6-2023

# Assessing the Contribution to OPV Efficiency of Energy Transfer in Charge Transfer Coupled H-aggregates.

Tyler James Wiegand
tjw8601@rit.edu

# RIT

# Assessing the Contribution to OPV Efficiency of Energy Transfer in Charge Transfer Coupled H-aggregates.

by

Tyler James Wiegand

A dissertation submitted in partial fulfillment of the requirements
for the degree of Doctorate of Philosophy in Microsystems Engineering

Microsystems Engineering Program
Kate Gleason College of Engineering

Rochester Institute of Technology
Rochester, New York
June 2023

**Assessing the Contribution to OPV Efficiency of Energy Transfer in Charge Transfer Coupled H-aggregates.**
**by**
**Tyler James Wiegand**

## Committee Approval:

We, the undersigned committee members, certify that we have advised and/or supervised the candidate on the work described in this dissertation. We further certify that we have reviewed the dissertation manuscript and approve it in partial fulfillment of the requirements of the degree of Doctor of Philosophy in Microsystems Engineering.

_____

Dr. Christopher J. Collison Date
Professor, Chemistry and Materials Science

_____

Dr. Santosh K. Kurinec Date
Professor, Electrical and Microelectronic Engineering

_____

Dr. Parsian K. Mohseni Date
Associate Professor, Electrical and Microelectronic Engineering

_____

Dr. David W. McCamant Date
Associate Professor, Chemistry

## Certified by:

_____

Dr. Stefan F. Preble Date
Director, Microsystems Engineering Program

# ABSTRACT

Kate Gleason College of Engineering
Rochester Institute of Technology

**Degree**: Doctor of Philosophy **Program**: Microsystems Engineering
**Authors Name:** Tyler J. Wiegand
**Advisors Name:** Christopher J. Collison
**Dissertation Title:** Assessing the Contribution to OPV Efficiency of Energy Transfer in Charge Transfer Coupled H-aggregates.

Organic photovoltaics (OPVs) are intended to be low-cost, long-lived devices with an array of possible applications. While record device power conversion efficiencies continue to improve, developments have largely been achieved with increasingly synthetically complex, high-cost molecules. Meanwhile, a deeper understanding of underlying molecular excited states and active layer structures influencing long-term performance is often neglected. To improve understanding of what drives efficiency in OPVs, Squaraine, a synthetically simple, low-cost organic molecule with a diverse array of excited state species and blending properties, is considered here. Focus is placed on the Squaraine charge transfer H-aggregate (HCT) and how active layer morphology influences the remarkable energy transfer properties of this species.

First, by quantifying the contribution to OPV efficiency of a diverse array of Squaraine excited state species, a clear dependence is observed on the extent of mixing between Squaraine and PCBM. Some mixing is shown to be beneficial for molecular devices, shortening the distance for exciton diffusion. However, improved crystallinity within Squaraine domains is observed to overcome any stifling of exciton diffusion associated with concomitant phase separation. Thus, since crystal packing could improve device efficiency, questions are raised about the efficiency contributions of HCTs which form in pure, crystalline Squaraine domains.

To address the concerning phase separation, incorporation of two different Squaraine donors in a two donor, one acceptor ternary blend is identified as a pathway for improved control over aggregation and phase separation within OPV active layers. Limited energy transfer across

diverse excited state populations and broad distribution of states is observed to have a dramatic negative effect on device efficiency. Yet, isolated HCT formation, or crystallization, is identified as not inherently bad for device performance when extensive phase separation is restricted. The typical negative impact of HCT formation on device efficiency in organic photovoltaics is determined to be primarily due to larger domain sizes and diverse excited state populations.

Finally, with sub picosecond transient absorption measurements we directly observe energy transfer kinetics of HCTs and identify morphological features that drive their contribution to device efficiency. Sub-picosecond energy transfer from HCTs to monomers is facilitated by the Dexter energy transfer mechanism. Furthermore, formation of a Squaraine:PCBM charge transfer complex is rapid following HCT excitation and energy transfer to monomers, demonstrating the potential of HCTs for OPV efficiency. However, excessive domain enlargement is found to slow down exciton motion and hinder energy transfer, emphasizing the importance of small domains in HCT-based OPV devices. This dissertation thus highlights the importance of well-mixed materials and the diverse array of active layer morphologies that Squaraine derivatives may provide. Rapid energy transfer observed in small domains of Squaraine charge-transfer H-aggregates is a key advantage for improving OPVs and driving research towards technological improvement and commercialization.

## ACKNOWLEDGMENTS

This dissertation was made possible by the amazing support from my collaborators, colleagues, family, and friends. First, I would like to thank my advisor, Dr. Christopher Collison, for his continued support throughout my PhD research at RIT. His detailed feedback, extensive questions, and passion for the subject helped me maintain both understanding and appreciation for my research.

I also wish to thank my committee members, Dr. David McCamant, Dr. Parsian Mohseni, and Dr. Santosh Kurinec for their support and guidance. I was incredibly fortunate to have had the opportunity to work with each of them, either in the classroom or in research.

I would like to thank my collaborators: Juan Sandoval, Steven Diaz, and Brendan Courtsal at University of Rochester. Dr. Tonya Coffey and Joseph Godoy at Appalachian State University. Dr, Kristen Burson, Hudson Smith, Adriana Cruz, and Catherine Ryczek at Hamilton College. Dr. Frank Spano at Temple University and Dr. Jeremy Cody at Rochester Institute of Technology. I would also like to acknowledge Ross Hisert and Dr. Stephen Polly at RIT for their help on various experiments presented in my dissertation.

I also want to acknowledge former and current group members of the Collison research group at RIT: Dr. Chenyu Zheng, Matthew Seitz, Iain Tracton, Soumya Gupta, Zhila Hooshangi, and Daniel Mojica, for their beneficial conversations and support both in and out of the lab.

I would like to thank my parents, my mom Connie Pflaum, my dad Ronald Wiegand, my step-mother Debra Wiegand, my step-father David Pflaum, my mother-in-

law Michelle Colton, and my father-in-law Craig Colton. Each of you played a tremendous part in helping to keep me motivated on this journey and I can't thank you enough.

Finally, I would like to thank my wife Kara. You supported me constantly throughout this process and were always there for me. Words cannot describe how thankful I am to you for everything you have done and all the support you have given me.

# TABLE OF CONTENTS

# LIST OF TABLES

# LIST OF FIGURES

# 1 Chapter 1. INTRODUCTION

## 1.1 Organic Photovoltaics Devices

### 1.1.1 Global Impact and Growing Demand

As the global population surpasses 8-billion people, increasing per-capita energy consumption and growing concern for environmental stability continues to drive technology towards reliable renewable energy. The utilization of nonrenewable energy sources, such as oil and natural gas, remains a primary cause of the release of greenhouse gases into the atmosphere. Simultaneously, ever increasing energy needs show no signs of slowing down. Therefore, there is a continuous need for new renewable energy sources to support renewable technologies already in place. While photovoltaics are already a prominent source of renewable energy across the globe, Organic Photovoltaics (OPV) are poised to provide another option with low cost, rapid throughput, and environmentally friendly devices.

Since 1954, when silicon semiconductors were first used to develop a photovoltaic (PV) device [1], the efficiency and cost of PV technology has improved dramatically. Commercially available systems have efficiencies around or exceeding 20% with efficiency guarantees of up to 25 years [2]. The research, development, and advancement of PV technology continues to enhance efficiencies and lifetimes while decreasing cost of production. While silicon-based devices still dominate the market, new semiconductor materials, such as organics, have been identified as a new option [3], [4]. As new technologies arise, the goal remains the same: provide clean renewable energy at the highest efficiency, longest lifetime, and with the lowest cost financially, and environmentally.

Many PV semiconductor technologies remain prohibitively expensive, and rigidity limits their potential to flat pane applications. As part of the third generation of photovoltaic technologies, OPVs aim to fill the gap. Since their discovery by Kearns and Calvin in 1958 [5], the promise of OPVs has been low cost, high efficiency photovoltaics fabricated using environmentally friendly methods and flexible substrates. With a constantly expanding field of research, efficiencies now

exceed 18% in laboratory fabricated cells [6]. With commercialization expected in the near future, potential applications for OPVs are numerous, with examples like flexible substrates [7]–[9] and colorful device tapestries [10], [11]. However, the commercialization of OPVs remains in its early stages, facing limitations that have restricted commercialization efforts so far.

The primary limitations which plague OPV technology include poor lifetime stability [12], [13], limited green production technique success [14], [15], and proven scalability to meet demand [16]. While efficiency has continued to grow year over year, this is often coupled with increasing material and manufacturing complexity [17], [18] which only increases the cost of the device. There is a need for low-cost materials with a simple synthetic pathway that can be used in long-lasting devices. Now that efficiencies have well exceeded the 15% benchmark [19]–[21] for commercialization efforts, the field must turn focus to other requirements for commercialization: lifetime, scalability, and green fabrication.

Of the many types of OPVs, bulk heterojunction (BHJ) devices consisting of mixed photoactive electron donor and acceptor materials, have demonstrated greatly increasing efficiencies enabled through a proliferating number of materials [22]–[27]. Despite major progress in the lab with new materials, commercialization attempts remain underwhelming and rely more on a small set of over-utilized conjugated polymers such as P3HT [13], [28], [29]. Commercial success will likely depend on the simple synthesis of small-molecule active layer materials and the efficiencies of devices made from these simpler materials. [17] For example, squaraines, a focus in this work, can be synthesized at low cost in very few steps. [30] However, the commercial viability of squaraine-based devices also depends on device efficiency, [31] which has room for improvement. The primary objective of this thesis will be the consideration of OPVs utilizing squaraines, a promising small molecule that is cheap to produce, in order to improve their status in the large library of OPV materials. In order to improve efficiency and drive commercialization of OPVs, it is first necessary to understand how they work.

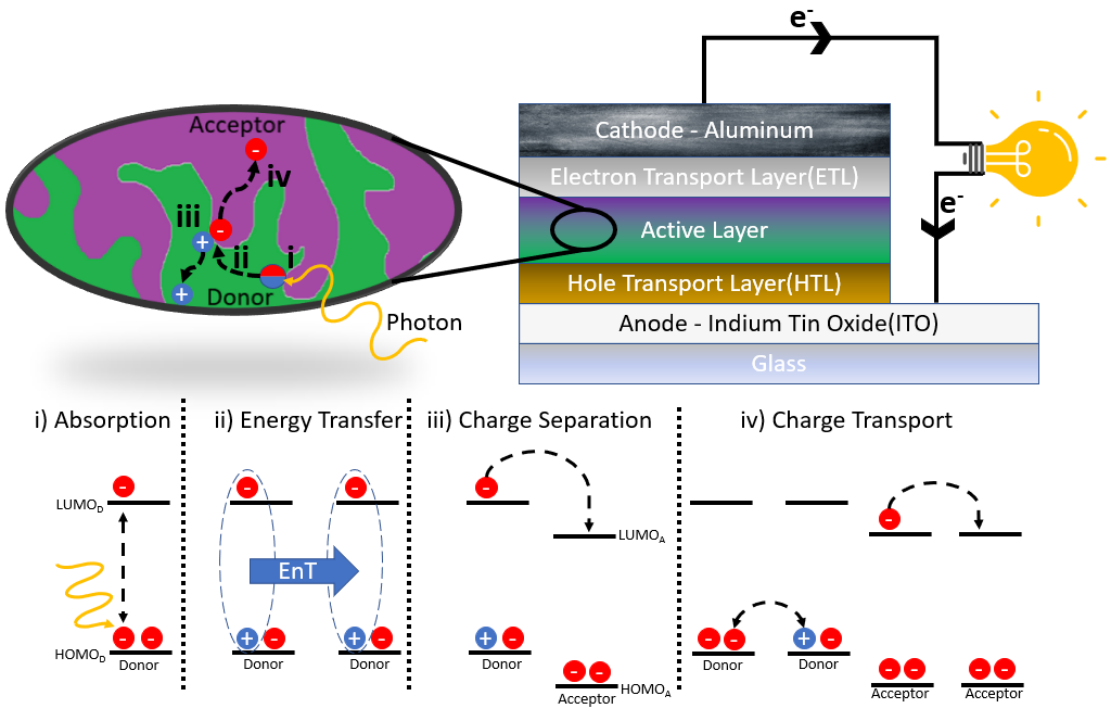


**Figure 1.1 – Simplified model of photon to electron conversion in and organic photovoltaic (left) and general structure of overall device (right). Below are electron and hole positions at each stage in the photon to charge carrier conversion process.**

### 1.1.2 Understanding the Device

#### 1.1.2.1 Structure, Fabrication, and Operation

OPVs convert solar energy into electrical energy with an all-organic-molecule active layer. To understand this process in detail, it is valuable to first understand the structure of an organic photovoltaic. A complete device structure, provided in Figure 1.1, is designed to promote efficient photon to electron-hole pair conversion, charge separation and subsequent collection, thereby generating electricity from sunlight. The main component is the active layer; composed of photoactive materials, this layer absorbs sunlight, generates collectible charge carriers, and transports them to electrodes for collection. The active layer may be fabricated in several different structures, discussed further elsewhere [32]; the focus here is on the Bulk Heterojunction (BHJ) structure, the most common in modern devices. A BHJ active layer is composed of two (or more) compounds, randomly mixed as in Figure 1.1. The morphology of the active layer, a broad term that includes crystallinity, domain size, and purity, among other properties, describes its structure. The molecules included within the active layer act as either an electron donor or acceptor during

operation. On either side of this active layer are two electrodes which serve to collect electrons (or holes) generated within the active layer and transport them to an external circuit. In select cases, hole (HTL) and electron (ETL) transport layers are utilized between the active layer and electrodes to improve device efficiency by improving separation of these charge carriers.

While fabrication of standalone device layers can take place using several different techniques, depending on materials and processing restrictions, this work focuses on the BHJ and its manufacture. Interested readers are referred elsewhere for information on electrode layer fabrication [33], [34]. For BHJ fabrication, the most common technique is spin-coating, whereby i) a concentrated solution of the photoactive material mixture is dissolved in a highly volatile solvent, ii) that solution is dispensed onto the substrate, which is iii) subsequently spun rapidly, allowing solvent evaporation to leave behind a thin layer of photoactive material. Chosen solvent, spin speed, concentration, and inherent molecular properties all influence the resulting morphology [14], [35], [36]; more detail on this is provided in a later section. After spin-casting, post-processing techniques such as thermal and solvent annealing may be utilized to further alter morphology, promoting material diffusion and phase separation. Other common techniques for the deposition of the bulk heterojunction include vacuum deposition [37], drop casting [38], and printing techniques [39].

Once fabricated, device operation occurs through five steps, four of which are shown in Figure 1.1: i) photon absorption, ii) energy transfer, iii) charge separation, iv) charge diffusion, and charge collection. Each of these steps has an associated efficiency that, when combined, describes the overall conversion efficiency ($\eta_{PCE}$) of a device by

$$\eta_{PCE} = \eta_{ABS} \times \eta_{EnT} \times \eta_{CS} \times \eta_{CD} \times \eta_{CC} \quad 1\text{-}1$$

where $\eta_{ABS}$ is the efficiency of photon absorbance, $\eta_{EnT}$ is the energy transfer efficiency, $\eta_{CS}$ is the charge separation efficiency, $\eta_{CD}$ is the charge transport efficiency, and $\eta_{CC}$ is the charge collection

efficiency. While Figure 1.1 provides a cartoon depiction of select steps, greater detail is necessary to understand what drives the efficiency of each step.

The incident photon, absorbed by photoactive materials, may excite a ground state electron from the highest occupied molecular orbital (HOMO) to the lowest unoccupied molecular orbital (LUMO). The absorption probability for a photon is a complex quantity accounting for the transition dipole moment, conservation of momentum, selection rules, and molecular symmetry, among other contributing factors. Those interested in better understanding are directed to [40] although some details will be provided later. The resulting excitation, an exciton, is a coulombically bound electron-hole pair on the excited molecule, held together with a binding energy on the order of several hundred millielectronvolts and a predicted lifetime typically on the order of hundreds of picoseconds [41]. Once generated, this exciton may diffuse through the active layer via energy transfer (EnT) from molecule to molecule. The distance the exciton is capable of travelling is typically estimated as 10 nm [41]–[43], although the distance, and even direction, varies due to differing pathways and intrinsic molecular properties. If the exciton successfully diffuses to the interface between donor and acceptor, before it decays back to the ground state, a lower energy unoccupied molecular orbital in the electron acceptor will encourage charge separation through relaxation of an electron from donor to acceptor. (It is important to note that excitons generated on the acceptor material will result in a separation of charges through a similar mechanism with the hole being donated from acceptor to donor. However, it is commonplace to describe the mechanism from the point of view of a photogenerated exciton on the electron donor. Regardless, the result is a charge separated state with the electron residing on the acceptor and the hole residing on the donor.) Once chemically separated, the opposing charge carriers must overcome coulombic attraction and then individually diffuse through the active layer to their respective electrodes for collection. As described by Equation 1-1, if any step described here has a low efficiency, the device

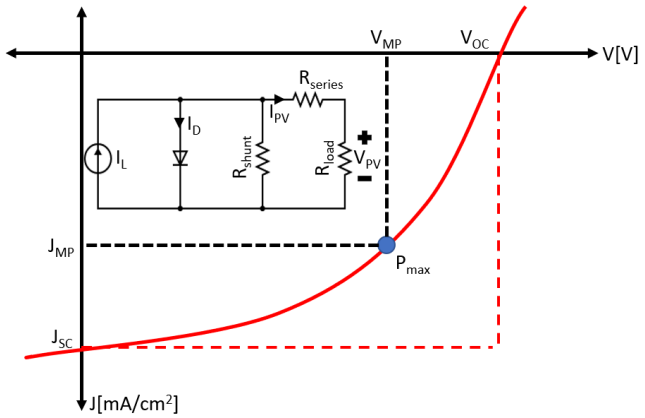


**Figure 1.2 – JV-curve of a photovoltaic under illumination. Inset is a simplified circuit model of an illuminated photovoltaic.**

suffers no matter how efficient the other processes are. Researchers must therefore optimize all processes to make the best performing device.

#### 1.1.2.2 Device Testing

Evaluating the efficiency of each step in the mechanism individually is no small feat, so device testing most often begins with measuring overall efficiency in current density(*J*) vs. voltage(*V*) curve while the device is exposed to a light source, an example of which is provided in Figure 1.2. From this measurement the open-circuit voltage($V_{OC}$), short-circuit current density($J_{sc}$), fill factor(FF), and the power conversion efficiency(PCE) are determined. $V_{OC}$, determined by the curve's intersection with the x-axis, is the applied voltage which halts current flow. The $V_{OC}$ is proportional to the energy difference between the acceptor LUMO and the donor HOMO, also thought of as the energy of the electron-hole pair after charge separation. $J_{sc}$, determined by the y-axis intersection, is the current density per unit area flowing through the device when there is no applied voltage opposing charge flow. $J_{sc}$ is largely influenced by the number of photons absorbed by the photoactive material, since more absorbed photons will lead to more electrons and increased current. FF is a characteristic quantity of the JV-curve describing its squareness with a more rounded curve having a lower fill factor due to a variety of energy losses related to device structure [44], [45]. FF may be calculated by

$$FF = \frac{V_{MP} \times J_{MP}}{V_{OC} \times J_{SC}} = \frac{P_{max}}{V_{OC} \times J_{SC}} \quad 1\text{-}2$$

where $P_{max}$ in Figure 1.2 is the maximum power point based on the product of current density ($J_{MP}$) and the voltage ($V_{MP}$). These three values are combined to calculate the output power of the device ($P_{out}$) in

$$V_{OC} \times J_{SC} \times FF = P_{out} \quad 1\text{-}3$$

which is divided by the input power from the light source ($P_{in}$) to determine the device's power conversion efficiency.

$$\frac{P_{out}}{P_{in}} = \eta_{PCE} \quad 1\text{-}4$$

Beyond the JV-curve, two other common methods for efficiency evaluation are measurements of carrier conversion quantum efficiency and thin film absorbance. The latter is a measure of the fraction of photons absorbed by the thin film across a range of photon wavelengths, typically selected based on the solar spectrum, and represents the $\eta_{ABS}$ term in Equation 1-1. Greater absorbance increases exciton generation, leading to greater device output power if those excitons are separated into opposing charge carriers and able to diffuse to electrodes for collection. The other measurement, carrier conversion quantum efficiency (QE), describes the efficiency of photon to separated charge conversion and collection. QE may be measured externally (EQE), the probability of an incident photon being absorbed, converted to charge carriers, and collected. Internal Quantum Efficiency (IQE) is the efficiency of just the conversion and collection process and is measured after the photon is absorbed. IQE combines all terms, other than $\eta_{ABS}$, in Equation

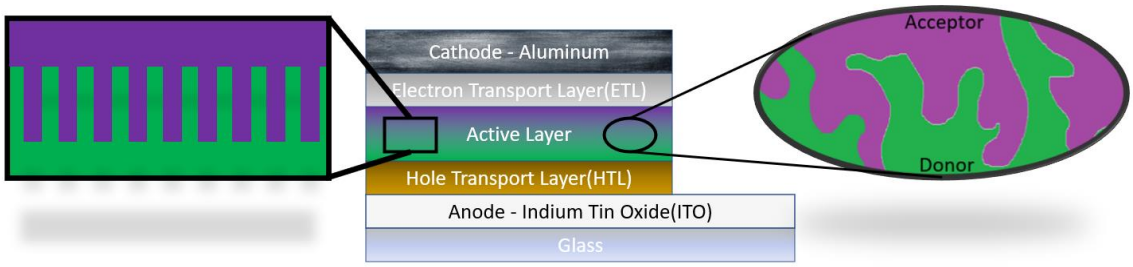


**Figure 1.3 – Theoretical optimum structure of the morphology (left) compared to a more experimentally common BHJ morphology (right) achieved from the spin-coating fabrication process.**

1-1. The IQE of a photovoltaic is measured by comparing the number of electrons extracted from the device to the number of photons absorbed by the device.

#### 1.1.2.3 Morphology Control and Description

From the operational description of OPVs, it is evident that the efficiency of a device is largely dependent on the structure, or morphology, of its BHJ active layer. To maximize efficiency, material domains must be small enough to ensure easy energy transfer to the interface, providing the maximum interfacial area for charge separation. At the same time, domains must be sufficiently continuous to provide separated charges a clear pathway to electrodes after separation. An ideal morphology is a series of thin interwoven fingers of donor and acceptor as in the left side of Figure 1.3, yet the reality is more often akin to the right side of Figure 1.3 for a BHJ. This raises the essential question of how morphology is optimized to maximize device efficiency. Obtaining a bicontinuous network of domains, both small and interconnected, through spin-coating requires either self-assembly during deposition or post-processing guidance [35]. Six components typically determine the morphology obtained through self-assembly from spin-casting: processing conditions, primary casting solvent, solvent additives, overall concentration, material ratios, and molecular structure [35].

Processing conditions encompass characteristics like the substrate rotation speed, substrate area, and the volume of solution dispensed. Faster spin speeds decrease film thickness as a greater quantity of solution is thrown off the substrate before the solvent can evaporate. Larger substrates may also have a thinner film as the solution is spread out over a greater surface area with fewer

substrate edge effects, perhaps reducing the amount of material available per unit area. The inertia of a larger substrate will also influence the angular acceleration, which in turn can affect film properties. Lastly, a smaller volume of dispensed solution further induces film thinning by providing less material per unit area.

Primary casting solvent(s) are the volatile solvents that the photoactive material is dissolved in. More volatile solvents will have an increased rate of evaporation, increasing material deposition rate. A faster deposition rate reduces the available time for molecular reorientation time during the deposition. Therefore, a rapidly deposited film will have less opportunity for dynamic molecular alignment towards a thermal equilibrium, that may include phase separation and crystallinity in pure domains. Solvent choice can also determine the deposition order of molecules based on solubility limits, where higher solubilities mean the solute will stay solvated for longer as solvent evaporates and concentration increases, while lower solubilities lead to earlier precipitation during spin coating.

The use of solvent additives has been fruitful for manipulating thin film morphology [35], [46]. Solvent additives, added to the solution in small quantities, typically promote separation of donor and acceptor due to higher boiling points and favorable solubilities. High boiling point additives promote the development of a thermodynamically stable morphology because the solution remains for longer times than when simply using a highly volatile solvent [47], although select solvent additives have also been demonstrated to enhance mixing [48]. However, concerns regarding reproducible results have been raised regarding morphology stability and whether such additives are a source of toxicity in fabrication [35]. Additionally, removal of solvent additives from the active layer matrix may be both necessary and costly [49]–[51]. Unremoved residual concentrations of high boiling point additives may promote further unintended and unwanted phase separation.

Changes to molecular concentration alter the rate at which material falls out of solution as solvent evaporates. The concentration of active layer material in the spin-casting solvent will also

lead to changes in viscosity of the solution, which will have an impact, although the viscosity changes are very small for molecular systems as compared to those spin casting solutions made from polymer active layer materials. If a solute is highly concentrated in the solution, more material is deposited onto the surface. The resulting thicker film will trap solvent deeper within the film, increasing drying time and giving solute molecules more time to organize, or crystallize, after the spin-coating process due to the elongated drying time. The effect is like annealing, allowing the molecules to move towards a preferred thermodynamically stable state through the additional translational freedom the solvent provides.

Lastly, we consider material ratios and molecular properties, two of the more important characteristics in the context of this work. The properties of molecules and their interactions with each other will directly influence their ability to mix (or not). Both early kinetic behaviors during the casting process and long-term thermodynamic interactions will influence the morphology [35], [52], [53]. Molecules which are found to mix well together are likely to promote small, highly impure domains which greatly support EnT to the interface but may limit the efficiency of the charge transport that follows. In contrast, molecules with a tendency to phase separate will produce large, pure domains of each material leading to developed pathways for charge transport, but larger distances for the exciton to traverse. While there is no fully encompassing description of the interactions of molecules based on their molecular properties, mixing is driven by intermolecular forces and entropy. In OPVs, the donor and acceptor are often combined in mass ratios very close to 1:1 to ensure adequate pathways for charge diffusion and provide more interfacial area for charge separation, though this is not a requirement. Each new combination of materials will have its own optimal morphology and material ratio, and identifying that optimum is no small undertaking.

The morphology of the active layer may be characterized by several parameters describing the microstructure of the material mixture. The most common analysis includes measurement of the topography, distribution of materials (blending), and crystal packing. Topography of the film, often measured by atomic force microscopy (AFM) [54], is essential for describing surface

roughness as it defines the interface with the top electrode, which is influential in charge collection efficiency [55]. Material distribution on the surface may be monitored by techniques derived from (AFM), such as Kelvin Probe Force Microscopy, to determine the distribution of materials on the surface [54] and even the bulk, through measurement [56] or extrapolation. Accurate descriptions of material distributions can give estimates of the sizes of domains throughout the active layer and allow for an evaluation of domain purity, a factor that influences extent of crystallinity. Crystal packing describes how the molecules orient with respect to each other and the surface. When molecular packing transitions from amorphous to a crystalline state, electron wavefunctions of neighboring molecules may have a larger overlap, increasing charge mobility. A combination of the identified morphological characteristics can therefore provide an excellent picture of the BHJ. Once the optimal morphology is determined through correlation with device efficiency, the challenge then becomes obtaining (or retaining) that morphology throughout the lifetime of the device.

When designing or selecting materials to act as electron donor and acceptor, a significant number of characteristics must be considered. It is not as simple as just selecting the cheapest molecules to move forward with. As a result, the library of materials utilized in OPV numbers in the thousands, each of which has its own qualities [18], [57]. In the long run, any commercialized material must be cheap to produce in high quantities [17], [18]. Until around 2015, fullerene derivatives dominated as the acceptor [58] and only the donor was adjusted. Fullerenes were prized for extensive conjugation, isotropic charge transfer characteristics, and limited concerns for crystal structure variation [58]. Beyond that, they were readily commercially available and reasonably priced for laboratory levels of production. However, fullerene's downfalls became apparent as commercialization became more possible and efficiency began to drive literature. A major shift occurred toward selectively designed non-fullerene acceptors (NFAs) built to order for OPV and radically improving device efficiencies [58]. While the ever-expanding library of materials for OPV has allowed device efficiency to grow exponentially, it has allowed materials to become lost in the

literature if they fail to immediately exhibit high efficiency. This is concerning as finding the optimal efficiency (through morphology) is easier said than done. Often forgotten on the quest for high efficiency is the original goal of OPV to be a low-cost PV technology. High efficiency, long lasting devices composed of low-cost components must be focused on if OPV technology is ever going to be successfully commercialized.

### 1.1.3 Maximizing Efficiency

Because the efficiency of each step in the OPV mechanism must be maximized, a discussion here on some additional device parameters is necessary. The first parameter, absorbance, is largely defined by the materials that make up the active layer. Each molecule has different HOMO and LUMO energy levels, the energy difference between which defines the minimum photon energy that may generate an exciton for that molecule. While the HOMO-LUMO gap defines the required photon energy, it is the oscillator strength which defines molar absorptivity and probability of absorption [40]. Through interaction of the molecule's electron cloud with the absorbed oscillating electromagnetic wave, a non-zero transition dipole moment creates an electron cloud rearrangement. The square of the transition dipole moment is proportional to the oscillator strength [40]. Without interaction between the electron cloud and photon, or when a transition dipole moment is zero, no absorption may occur, and the photon will be transmitted and lost. Furthermore, even for the same molecule, the HOMO-LUMO gap and oscillator strength vary with the properties of the molecular environment, allowing a range of wavelengths to excite a molecule with variable probabilities [40]. To maximize the absorbance efficiency, the bandwidth of absorbance should be broadened to absorb the maximum fraction of the solar spectrum. Selecting molecules with increased intrinsic absorbance probability and bandwidth is the first step towards improving device efficiency, to ensure more photons are absorbed. Typically, absorbance of the donor and acceptor are chosen to be complementary, improving device efficiency. The interested reader is referred to [40] for further information on the absorption properties of molecules.

The second step in the device mechanism, diffusion of Excitons, is the most significant characteristic, differentiating OPVs from other PV technologies. The diffusion of these electrically neutral excited states is often referred to as occurring through energy transfer (EnT) mechanisms as the energy is moved between molecules within the active layer [41], [59]. EnT occurs in OPVs primarily through either Dexter [60] or Förster [61] (Fluorescence Resonance Energy Transfer, FRET) mechanisms. However, there may be other contributing or competing mechanisms [62]. A complete discussion of energy transfer theories and experimentation is essential in the context of this work and is reserved for a later section. For now, an improved energy transfer rate increases the distance the exciton may travel for a fixed lifetime ($\tau$), increasing the likelihood it reaches the interface for charge separation. The efficiency of energy transfer ($\eta_{EnT}$) , or exciton diffusion, is described by an exponential ratio of the exciton diffusion length ($L_D$) and the distance from the exciton to the nearest donor:acceptor interface ($d$) in

$$\eta_{EnT} = e^{-\frac{d}{L_D}} \qquad \text{1-5 [63]}$$

where $L_d$ may be described by the exciton's diffusion coefficient ($D$), determined by previously discussed EnT mechanisms, and the dimensionality of diffusion ($Z$) in

$$L_D = \sqrt{2ZD\tau} \qquad \text{1-6 [42]}$$

Without successful charge separation, recombination occurs such that the excited electron relaxes back down to the ground state, releasing its energy as either a photon (radiative recombination) or thermal energy and vibrations (non-radiative recombination). Additional competing actions include inter-system crossing to a long-lived lower energy triplet state which may behave as a trap, fission processes by which initial excitations break into two separate lower energy triplet states [64], or fusion processes by which two low energy excitons may combine to form a single higher energy exciton [65], [66]. A final competing mechanism is exciton-exciton annihilation whereby two excitons come into contact and destroy one-another [67]. Because this requires two excitons to be

in close vicinity, it depends highly on the power density of incoming photons and the concentration of a specific material on which the resulting excited states reside in the blend [68]. Each of the described mechanisms has different kinetics and probabilities and each influences device performance.

Once the exciton reaches the interface between the donor and acceptor materials, the excited state must undergo charge separation, which results in the hole being on the electron donor and the electron being on the electron acceptor. It was long believed that this process required a driving force to enhance charge separation efficiency and overcome the exciton's coulombic binding energy. This driving force is introduced by an energy offset of the LUMOs for excitons generated on the electron donor, of the two active layer components, typically in the range of 300meV. However, recent reports have suggested this required driving force may not be a necessity and is solely a consequence of poor interactions between the chosen donor and acceptor [69]. Fullerene derivatives were the typical choice for electron acceptor owing to their reasonably high manufacturing scale and isotropic charge transfer behavior believed to improve device efficiency [69], [70]. However, the most common acceptor, PCBM ([6,6]-phenyl C61 butyric acid methyl ester, or $PC_{61}BM$), remains too costly for large scale manufacturing, and it was determined that the previously required energy offset was likely an artifact of poor donor interaction with the PCBM [69], a key reason for the shift to NFAs [58], [71]. Eventually, more appropriate acceptors currently limited to low-scale, high-cost syntheses will likely take its place, but for now PCBM remains a common acceptor choice due to availability and an extensive library of reference literature employing PCBM as the acceptor [72].

The final processes after successful charge separation are charge transport (diffusion) to the electrodes and charge collection. Once separated, charges may diffuse freely through the domains of their selected material as they are no longer coulombically bound to the opposing charge carrier, to which they were "geminately" formed. These independent charges diffuse through a hopping mechanism between neighboring molecules towards their respective electrode interfaces

[73], [74], at which point they are collected. Factors influencing the efficiency of this hopping are expected to include the size, purity, density, and uniformity of domains within the active layer. There must be a clear path between the point of separation and the electrode, otherwise there is a risk for the charge to become stuck in a trap or undergo recombination with an opposing charge carrier. Recombination may occur from both a previously separated geminate and non-geminate electron-hole pair; charge carriers must be collected without non-geminately recombining with an opposing charge at any available interface. Therefore, a more crystalline and organized domain is expected to better enhance charge mobility and therefore to facilitate the efficiency of this motion. Lastly, the collection of these charges at the electrode is largely dependent on the interface properties facilitating a smooth transition, providing good contact, and the resistance of the corresponding electrode. Influential properties can include relative energy levels, surface roughness, molecular alignment at the surface, and the inclusion of ETLs and HTLs as previously mentioned to selectively collect a single charge type [74]–[77].

The efficiency of all five of these steps determines the efficiency of an OPV device and must all be maximized. However, sole maximization of each step, and consequently maximizing the device efficiency, is insufficient for commercialization. The device efficiency overall, and for each step, must be maintained over the entirety of the device's operational lifetime. If any one step should fail, the efficiency of the others are irrelevant. As such, focus is now turned to evaluating how device efficiencies may change over the course of operational lifetime due to environmental and operational stressors, and how researchers can change the device to prevent failure.

### 1.1.4 Device Lifetime Considerations

Improving the efficiency of a device is meaningless if the device is too costly and does not maintain performance over a sufficient lifetime to counter the cost. There needs to be a dramatic research shift to focusing on improving device lifetime [12], utilizing less costly materials, and using fabrication techniques that are scalable [78]. While each of these considerations warrants their own full discussion, here we will discuss specifically how morphology can impact long-term

device performance. Changes can occur from selected fabrication techniques or as a natural consequence of device operation in a non-laboratory-controlled environment.

Maintaining morphological control over the lifetime of an organic photovoltaic device is essential for commercialization of the technology. Organic molecules in a BHJ differ dramatically from inorganic crystals like Silicon as they are not locked in a lattice and are instead intermixed during fabrication and free to translationally diffuse. Over time with sufficient thermal energy, certain compound combinations may phase separate to form larger pure domains of each component, leading to significant morphological changes and device efficiency fluctuations. These phase separations are determined by the enthalpy of the interactions between components, the entropy associated with highly mixed states, and the kinetics of mass transport driven by temperature. Optimizing and locking in the best morphology is essential to ensure that the device maintains its efficiency over the course of its lifetime. Any relaxation from the optimized structure is predicted to dramatically change the efficiency [79].

The best-case scenario for a device is when selected materials have an optimized morphology that is comparable to its eventual thermal equilibrium. In this case, thermally induced changes to morphology such as limited phase separation, can be instigated in production. If the optimal morphology is not the thermal equilibrium, it becomes necessary to find ways to prevent significant mass transfer during operation. One potential solution is the introduction of cross-linked polymers to limit diffusion and lock molecules into larger polymer structures [80], [81], [82]. Alternatively, inclusion of additives within the mixture has been shown to promote a specific morphology by interacting with select components to alter blending characteristics [46]. Inclusion of additives often leads to incorporation of a third primary component in a ternary blend active layer [83]. The third material can be selected to provide a number of benefits such as a third complementary absorbance and increased control over device morphology [83]. However, selection of this third component further increases the number of variables leading to device efficiency and so careful consideration of available materials becomes very important.

## 1.2 Excited States, Energy Levels, and Energy Transfer

In addressing the changing morphology of devices over operational lifetimes, a need arises for a deeper understanding of molecular interactions. While we have already discussed how changing properties in the bulk can influence the efficiency of devices, there are additional changes which occur at the molecular level which can completely alter the behavior of a device. A more detailed framework will be provided here for interactions of molecules on a more intimate scale than on the entirety/bulk of the BHJ. The impact of the work presented here depends greatly on three types of interactional packing structures: monomers, aggregates, and charge transfer species. Although these three species have been described in more detail elsewhere, we provide here a brief review.

### 1.2.1 Monomers

A monomer is a single molecule that is isolated physically and electronically from other similar molecules which it has the potential to interact with. Often monomers are best described by the behavior of dilute solutions where molecules may freely undergo translational and rotational motion without interaction with other solutes. Monomers are typically characterized by narrow absorption bands due to limited variability in their environment which would otherwise alter energy levels, and because of their rapidly changing orientation. The absorbance characteristics of monomers in a thin film, while similar to those of an isolated molecule in solution, will often produce shifts in absorbance as they move from a liquid solvent to a solid solvent with a different dielectric constant/permittivity and as realignment of the surrounding molecules in the solid lattice is restricted [84], [85]. In addition to a red-shift, the absorbance is often broadened in a thin film due to variation in molecular environment from molecule to molecule. Physical and electronic isolation in a thin film is not so easily achieved due to the inherent density of molecules leading to aggregation [85].

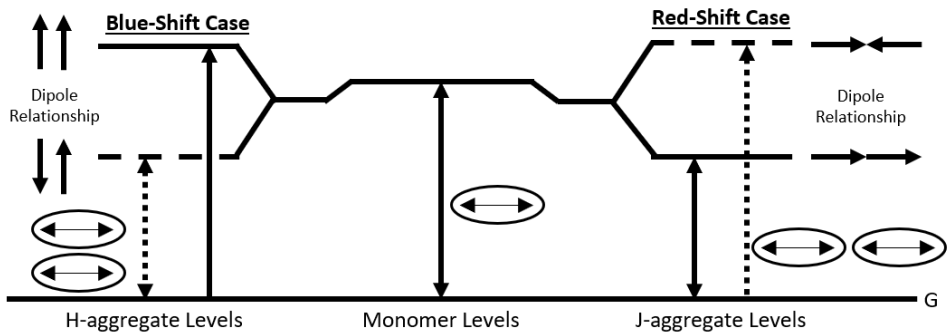


**Figure 1.4 – Splitting patterns of the H-aggregate (left) and J-aggregate (right).**

### 1.2.2 H- and J-Aggregates

Aggregates appear in thin films as dipoles of nearest neighbor molecules reorganize towards preferred orientations. For example, J-aggregates are characterized by a head-to-tail packing motif where transition dipole moments point towards or away from one another as in Figure 1.4. J-aggregates are identifiable by a red shift in the absorbance spectrum along with a significant enhancement in photoluminescence efficiency. H-aggregates on the other hand result when molecules pack face-on, leading to neighboring transition dipole moments which are either parallel or antiparallel, as in Figure 1.4. H-aggregates tend to produce a blue shift in the absorbance spectrum (and a dominance in the $0 \rightarrow 1$ vibronic band over the $0 \rightarrow 0$ vibronic band [86], [87]) and a significant reduction in the photoluminescence efficiency. While a detailed description of the properties of these species along with a quantum mechanical explanation can be found elsewhere [86], [88], we provide additional details specifically on H-aggregates which are consequential in this work.

Fluorescence in H-aggregates has been shown theoretically and experimentally to be forbidden if the transition dipoles are parallel [86], [88], [89]. To explain, we recall that a non-zero transition dipole moment is a requirement for absorption as its square is proportional to the oscillator strength. When transition dipole moments of neighboring molecules are parallel (pointed in the same direction), the arrangement results in an overall non-zero transition dipole moment pointed in the same direction and the associated transition is allowed. This parallel state is higher

in energy than the monomer due to repulsion from the dipole interaction and is commonly referred to as the bright state. In contrast to the bright state of the H-aggregate, excitations to the anti-parallel state are forbidden since the opposing transition dipole moments of neighboring molecules will produce a net zero transition dipole moment. The anti-parallel state is both lower in energy and is commonly referred to as the dark state. Because excited states tend to relax in energy very rapidly following excitation, via internal conversion, an H-aggregate bright state will relax into the dark state which cannot transition to the ground state by fluorescing may act as a trap since the release of energy is limited to non-radiative decay. While the lack of fluorescence will be further evaluated later, the lower energy of the dark state may be damaging to the performance of OPV as it makes charge separation at the interface less favorable due to a reduced driving force from the LUMO-LUMO energy gap between the donor and acceptor, a key part in the OPV mechanism.

In the context of this work, we define a dimer H-aggregate (DHA) based on the dipole interaction between one molecule and its nearest neighbor. The intermolecular spacing and molecular orientation at which H-aggregate interactions occur is somewhat variable. Zheng *et al.* showed how the absorbance spectrum, and corresponding shifts of aggregates, will change based on proximity and orientation [68]. Further blue shifts and increasing magnitude of H-aggregate bright state absorbance occurs as the concentration of the interacting molecules increases and the nearest neighbor distance decreases [68]. Furthermore, since these two molecules are randomly oriented and may not be perfectly parallel, the absorbance properties are based on a distribution of all possible angles allowing dipole–dipole interaction. The result is a spectrum that can be clearly defined theoretically, but with subtle variation experimentally.

### 1.2.3 Intermolecular Charge Transfer State

When molecules are very tightly packed, creating an overlap of the electron orbitals of neighboring molecules, it becomes possible for excited electrons to hop onto their nearest neighbor, forming an intermolecular charge transfer (ICT) state. The result is an excited state where the

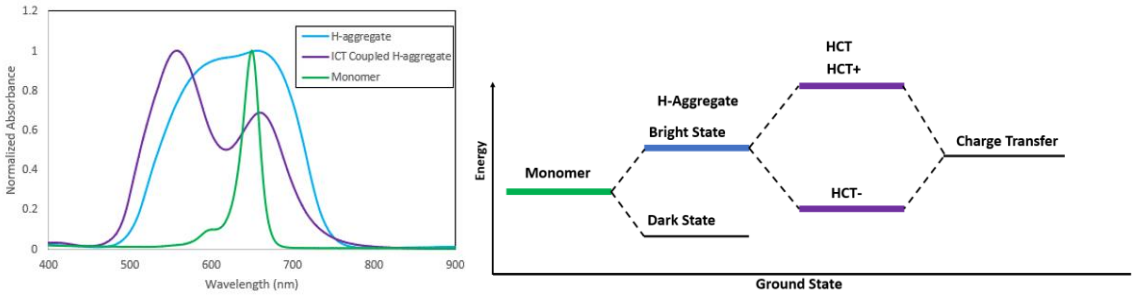


**Figure 1.5 – Example absorbance spectra (left) and relative energy levels (right) of the monomer, H-aggregate bright and dark states, and charge transfer coupled H-aggregate low (HCT-) and high (HCT+) energy state.**

excited electron and hole exist on two separate neighbors. This is like the charge transfer state previously described as a part of the OPV mechanism, when the electron moves from electron donor to electron acceptor, leaving behind the hole on the donor. However, the ICT state being discussed here is on two of the same molecules [90]. We now have two species which become possible with small intermolecular spacing, a coulombic H-aggregate through dipole interactions and an intermolecular charge transfer species through orbital overlap. The bright state of the excitonic H-aggregate, when similar in energy to the ICT state, couples with the neutral charge transfer state that resides over two closely packed adjacent molecules [86], [90]. Through coupling, the ICT state borrows oscillator strength from the H-aggregate bright state and quantum mechanical splitting results in two coupled states. With the borrowed oscillator strength, absorbance transitions to these two states are allowed, resulting in a "double hump" absorbance spectrum [90], [91], shown in Figure 1.5. This spectral assignment was confirmed by the essential states model whereby a Squaraine molecule, later discussed in section 1.4, is described as two electron donating units, the amine side arms, and a central electron accepting group, the squarylium ring [90], [92]–[96]. The essential states model goes beyond typical interactions modelled by Kasha's theory of molecular aggregates, which focuses on coulombic interactions, to account for the possibility of a charge transfer nature to transitions. This includes a lower energy state (HCT(-)) than the bright H-aggregate, and possibly the monomer, that may act as a long-lived trap [90]. The relative energy of

the two humps in the ICT coupled state (HCT+ and HCT-), the H-aggregate's dark and bright state, and the monomer is shown in Figure 1.5.

## 1.3 Energy Transfer (or Exciton Diffusion)

### 1.3.1 Theoretical Foundations

Energy transfer is the process by which an excited state (exciton) diffuses through a material, and it can occur via several possible mechanisms. These transfers occur over very short timescales and a wide range of distances depending on the mechanism [40], [41], [67]. The first energy transfer mode is called the 'trivial' mechanism and it occurs after actual photon emission by the energy donor followed by that photon's reabsorption by the energy acceptor. Since a photon can be emitted at one point and may travel over a 360-degree solid angle, this mechanism is never important and is incredibly inefficient. Nevertheless, the efficiency of this mechanism can be quantified and depends in part on i) donor emission quantum yield, ii) number of absorbing acceptors in the photon path, iii) efficiency of acceptor light absorption, and iv) the overlap of donor emission and acceptor absorption [40]. This overlap, however, remains particularly important for energy transfer in general. It is often described by the normalized spectral overlap integral,

$$J = \int_0^\infty \lambda^4 F_D(\lambda)\sigma_A(\lambda)d\lambda = \int_0^\infty I_D(\tilde{\nu})\varepsilon_A(\tilde{\nu})d\tilde{\nu} \qquad \text{1-5[40], [42]}$$

using the normalized emission spectrum of the donor ($I_D$) and the absorption spectrum of the acceptor described by its extinction coefficient ($\varepsilon_A$) [40]. From this description, the trivial mechanism requires a large extinction coefficient for the accepting state (ii) and a high quantum yield of emission for the excited donor (i). Two other energy transfer mechanisms dominate energy transfer in general, as it features in various applications.

Förster energy transfer, also known as fluorescence resonance energy transfer (FRET) [61], involves the transfer of energy via dipole-dipole coupling between the energy donor and acceptor molecules through a "virtual photon". The efficiency or rate of the FRET is proportional to the square of the electrostatic interaction energy (E) between the two interacting dipoles,

$$k_{EnT,FRET} \propto E^2 \approx \frac{\mu_D^2 \mu_A^2}{R_{DA}^6} \quad \text{1-6[40]}$$

where $\mu_D$ is the transition dipole moment of the donor, $\mu_A$ is the transition dipole moment of the acceptor, and $R_{DA}$ is the separation in space between energy donor and acceptor. Often this proportionality is reinterpreted using a variety of experimental parameters as

$$k_{EnT,FRET} = \frac{9\phi_{PL}\kappa^2}{128\pi^5 n^4 \tau_0 R_{DA}^6} J(\varepsilon_A) \quad \text{1-7[41], [42]}$$

or

$$k_{EnT,FRET} = \alpha \frac{\kappa^2 k_D^0}{R_{DA}^6} J(\varepsilon_A) \quad \text{1-8[40]}$$

where $\phi_{PL}$ is the photoluminescence quantum yield, $\kappa^2$ describes the mutual orientation of the dipole moments for each species, $n$ is the refractive index of the medium, $\tau_0$ is the intrinsic lifetime of the exciton, $\alpha$ is a proportionality constant that reflects experimental parameters such as concentration and refractive index, $k_D^0$ is the radiative decay rate of the donor, and $J(\varepsilon_A)$ is the spectral density integral which is similar to the spectral overlap integral except the true unnormalized value of the extinction coefficient of the acceptor is included in the integration. Regardless of chosen experimental variables, it is key that the efficiency is once again dependent on the fluorescence efficiency of the donor in all cases ($\phi_{PL}$, $k_D^0$) and therefore this limits the energy transfer contribution of H-aggregates.

A final mechanism, Dexter energy transfer, transfers energy between neighboring (or colliding) molecules via direct electron exchange, a non-radiative process[40]–[42], [60], between the two molecules through the overlap of their molecular orbitals. The rate of Dexter energy transfer is described by

$$k_{EnT,Dexter} = KJe^{\left(-\frac{2R_{DA}}{R_{DA}^0}\right)} \quad \text{1-9[40], [41]}$$

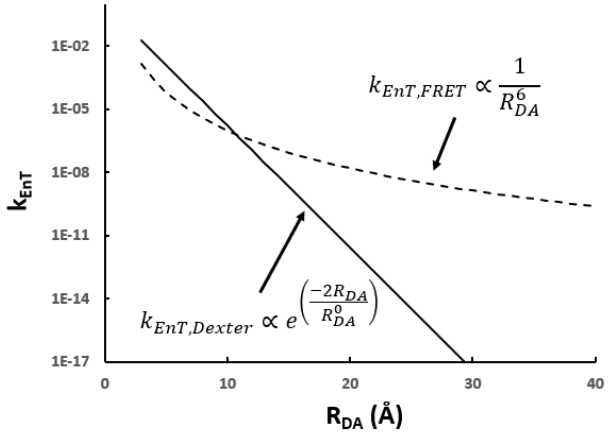


**Figure 1.6 – Relative dependence of energy transfer rates on distance between energy donor and acceptor for the FRET (Dipole-Dipole) and Dexter (Exchange) mechanisms.**

where $K$ describes the orbital overlap of neighboring molecules acting as energy donor and energy acceptor,$R_{DA}$ the separation in space between energy donor and acceptor, $R_{DA}^0$ is the separation of the two species such that they are in van der Waals contact, and $J$ is the normalized spectral overlap integral where the area of both the emission spectrum and the extinction coefficient are adjusted to unity [40]. It is essential to note here our interpretation that the normalized spectral overlap contribution to this equation is an experimentally determined variable describing the density of overlapping states in both species [40], [67]. Thus, according to this interpretation, there is no dependence here on the magnitude of the dipole moment for either the energy donor or acceptor and therefore a dark species such as an H-aggregate dark state may contribute to energy transfer. However, Dexter energy transfer is highly dependent on the distance and orientation relationship between the two molecules, as well as the strength of their electronic coupling. FRET outperforms the efficiency of Dexter energy transfer for large intermolecular separations as FRET maintains higher efficiency at longer distances according to

$$k_{EnT,FRET} \propto \frac{1}{R_{DA}^6} \qquad 1\text{-}10$$

compared to the Dexter equivalent of

$$k_{EnT,Dexter} \propto e^{\left(-\frac{2R_{DA}}{R_{DA}^{0}}\right)} \quad 1\text{-}11$$

for which $R_{DA}^{0}$ is typically on the order of a few angstroms. A comparison of the effect these proportionalities have on the rates of each mechanism is provided in Figure 1.6. Because dark species may be transferred only by the Dexter mechanism, the energy transfer contributions of dark states may be inherently limited to hops across short intermolecular separations. [67] While Dexter and FRET mechanisms are the dominant explanation for energy transfer in OPVs, there are other proposed mechanisms such as "coherence"[62], [97], although these mechanisms are less commonly used as an explanation for OPV performance [41], [67], [98], [99].

### 1.3.2 Energy Transfer Behavior

While theoretical understandings of energy transfer are key in predicting device behaviors, validation of theories with experimental work confirm understanding. There are two different characteristics that should be evaluated for any system in the context of improving OPV efficiency: i) the rate and efficiency of energy transfer and ii) the preferential direction of the process. The former is largely described by the equations of the previous section along with the expected distance the exciton may diffuse prior to a spontaneous decay back to the ground state. The latter (ii) is often described as a somewhat random walk due to the inherent neutrality of excitons not being influenced by external fields. However, it has been shown that the energy landscape of neighboring molecules can drive the direction of energy transfer if it is aligned with a particular spatial direction.

Morphology is a macroscopic perspective of the underlying molecular order and disorder, which causes efficiency losses through reduction in charge mobility and through barriers to energy transfer. Furthermore, when there is a large range of different packing motifs among a mixture of molecules, a range of species with different excited state energies will exist. Energetic disorder within the BHJ of organic photovoltaics has been shown to limit the capability of both charge transfer [59], [73], [100] and exciton harvesting [43], [59], [101]–[103] due to energy level traps.

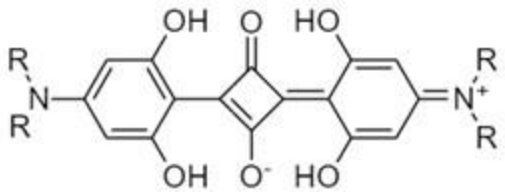


**Figure 1.7 – Example structure of a Squaraine molecule.**

Movaghar *et al.* considered the effect of traps on exciton harvesting as early as 1986 [104], with Athanasopoulos *et al.* showing theoretically how energetic disorder can reduce the exciton diffusion length by up to an order of magnitude in disordered polymers when compared to highly ordered conjugated molecules [101]. As the exciton spontaneously falls to lower energies with each progressive jump, the probability of finding a new site to hop to falls as the exciton nears the bottom of the energy distribution [101], [102]. Athanasopoulos *et al.* showed how disorder tends to reduce the FF and Jsc [100] even though it may increase BHJ surface area and enhance charge separation at the BHJ interface for low efficiency devices. [59], [100].

## 1.4 Squaraines

One material class offering several of the benefits required for eventual OPV commercialization is the Squaraine(SQ) class; an example structure is provided in Figure 1.7. SQs are produced by a simple synthetic route, a one-pot two-step synthesis, that makes high yields very affordable [17], [31], [105]. In addition to having a large intrinsic absorbance, SQ thin films absorb predominantly in the red and near-infrared wavelengths [31], [84] which aligns with the solar spectrum. Through modifications of SQ substituents, or *R* groups shown in Figure 1.7, the blending properties of SQs can be dramatically altered without substantial changes to their energy levels [54], [84], [106]. This is extremely powerful for OPV device testing, as it allows for a range of morphological structures spanning extremely well blended (with PCBM) to highly phase separated (from PCBM). Through their changing blending properties, poorer mixing tendency drives the formation of aggregates in select SQs [84], making them an excellent candidate for evaluation of the energy transfer properties in such aggregates. A final significant, yet unexplored benefit of SQs is that their molecular structure induces an intramolecular push-pull effect due to the electron

donating side groups and electron accepting central structure (D-A-D). This is comparable to the intramolecular push-pull effect of non-fullerene acceptors (NFAs) which tend to have an A-D-A type structure [58]. NFAs are prized due to improved material interactions with the donor so it could be hypothesized that similar behavior would occur between SQs and an appropriate intramolecular push-pull acceptor. The push-pull property of SQs could make them an excellent donor candidate to combine with similarly structured NFAs leading to a high efficiency cell at a low overall cost.

One of the most beneficial properties of SQs is that small changes to their structure can produce dramatic changes to the morphology of pure thin films. To explain, anilinic SQs are shown to preferentially stack in a slip-stack structure [84], [106] with varying molecular separation depending on their alkyl chain lengths [84]. These subtle changes to molecular packing structure dramatically affect the molecular environment and packing density in thin films. Because Squaraines preferentially pack in a slip-stack structure where the transition dipole moments of neighboring SQs are side by side, they exhibit H-aggregate characteristics [84], [90]. The formation of H-aggregates is a consequence of very tightly packed, well-organized, crystalline domains of SQ. As previously mentioned, H-aggregates are often identified by a blue-shifted broadening of the absorbance relative to the monomer. While this absorbance broadening and improved crystallinity should improve OPV performance, the fluorescence properties of H-aggregates may limit their energy transfer mechanisms. In accordance with theory, fluorescence from SQ H-aggregates is quantum mechanically forbidden due to a low energy dark state that is not coupled to the ground state [86], [88]. This lack of fluorescence is expected to limit energy transfer based on the previously described requirements of the most common EnT mechanisms. Furthermore, the small intermolecular separation of SQ crystals allows for coupling between the H-aggregate bright state and an intramolecular charge transfer (ICT) state in sufficiently ordered thin films [90]. Within the SQ crystal structure, the nitrogen atom of a SQ molecule is shown to be closer to the central ring of its nearest neighbor (5.21Å) than the intramolecular central ring (6.68Å) [106].

Confirmation of charge transfer H-aggregate formation is made by the double hump spectral motif previously shown in Figure 1.5. Fully aggregated thin films leading to the double hump spectral motif are further predicted to limit energy transfer as the new species also lacks fluorescence [107]. As such, several works from our group have investigated the effects of SQ phase separation to form large pure donor domains due to altering alkyl chain length, or by annealing, typically leading to lower device efficiency [54], [84], [106] though confounding variables, such as domain enlargement, have prevented conclusive confirmations of limitations to charge transfer H-aggregates.

The previous paragraph focused primarily on SQs in pure films, though the same properties apply to blends. Small functional group (molecular structure) changes also have a huge impact on SQ blending properties with OPV acceptors. These changes to their blending behavior can be used to produce a wide range of different BHJ morphologies with variation in domain size, purity, and crystallinity depending on how they interact with acceptors such as PCBM [84]. The difference in similar SQ blending properties allows the effects of morphology on device performance to be better isolated and studied. For example, when the R-groups of Figure 1.7 are butyl chains ($DBSQ(OH)_2$), the SQ has been shown to blend well with PCBM, leading to significant intermixing of donor and acceptor and minimal formation of isolated pure domains [54], [84]. In contrast, hexyl side chained SQs ($DHSQ(OH)_2$) phase separate almost immediately from PCBM at room temperature leading to large, pure, separated domains of both the acceptor and the donor [54], [84]. Additionally, further phase separation of SQs from the acceptor may be induced with thermal annealing [84].

With sufficient phase separation and enhanced packing density, the separation between neighboring SQs begins to shrink. Because of the previously discussed preferred packing behavior of SQs, poor blending and phase separation leads to the formation of H-aggregates and ICT coupled states in the SQ domains. Formation of these H-aggregates, and the eventual ICT coupling, is expected and has been shown to reduce overall device performance [84]. Specifically, devices utilizing $DBSQ(OH)_2$ consistently outperform those with $DHSQ(OH)_2$ as the donor [54], [84]. This

fall in performance of $DHSQ(OH)_2$ devices correlates with significantly more ICT state coupling and H-aggregate formation due to phase separation. The question remains, however, as to whether the H-aggregate and ICT state coupling are the source of decreased performance or if there is some other explanation such as the increased phase separation.

Recently, Zheng *et al.* identified energy transfer occurring preferentially from monomers to H-aggregates very rapidly [68], effectively suggesting these excited states are quickly moving into traps if these H-aggregates are unable to energy transfer towards the interface. In the same study, excitons continued to transfer into progressively tighter packed DHAs [68]. However, this study did not consider the behaviors of the charge transfer coupled H-aggregate on OPV performance which still requires investigation because theory suggests that these states should have limited energy transfer contributions. Therefore, it is suggested that this could be a significant opportunity for further research with notable impact on OPV and energy transfer theory.

## 1.5 Objectives

Commercialization of OPV necessitates that the efficiency of devices needs to be consistent for longer and they must be cheaper to produce [108]. As such, the field looks to predict and reach the intersection between manufacturability, efficiency, and cost [109]. The efficiency, lifetime, and cost of an OPV device is determined by a number of factors, one of which is the active layer morphology (or structure) [110]. It is clear that the morphology of the active layer both immediately after fabrication and throughout the device's lifetime is a performance-defining characteristic [79]. It is, however, the eventual thermal equilibrium morphology which must be optimized to define the lifetime of a device, yet most research focuses on initial performance, promoting higher efficiencies, without concern for long-term changes to the morphology which will undoubtedly alter efficiency. For this reason, accurate control of the morphology in both the kinetically stable state after fabrication and the thermally stable state after years of operation is a necessary challenge to consider and overcome. Thus, a primary objective of this work will be to develop improved

control and evaluation of the active layer morphology and its lifetime through alternative design strategies.

Because of a changing active layer morphology, the energy landscape of the materials that make up the active layer fluctuate. The relative packing density and orientation of molecules within determines the nature of the excited states [86], and in turn the energy transfer properties [41], of the thin film active layer. A necessary step therefore is to develop an accurate measurement of the relative populations of different states within an active layer. Through a combination of spectroscopic techniques, the packing densities of materials and predicted population of these states within the device may be accurately determined. Because their populations are dependent on the manufacturing and materials of the device, the previously developed morphology control may be used to generate a range of different populations. Comparing these identified populations in an active layer with the associated device efficiency is essential to improved device understanding. This work therefore further considers how types of excited states, and their ratios correlate with device performance.

Finally, predicted energy transfer properties of these various energy states are described by several key works. The foundational knowledge describes how aggregates of small molecules, and their orientations [86], [88], determine their energy transfer ability [41]. Specifically, it is predicted that select energy states, namely H-aggregates and ICTs, should be limited in their ability to energy transfer. The objective is to understand if these theories of energy transfer limitations of dark states are essential to OPVs. The question is if energy transfer limitations are truly detrimental to the performance of charge transfer coupled H-aggregates and corresponding devices. This outcome must be carefully considered since H-aggregates, if capable of significant energy transfer, could be beneficial for devices later in operational lifetimes. Should this be the case, its impact cannot be understated both in the impact of the claim on key theories and considerations in OPV fabrication. Therefore, the third and final objective is an experimental evaluation of key theoretical energy transfer properties of charge transfer H-aggregates and their influence on device performance.

# 2 Chapter 2. Experimental Methods

## 2.1 Materials, Solutions, and Films

**Materials.** Aniline based Squaraine(SQ) derivatives, a general structure of which was provided in Figure 1.7, were utilized throughout the research presented here. Specifically, 2,4-bis[4-(N,N-dibutylamino)-2,6- dihydroxyphenyl]squaraine ($DBSQ(OH)_2$) and 2,4-bis[4-(N,N-dihexylamino)-2,6-dihydroxyphenyl]squaraine ($DHSQ(OH)_2$), were synthesized in a one-pot, two-step procedure by Jeremy Cody's research group at Rochester Institute of Technology (RIT) [111]. The appropriate secondary amine had been purchased and condensed at reflux with 1,3,5-trihydroxylbenzene in a toluene/n-butanol (3:1, v/v) mixed solution. The resulting aniline intermediates were mixed with a half equivalent squaric acid in a second condensation reaction to produce the Squaraine derivatives, both of which are green solids. Squaraine derivatives have extinction coefficients over $10^5$ $cm^{-1}$ and band gaps of around 1.6 eV, making them excellent candidates as electron donors in OPV devices [84], [112]. Within the SQ molecule, the central ring behaves as an electron acceptor (A) while the outlying anilines act as electron donors (D) to give the overall molecule zwitterionic character evident in Figure 1.7 [113].

$PC_{61}BM$ ([6,6]-phenyl C61 butyric acid methyl ester, >99.5%) was purchased from SES Research and utilized throughout this work as an electron acceptor for OPV devices. $MoO_3$ (molybdenum trioxide, >99.5%) was purchased from Sigma-Aldrich and used as a hole transport layer between the Indium Tin oxide (ITO) anode and the active layer in all devices. All materials were stored in a $N_2$-filled glovebox and were used as received. In the context of this work, $PC_{61}BM$ is referred to as PCBM to be more concise.

**Solutions.** All solutions were prepared in chloroform (HPLC Plus, ≥99.9%), purchased from Sigma Aldrich, at a fixed combined material concentration of 15 g/L. Where necessary, deviations from this concentration were made to achieve an appropriate optical density for the UV/Vis measurement. Deviations, where explicitly stated, were obtained through either an adjustment to the prepared stock solution or through serial dilution. Solutions used for device fabrication and

UV/Vis-absorption measurements are defined by the weight percent of each material in the final blend. To achieve the desired blend ratios, materials are initially weighed as solids and then dissolved in an appropriate volume of chloroform to achieve desired concentrations. Solutions are heated to *ca.* 45˚C and are mixed by sonication for 20 minutes to ensure materials fully dissolve. No significant differences in solution absorbance were observed due to heating, demonstrating that there is no apparent negative chemical consequence from heating the materials to induce faster solvation.

**Films.** All thin films were prepared by spin-coating 60 μL of solution onto a 20 mm x 15 mm glass substrate, or 120 μL of solution onto a 1 in. x 1 in. glass substrate, at 1500 rpm for 30 seconds with a vacuum-free Ossila Spin Coater inside of a nitrogen ($N_2$) filled glovebox. Film thicknesses of around 100 nm were typical, as will be discussed further in chapter 3. When all subsequent film annealing treatments are described below, this indicates that the process was performed on a digital hotplate at a set temperature in the same glovebox, with hotplate temperature calibrated at a consistent location to within ±5˚C by an Etekcity Lasergrip 1080 Infrared Thermometer. Films were cooled following annealing and/or spin-coating by placing them onto a cold metal surface. Complete solvent evaporation was ensured by briefly placing the films under vacuum. Contact angle measurements completed on neat thin films were performed on a ramé-hart goniometer model 250 with deionized water as the reference liquid.

## 2.2 Characterization

### 2.2.1 UV/Vis-Absorbance Spectroscopy

UV/Vis-Absorbance Spectroscopy measurements were completed on a Shimadzu UV-2401PC spectrophotometer outside of the controlled $N_2$ environment of the gloveboxes. Several hours of uncontrolled air exposure were shown to have no notable impact on the optical properties of the films. For solutions, measurements were completed using a 1 cm pathlength Starna Cells quartz vial calibrated for a usable range of 170 to 2700 nm. For all solution measurements, serial dilutions were performed to achieve absorbance values below 1.5 for all spectral peaks. In solution

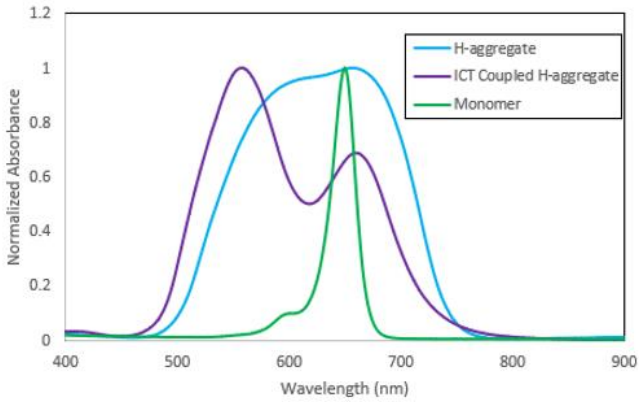


**Figure 2.1 - Example absorbance spectra of the monomer, H-aggregate, and intermolecular charge transfer coupled H-aggregate.**

absorbance measurements, SQs appear as a narrow peak at *ca.* 650 nm. For thin film absorbance measurements, SQs appear as either an isolated monomer peak (Figure 2.1-Green), a broad peak with a blue shoulder indicative of H-aggregates (Figure 2.1-Blue), as the double hump motif indicative of coupling between the H-aggregate and charge transfer state (Figure 2.1-Purple), or as a combination of the three depending on the extent of aggregation. Extent of aggregation is shown to be largely influenced by the weight ratio of SQ to PCBM and the temperature, or time, of any annealing processes. Increases in the PCBM fraction were shown to improve blending and break up SQ aggregate formation while increases in annealing temperature (time) induced further aggregation in an otherwise kinetically stable film. PCBM absorbs, in both solution and films, between the lower limit of our measurements at 300nm up to *ca.* 525nm with negligible absorbance at longer wavelengths.

When quantified, the populations of charge-transfer H-aggregate, Dimer H-aggregate, and monomer in each film were determined using the wavelength dependent, extinction coefficient, α, in units of $cm^{-1}$, for each species. The absorbance of a film is measured and governed by the following equation where d is the contributing film thickness, in cm, for each species.

$$A = \alpha d \qquad 2\text{-}1$$

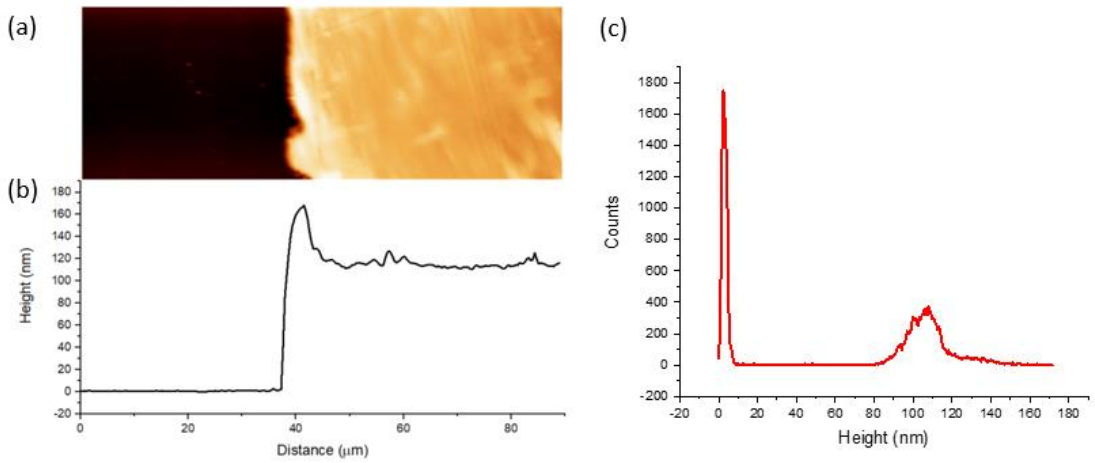


**Figure 2.2 – (a) Atomic Force Microscopy image (90 um x 32.7 um) displaying a lateral interface between the bare glass slide substrate (dark region) and spin-cast active layer (bright region). (b) Line profile showing the height of the material and (c) height histogram of the image used to determine the average height of the active layer relative to the substrate. This data was collected by our collaborator, Kirsten Burson.**

The effective thickness for blended active layers can be measured using an approach described by Heier *et al*., [114] who investigated the aggregates of cyanines in mixtures with PCBM. They measured various populations of both J- and H-aggregates after dissolving away either PCBM or cyanine, over time. They calculated the amount (in mol) of PCBM or cyanine in their thin original film samples through film dissolution, UV–vis measurements, and Beer–Lambert theory, as summarized by

$$A = \varepsilon c l \qquad 2\text{-}2$$

where $\varepsilon$ is the solution extinction coefficient of $DBSQ(OH)_2$ or PCBM (dissolved from the film), with units of L $mol^{-1}$ $cm^{-1}$, $c$ is the concentration of the solution, and $l$ is the path length of the cuvette. We target an approach similar to that of Heier *et al*. [114] to back calculate the amount of $DBSQ(OH)_2$ or PCBM on a given film. Casted films are first measured to determine the thin film absorbance. After this, films are submerged in a known volume of chloroform to redissolve the materials off the glass substrate. To ensure full dissolution, solutions with the substrate submerged are sonicated in the same procedure as described for previous solutions. Resulting solutions are then adequately diluted for a solution absorbance measurement. Based on the known $\varepsilon$ of each

molecule, the concentration of each (PCBM and SQ) in solution is determined and from that the moles of each molecule on the original film are calculated.

### 2.2.2 Atomic Force Microscopy

Atomic Force Microscopy (AFM) measurements were completed by the research group of Kristen Burson in the department of Physics at Hamilton College. For these AFM measurements, solutions were deposited on glass slides using the previously described procedure. Some material was removed mechanically, using a fine tipped q-tip or wooden stick dipped in isopropyl alcohol (IPA) or acetone, creating a clear lateral interface between bare substrate regions and regions with active layer materials as in Figure 2.2a and b. Film thickness measurements were performed with an Asylum MFP-3D AFM using Olympus AC160TS-R3 tips with nominal radius $r$ =7 nm, $k$ =26 N/m, and $f$ =300 kHz. Heights were established through a statistical approach using height histograms, as in Figure 2.2c, from at least 10 high-quality images of the interface from each sample and considering multiple samples for each ratio of materials in deposited solution. Film areas were established using the software ImageJ.

### 2.2.3 Kelvin Probe Force Microscopy

KPFM measurements were completed by the research group of Tonya S. Coffey in the department of Physics and Astronomy at Appalachian State University. Thus, scanning probe microscopy (SPM) measurements were acquired with a Bruker Icon SPM system in Bruker's PeakForce Kelvin Probe Force Microscopy (KPFM) mode using Bruker's PFQNE-AL probes. These probes have tip radii of roughly 5 nm, spring constants of ~0.8 N/m, and resonant frequencies of ~300 kHz. PeakForce KPFM combines PeakForce tapping mode with Frequency Modulated KPFM (FM-KPFM). In PeakForce tapping, the cantilever is oscillated well below its resonant frequency, tapping the surface at 2 kHz. This slower tapping frequency enables real-time analysis of the force curve, and the feedback loop is maintained at a peak force of a few picoNewtons on the photovoltaic samples, preventing damage to the samples and slowing the rate of material accumulation on the tip.

For most KPFM maps, it was only necessary to monitor the changes in the surface potential difference within a single image to discriminate between acceptor and donor regions. Whenever we needed to know the work function of the sample, we calibrated our PFQNE-AL probes using a silicon substrate patterned with gold and aluminum provided by Bruker. Because the work functions of Al and Au are well-known, we can use the measured potential difference between the tip and sample to infer the work functions of unknown samples. Bruker's Analysis software was used to find the average potential difference between the tip and sample for the regions of aluminum and gold in each calibration image. This yielded a constant offset which, when applied to KPFM images, would convert the relative surface potential differences into work functions for each sample.

### 2.2.4 Transient Absorption Spectroscopy

Transient Absorption (TA) measurements were completed by the research group of David W. McCamant in the department of Chemistry at the University of Rochester. For these TA measurements, a regeneratively amplified titanium: sapphire laser (Spectra-Physics Spitfire) was used to produce ~150 femtosecond laser pulses at a 1 kHz repetition rate. These pulses seeded a noncollinear parametric amplifier, which produced pump pulses centered at 550nm or 645 nm with a bandwidth of around 30 nm [115], [116]. The probe beam was created by focusing the fundamental 800 nm beam through a sapphire crystal to produce a white light continuum spanning 400−800 nm. A mechanical chopper was used to block every other pump pulse. After passing through the sample, the probe was dispersed by a grating spectrograph (Acton, 300 mm fl, 150 gr/mm) before reaching the CCD camera (Princeton Instruments, PIXIS 100BR). Before the sample, the white light spectrum was filtered using a dye solution (NIR800A, QCR Solutions Corp) to block residual 800 nm light from entering the spectrograph during data collection. The pump/probe cross-correlation was measured via the optical Kerr effect in a 1 mm glass slide [117] giving an instrument response of 100 fs or less. TA data were collected at three powers for each film to evaluate the effects of energy density on kinetics. To prevent photobleaching, the thin films

were translated rapidly in both the x and y directions via automated stages. Additionally, a bandwidth of ±15nm from the pump wavelength is neglected in all measurements due to detected pump photons scattered by the film artificially altering the TA signal in that range.

The TA signal was collected at parallel and perpendicular pump polarizations relative to the probe, to obtain the isotropic signal, $\Delta A_{ISO}$, calculated by

$$\Delta A_{ISO} = \frac{\Delta A_{\parallel} + 2\Delta A_{\perp}}{3} \quad 2\text{-}3$$

where $\Delta A_{\parallel}$is the signal for parallel polarization and $\Delta A_{\perp}$is the signal from perpendicular polarization. Transient anisotropy traces were also calculated via

$$\rho(t) = \frac{\Delta A_{\parallel} - \Delta A_{\perp}}{\Delta A_{\parallel} + 2\Delta A_{\perp}} \quad 2\text{-}4$$

## 2.3 Organic Photovoltaic Devices

### 2.3.1 Fabrication

**ITO Patterning.** Indium Tin Oxide (ITO) coated glass substrates (1.1 mm thick, 15 ohms/sq., 5 in. x 5 in.) purchased from Visiontek were first cleaned with successive baths in room temperature acetone, isopropyl alcohol, and deionized water followed by a 5-minute bake to ensure they were completely dry. Cleaned ITO plates were then transferred to the Semiconductor & Microsystems Fabrication Laboratory (SMFL) at RIT for photolithography processing. In the SMFL, ITO plates were first coated with HMDS P-20 in a two-step spin coating process of 500 rpm for 3 seconds followed by 2000 rpm for 45 seconds. Plates were then baked at 120˚C for one minute then allowed to cool to room temperature. Once cool, plates were coated with HPR 504 using the same two step spin coating process followed by a 90 second bake at 120˚C, then allowed to cool once again.

Plates were then covered by a mask and exposed to mercury broadband irradiation, calibrated to 25 mW/cm$^2$, for 20 seconds. Exposed photoresist was then developed in a CD-26 developer bath for 90 seconds followed by two successive rinses in deionized water before baking

at 120˚C for 90 seconds. Etching of exposed ITO was then completed in a 1:1 solution of deionized water and hydrochloric acid on a hotplate at 100˚C (note that typical etchant temperature was ~45˚C) for 10 minutes. Plates were then rinsed in acetone, isopropyl alcohol, and deionized water and allowed to air dry before being tested with a multimeter to verify etching was complete. Plates were then cut into 20 mm x15 mm substrates (outsourced to Joe West) for OPV device fabrication.

**Device Fabrication.** Cut substrates were first cleaned in acetone, isopropanol, and deionized water under sonication for 20 minutes. Substrates were subsequently subjected to a 20-minute bake to ensure dryness, followed by a 20-minute UV-ozone treatment in a model 18 UVO-Cleaner from Jelight. Substrates were then transferred into an $N_2$ glovebox and placed into a hole transport layer mask and loaded into a COVAP II thermal evaporator for a 12 nm $MoO_3$ deposition, performed at a rate of approximately 0.45 Å/s and a base pressure of <1E-6 Torr. Once complete, previously described active layer solutions were spin-cast onto substrates in the same manner as films (60μL at 1500rpm for 30 seconds), within the same $N_2$ environment. Any noted annealing of devices was completed immediately following the spin-coating process and with the same procedure as previously described for films. Devices were then transferred back into the thermal evaporator for a 100nm Al deposition at a rate of approximately 3 Å/s and a base pressure of <1E-6 Torr. This solar cell manufacture process would ultimately lead to a single batch producing 12 substrates (with a minimum of 3 substrates for each solution when different blend ratios were used in a batch), and each substrate would contain 8 devices, each of area 4.5 $mm^2$.

### 2.3.2 Device Performance Evaluation

**Current Density(J) – Voltage(V) Testing.** J-V testing of devices was completed within 24 hours of fabrication in the same $N_2$ environment used in their fabrication. A 450W Xenon arc lamp in a Newport 91192 AM1.5 solar simulator illuminated each device with a power density of 100 $mW/cm^2$ (calibrated against standard InGaP solar cells fabricated in NASA Glenn Research Center, Photovoltaics Branch 5410). Calibration was completed each time the system was turned on and allowed to warm up for 15 minutes. JV curves were produced by a LabVIEW program

developed in house which generated a voltage sweep from -2 to 2 volts in 0.02-volt steps on a Keithley 2400 sourcemeter with a four-point probe geometry. All statistical J-V data were generated based on data for a minimum of 20 devices for each material blend ratio.

**Spectral Response.** Carrier conversion Quantum Efficiency (QE) measurements were measured on a spectral response IQE200 system in the NanoPower Research Laboratory (NPRL) at RIT. Measurements were performed on one of the top four devices for selected blend ratios within 72 hours of fabrication. A monochromatic beam was formed by passing light generated by a halogen bulb through a monochromator and a beam chopper. The monochromatic beam was focused on an individual device with an area of ~1 mm. The device was held in place in a specially designed box fabricated by Chenyu Zheng, a previous member of our group, in collaboration with the RIT machine shop. The current produced by the device was sent to a Stanford Research System 570 preamplifier followed by a Stanford Research System 830 Merlin lock-in amplifier set to the frequency of the beam chopper. The resulting spectral response was obtained using a LabView program for wavelengths between 300 nm and 900 nm.

# 3 Chapter 3. Quantifying and Controlling Aggregate Populations in Organic Photovoltaics

The efficiency of all-small-molecule organic photovoltaic devices is significantly influenced by the nature of the excited state and morphology of the active layer. Squaraines are potential active layer materials for commercialization if their efficiency can be correlated with phase separation, miscibility, and crystallinity. However, there is currently no standard for defining the exact fractions of each excited state within the active layer. To address this issue, a self-consistent framework is proposed to connect the active layer morphology, excited-state populations, and device efficiency. Thin-film thickness is measured using atomic force microscopy, and the extinction coefficients of select excited state species are determined. With this information and the associated spectroscopic absorbance signals, a calibration curve is developed to accurately predict the fraction of squaraine molecules in each excited state for any device film. The relative populations of excited state species are determined for squaraine blends with varying amounts of PCBM. A population interchange between monomers in dilute mixtures, dimers in concentrated mixtures, and charge-transfer H-aggregates in pure/crystalline regions is identified. Measured efficiency of devices is shown to correlate with changing species populations. The proposed framework can be used to accurately determine excited state ratios in all-small-molecule organic photovoltaic devices, and changing excited-state populations can increase device efficiency.

## 3.1 Background Literature Review

OPV device efficiency depends on excited-state properties, energy transfer rate, and charge transport, [103], [118] and all of these depend on the morphology of the active layer materials, [84], [106] the solid-state packing, [68], [90], [91] and the mixing [54], [119], [120] of electron donor and acceptor materials within the BHJ active layer. Efficiency is also correlated with processing techniques [47], [121] since phase separation and morphology within the active layer are determined by such techniques. For example, as active layers are annealed, the donor and acceptor materials start to phase separate, and the purified domains start to crystallize. [122], [123] Changes

to both crystallinity and domain size for field devices must also be studied to understand their relative impact on efficiency. There is no current definitive framework for matching small-molecule donors and acceptors based on miscibility concepts. Furthermore, optimizing efficiency for donor/acceptor combinations requires tedious studies on the influence of several parameters such as blend ratio, thermal annealing, solvent additives, and solvent annealing. However, as we explore squaraine aggregation and active layer mixing, we consider the importance of miscibility, phase separation, and crystallinity for small-molecule devices.

A large body of work on the effects of processing and morphology already exists for polymer-based OPV devices [124]. A three-phase morphology has been described as valuable for polymeric solar cells, [125] combining regions of pure polymer donors, pure acceptors, and amorphous intermixed donors and acceptors [119]. However, spectroscopic differences in each polymer phase are subtle and masked. [126] On the other hand, spectroscopic characteristics of small molecules change substantially with new environments [127] and aggregation. By exploiting the radical change in spectroscopy of our active layer blend, which depends on the mixing of our donor $DBSQ(OH)_2$ and acceptor PCBM, we present a method to quantify species populations. Namely, the populations of the charge-transfer coupled H-aggregate (HCT), [90] of pure $DBSQ(OH)_2$ crystalline domains, the dipole–dipole (dimer) H-aggregate (DHA), [68] of well mixed blends of $DBSQ(OH)_2$ with PCBM, and the monomer (M), residing in dilute solid solutions of $DBSQ(OH)_2$ in PCBM. We aim to correlate the miscibility of donor/acceptor blends and PCE through a description of spectral signatures that pertain to each blend morphology. By determining the relative populations of HCT, DHA, and M, these populations can be correlated with the change in PCEs for a particular device.

In this work, an additional oversight is addressed within the OPV field that may be solved through our spectroscopic characterization. Thin film extinction coefficients, $\alpha$ in Equation 2-1, are rarely provided for OPV materials due to difficulty in nanometer resolution film thickness measurements. However, once each species is assigned an extinction coefficient, the population of

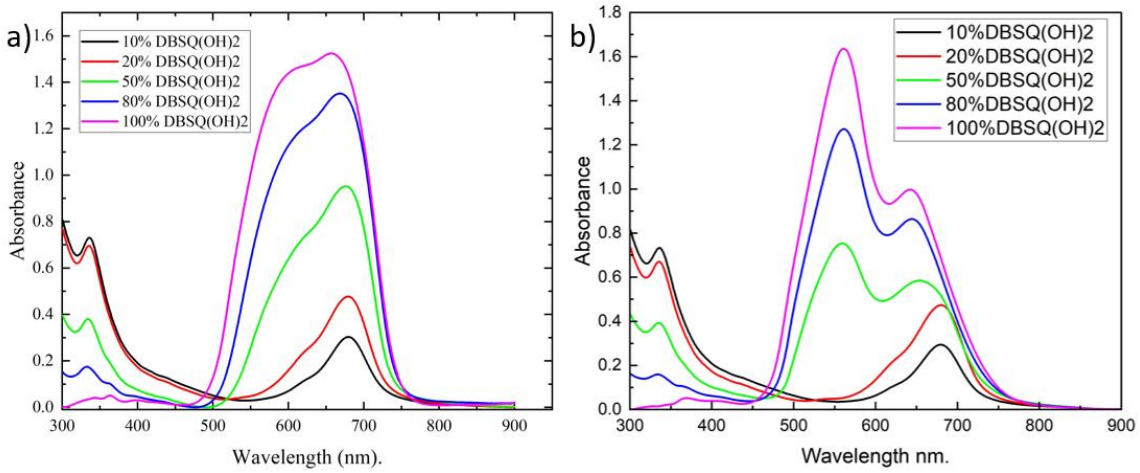


**Figure 3.1 - (a) Unannealed and (b) annealed $DBSQ(OH)_2$ films' absorbance. Percentages represent targeted $DBSQ(OH)_2$ weight% values, with the remaining percentage made up by PCBM.**

each species (HCT, DHA, or M) in a device can be quantified. We posit an approach to quickly determine the effective thickness of the active layer, independent of the blend ratio once the extinction coefficients are known and once the absorbance spectrum is measured. Subsequently, the effect of film thickness on device efficiency can be further studied, given the expectation that when active layers are too thick the number of charge carriers reaching the electrodes will drastically decrease [128]–[130] while thin active layers will reduce the photon absorption efficiency and concomitant current density.

We combine atomic force microscopy (AFM) measurements of the thickness of the film with an accurate indication of the number of moles of $DBSQ(OH)_2$ and PCBM for a series of films where the morphology is controlled through blend ratios and annealing processes. This allows exploration into the interchange of species from M to DHA to HCT. We use thin-film UV–Vis spectroscopy to indicate the relative contribution of each species to total film absorbance. We provide absorption spectra for different species, along with thin film extinction coefficients for M and HCT. We further use these results to provide insight on the incorporation of $DBSQ(OH)_2$ molecules within mixed PCBM:$DBSQ(OH)_2$ packing motifs. The determination of relative contribution of each species to the overall film makeup is then correlated with device efficiency to begin to interpret the contribution of each species to the performance of OPVs.

**Table 3.1 – Qualitative Assignment of spectroscopic features of Figure 3.1.**

| *$DBSQ(OH)_2$ wt.% in Sample* | *Unannealed* | *Annealed* |
|---|---|---|
| *10%* | M | M |
| *20%* | M + Trace-DHA | M + Trace-DHA |
| *50%* | M + DHA | DHA + HCT |
| *80%* | DHA | HCT |
| *100%* | DHA | HCT |

## 3.2 Quantifying Aggregate Populations

The absorption spectra of thin films used in this study are shown in Figure 3.1. In general, the peak at *ca.* 675 nm is assigned to the M, the feature that dominates at *ca.* 600 nm is assigned to the DHA, and the double hump peaks at ~560 and ~640 nm in the annealed samples both belong to the HCT species. The unannealed films in Figure 3.1a have a gradual shift from a peak at 680 nm for the 10% $DBSQ(OH)_2$ film (black) to 679 nm (at 20% $DBSQ(OH)_2$ (red) and 50% $DBSQ(OH)_2$ (green)), to 669 nm (for 80% $DBSQ(OH)_2$ (blue)), and ultimately to 658 nm (100% $DBSQ(OH)_2$ (magenta)). This blue shift represents an increase in the absorbance of the (600 nm) DHA species. The annealed films in Figure 3.1b show a sharp transition from a single peak at 680 nm (M) for the 10% and 20% $DBSQ(OH)_2$ films (black and red, respectively) to double hump peaks at 559 and 653 nm for the 50% $DBSQ(OH)_2$ film (green). Peaks at 561 and 643 nm are seen for the pure $DBSQ(OH)_2$ sample (100% squaraine, magenta). The lower energy peak in the annealed 50% $DBSQ(OH)_2$ (green) spectrum is broad and of a similar absorbance to the high energy peak, demonstrating remaining DHA population in this sample, contributing to the overall absorption. Notable spectral shifts, occurring from 50% to 100% $DBSQ(OH)_2$ films, further confirm that there is still DHA present in annealed 50 wt.% films, which has not been fully converted to HCT. All spectra follow the generalized trends shown in Table 3.1; the monomer gradually gives way to DHA, which as annealing occurs gives way to HCT as the percentage of squaraine increases. We first aim to quantify the relative contribution of the HCT state for each film. Despite limitations on accuracy that will be articulated below, the ideal outcome is a calibration curve of HCT population as a function of blend ratio for a variety of annealing conditions. We take two distinct

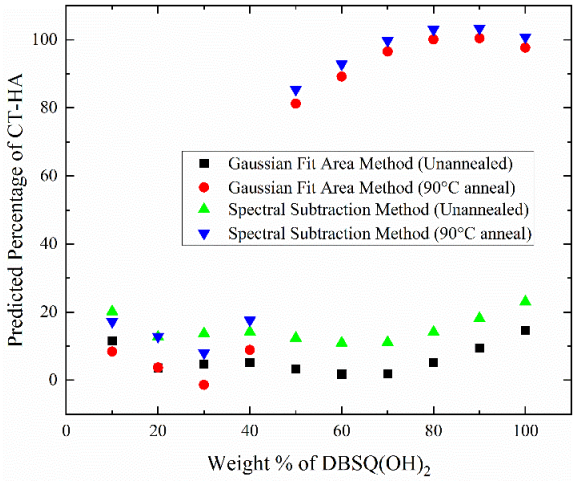


**Figure 3.2 - Predicted percentages of $DBSQ(OH)_2$ molecules in films associated with HCT species calculated by absorbance curve fitting methods.**

approaches to establish the HCT contribution, the results of which are shown in Figure 3.2, and which will be discussed after the methods used to generate them are introduced. These methods have different limitations, each of which is discussed in turn.

Introducing the "spectral subtraction" approach, we first subtract the known spectrum for PCBM from the as-measured spectrum. This is justified since the PCBM absorbs predominantly outside of the DBSQ(OH)2 absorbance region. We then define the spectrum of the 90°C annealed 100% DBSQ(OH)2 film to be that of the HCT state. However, the 90°C annealed 100% $DBSQ(OH)_2$ is not a perfect crystal and is broadened by discontinuities and local morphology changes, which therefore places a limit on the accuracy of our determination of the HCT contribution. We subtract this defined HCT spectrum, multiplied by a coefficient that we vary so as to target an absorbance average of zero for regions in the 480–570 nm range. The resulting spectra from these subtractions are presented in Figure A8.1. The coefficients used to arrive at these baselined spectra are divided by the known weight percent of $DBSQ(OH)_2$ in the sample, intended to normalize them and provide the "Percent of $DBSQ(OH)_2$ that is $HCT^b$" for each blend ratio. Both the coefficient and the normalized $\%DBSQ(OH)_2$ that is HCT are shown in Table A8.1. The $\%DBSQ(OH)_2$ that is HCT data are plotted (black squares) in Figure A8.2. We note

that the baseline after subtraction never recovers uniformly to zero due to spectral broadening depending on molecular environment. The crystal packing, and concomitant absorbance, of an ideal species is disrupted by local imperfections, PCBM "impurities", and by smaller domain sizes. In addition, DHAs are particularly sensitive to molecular orientation, separation distance, and PCBM mixing as described earlier. To quantify this error, we subtracted our defined HCT spectrum such that baseline values summed to zero for six different wavelength windows, 550–570, 540–570, 530–570, 520–560, 500–560, and 480–560 nm. These windows were selected around the high energy peak of the HCT absorbance while DHA absorbance exists mostly at longer wavelengths. Absent of HCT and PCBM, we expect a zero baseline to naturally occur in the range 480–570 nm. Subtraction coefficients for all these cases were then averaged. Larger wavelength windows demonstrated greater accuracy for smaller $DBSQ(OH)_2$ weight percent films while smaller wavelength windows demonstrated greater accuracy for larger $DBSQ(OH)_2$ weight percent films. The uncertainty is a consequence of absorption features that slightly vary for all of PCBM, HCT, DHA, and M such that perfect deconvolution is not possible. We again note how the absorbance spectrum will change when the nearest neighbor proximity decreases with the increased concentration of $DBSQ(OH)_2$ [68]. The uncertainties are provided in Table A8.1.

A second "Gaussian fit" approach to quantify HCT contribution is completed by first fitting all the measured spectra, after PCBM subtraction, to two Gaussian functions. The spectrum for a sample of pure M, DHA, or HCT could each be fit to two Gaussian peaks such that any blended sample would be better fit with six Gaussian peaks on a more complete underlying model. Yet, the objective is to parameterize the spectra with two Gaussians and to prevent overfitting. Therefore, the fits to two Gaussian peaks effectively provide an appropriate number of parameters, which describe (i) the peak position, (ii) area under each curve, and (iii) the width of Gaussian. Tables of the parameters of these fits (all made to a chi-squared value of $<1 \times 10^{-6}$) are presented in Table A8.2, Table A8.3, and Table A8.4. Given that the ~560 nm peak, when

present, is solely a result of HCT absorbance, we explore the area of that peak, the data for which are provided in Table A8.1, labeled "% of DBSQ(OH)2 that is HCT[d]". These values are plotted against wt % $DBSQ(OH)_2$ in Figure A8.2 for annealed films. However, for the unannealed films and for low wt. %$DBSQ(OH)_2$ annealed films, there is no ~560 nm peak so we consider peak position of the low energy Gaussian fit, given the trends seen in Figure 3.1 for all films. The high energy (low wavelength) peak positions and low energy (high wavelength) peak positions are plotted respectively in Figure A8.3.

The low energy peak position in Figure A8.3 is closely scattered around 682 nm from 10% $DBSQ(OH)_2$ to 70% $DBSQ(OH)_2$. A small but steady linear decrease is observed from 682 nm at 70% $DBSQ(OH)_2$ to 678 nm at 100% $DBSQ(OH)_2$ in the unannealed films. A similar trend is observed for the films annealed at 90°C, from 657 nm at 50% $DBSQ(OH)_2$ to 651 nm 80% $DBSQ(OH)_2$. Since from Figure 3.1a, the 100% $DBSQ(OH)_2$ 90°C annealed sample shows a low energy peak at 643 nm, we expect the peak position to correlate with HCT population. Two different slopes can be fit to each of these two linear trends. We note that the y axis in Figure A8.3 is the empirically determined peak position and x axis is the blend ratio; Gaussian fitting and parametrization is simply used here to describe the trends in a quantifiable way. In Figure A8.3 we demonstrate peak position as a function of blend ratio, but ultimately we desire a measurement of the contribution of HCT as a function of blend ratio.

To build that calibration curve of predicted percentage of HCT versus blend ratio, we plot in Figure A8.4 the wavelength of the low energy peak as a function of the percentage of HCT, both from the spectral subtraction approach and from the peak area parameterization approach. We note that this empirical description seems well-described by a straight line. We do not explain here the origins of the linear correlation, but each slope in Figure A8.4 is fit by linear regression and is a measure of the change in wavelength of the low energy peak per percentage fraction of HCT contribution. Hence, we can predict the percentage fraction of HCT as a function of weight percent of $DBSQ(OH)_2$ for each annealing condition by assessing the absorbance features of the spectrum.

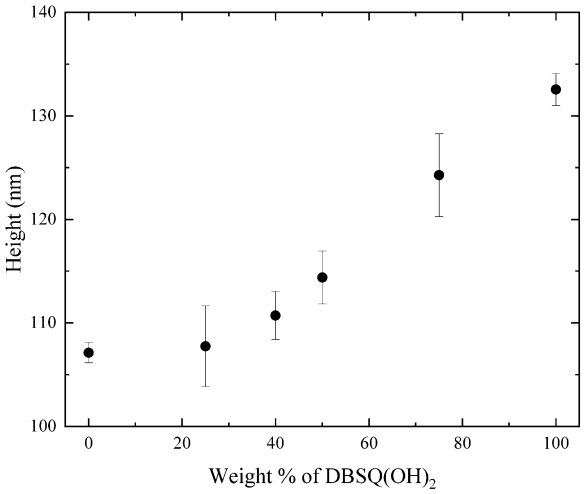


**Figure 3.3 - A plot of the average height of films of various weight percent of $DBSQ(OH)_2$, with PCBM being the other component in the binary blend. Error bars represent the standard error attained from multiple measurements from different film regions and distinct samples.**

The results are the calibration curves generated in Figure 3.2 (Figure A8.5), based on both the HCT spectrum subtraction method and the Gaussian peak area parametrization method. We note the limited data in our measurements, the nature of our approach, and how the percent error of the predicted percent fraction ranges from 7–28% depending on the method used to determine that HCT percentage. However, we have developed a guide to obtain reasonable estimates of the percentage of all $DBSQ(OH)_2$ molecules that are contained in HCT for a given blend ratio of $DBSQ(OH)_2$ and PCBM.

## 3.3 Extinction Coefficient of the HCT

We further sought to measure the extinction coefficients of each species, which would provide an indirect measure of the effective thickness and proportion of $DBSQ(OH)_2$ molecules associated with each species after a simple absorbance measurement. Here, again, the annealed 100% film was assumed to yield a fully crystallized HCT [84], [90]. Film thicknesses were measured for each blend ratio and averaged across multiple measurements to provide appropriate error bars. Results for annealed samples are presented in Figure 3.3. A measured thickness of 134 ± 1 nm of a 100% $DBSQ(OH)_2$ annealed film, $d_{HCT}$, therefore yields the extinction coefficient $\alpha_{HCT}$ according to

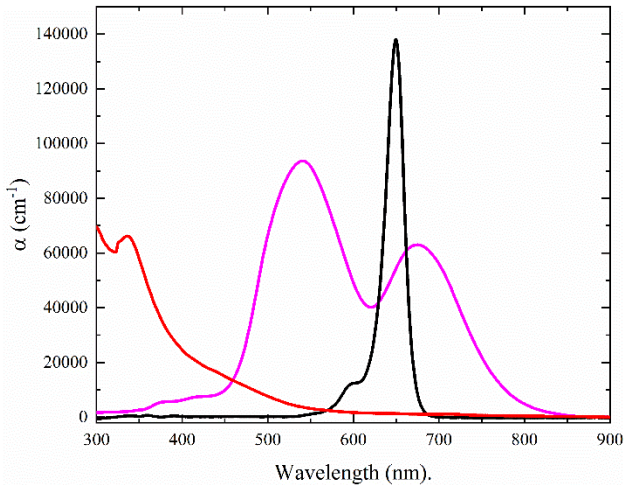


**Figure 3.4 – Extinction coefficients of SQs associated with HCT (Magenta), M (Black) and PCBM (red).**

Equation 2-1, which is plotted as a function of wavelength in Figure 3.4, (magenta) with maxima of 93,682 and 63,054 $cm^{-1}$ at wavelengths 541 and 675 nm, respectively.

With this extinction coefficient, we can now determine the effective thickness associated with the HCT species for any device. (The effective thicknesses can be derived from the HCT absorbance contribution using the spectral subtraction method.) Furthermore, since the squaraine amount (moles) in any film may be determined by dissolving that film, we seek to determine the average number of squaraines in a single HCT as part of the larger population of HCTs in a blended film. To address this, we first consider that the oscillator strength must be the same for a single squaraine independent of whether that squaraine is coupled with a second squaraine (DHA) or a set of squaraines (HCT) [40], [131]. (This assumption is valid so long as the molecules and aggregates are isotropic within the film; monomers and DHAs are isotropically arranged and the size of the "crystals" is considered so small with the sample being essentially a randomly oriented powder-like material with nanoscopic domains.) We assume equivalence between the integral under the curve of the extinction coefficient versus frequency (energy) per HCT squaraine molecule, and that same integral for the single squaraine monomer [132]. In Equation 3-1, we connect the extinction coefficient and molar absorptivity (from the Beer–Lambert law); we assume an equivalence

between the extinction coefficient for the monomer and the molar absorptivity multiplied by the molar concentration of the squaraine species in a (solid) solution, where PCBM is the solvent.

$$\int_{band} \alpha_{CT-HA}(eV) = \frac{x n_{SQ,mon}}{V_{PCBM}} \int_{band} \varepsilon_{mon}(eV) \quad 3\text{-}1$$

Therefore, in Equation 3-1, x is the number of molecules of $DBSQ(OH)_2$ per HCT species, $n_{SQ,mon}$ is the number of moles of monomer in a solid solution (PCBM film) and $V_{PCBM}$ is the volume of the PCBM host. When the weight percent of $DBSQ(OH)_2$ is an order of 1 wt.%, its contribution to the volume of the film is assumed to be negligible. Armed with the number of moles of squaraine in a 1% $DBSQ(OH)_2$ film, the volume of the film, the thickness of the film, and the absorbance of the squaraine, the extinction coefficient for the monomer can be determined. Once that extinction coefficient for a monomer in a solid solution is known, the number of squaraines in a single aggregate, x, is determined to be 5±1; we fully expand the details of the calculation in the Appendix. We also include equations to calculate the relative concentrations of each species M, DHA, and HCT, noting how the total numbers of $DBSQ(OH)_2$ and PCBM molecules are determined using simple Beer–Lambert law analysis after redissolving any given films.

We now turn to a discussion of film density and mixing for different blend ratios. After measuring the thickness and area of each film, the film can be dissolved such that the exact mass of $DBSQ(OH)_2$ and PCBM can be known. We note here that the density of PCBM does not change after annealing, which points to thickness changes for each film upon annealing being attributed to density changes in $DBSQ(OH)_2$. Data for annealed and unannealed films are presented in Figure A8.6. For annealed films, with film measurements shown in Figure 3.3, the film thickness increases overall as the $DBSQ(OH)_2$ weight percent increases and PCBM weight percent decreases. This trend is expected given PCBM's higher density. Yet, with low $DBSQ(OH)_2$ weight percent, we see a plateau before the thickness rises again beyond 25 wt.%. These data therefore deviate from a linear tie-line between 0%DBSQ(OH) 2 and 100% DBSQ(OH)2 that we would expect for two materials with fixed densities. The observed thicknesses are consistent with the incorporation of

the smaller $DBSQ(OH)_2$ molecules into PCBM, at blend ratios below 25% by weight of $DBSQ(OH)_2$. The experimentally determined lattice constants for PCBM crystals at 100 K are $a$ =1.347 nm, $b$ =1.51 nm, and $c$ =1.901 nm with $\alpha$ =90°, $\beta$ =106.9°, and $\gamma$ =90° (100 K) with a volume of 3.709 $nm^3$,[133] even though we recognize that PCBM will actually be found in an amorphous state in our samples [134]. The experimentally determined $DBSQ(OH)_2$ lattice constants are $a$ =0.5169 nm, $b$ =1.0847 nm, and $c$ =1.3538 nm with $\alpha$ = 77.165°, $\beta$ =79.143°, $\gamma$ =76.324°, a calculated density of 1.290 $g/cm^3$, and a volume of 0.7116 $nm^3$ [84]. The smaller volume of $DBSQ(OH)_2$ may allow for incorporation into the interstices of the larger PCBM unit cell. This leads to our interpretation that $DBSQ(OH)_2$ mixes well with PCBM.

## 3.4 Correlation of Device Efficiency with Aggregate Populations

A critical goal of this work is to correlate the extent of aggregation with the performance of $DBSQ(OH)_2$ photovoltaic devices. Previous work from our group has investigated energy transfer through distributions of squaraine DHAs at various concentrations [68]. Since energy transfer is critical for successful operation of BHJ devices, a logical next step is to correlate the nature and populations of all present excited states and their impact on device efficiency. A range of devices were made to complement the spectroscopy data in this work.

A plot of average short circuit current density ($J_{SC}$) for a given batch of devices as a function of $DBSQ(OH)_2$:PCBM blend ratio is shown in Figure 3.5a. For unannealed films, the greatest average $J_{SC}$ comes from devices with around 35% $DBSQ(OH)_2$, with all devices below 40% $DBSQ(OH)_2$ performing similarly. The average $J_{SC}$ then progressively drops off as the $DBSQ(OH)_2$ weight ratio is increased to 50 and 75%. The $J_{SC}$ data for the best devices in the sample set are presented in Figure 3.5b, showing identical trends to the averages. The trends for the average over all devices mirror those for the best devices, for which the data are provided in Figures 3.5b($V_{OC}$), 3.5c(FF), and 3.5d(PCE). The average open-circuit voltage ($V_{OC}$), fill factor (FF), and PCE data are shown in Figure A8.7, Figure A8.8, and Figure A8.9.

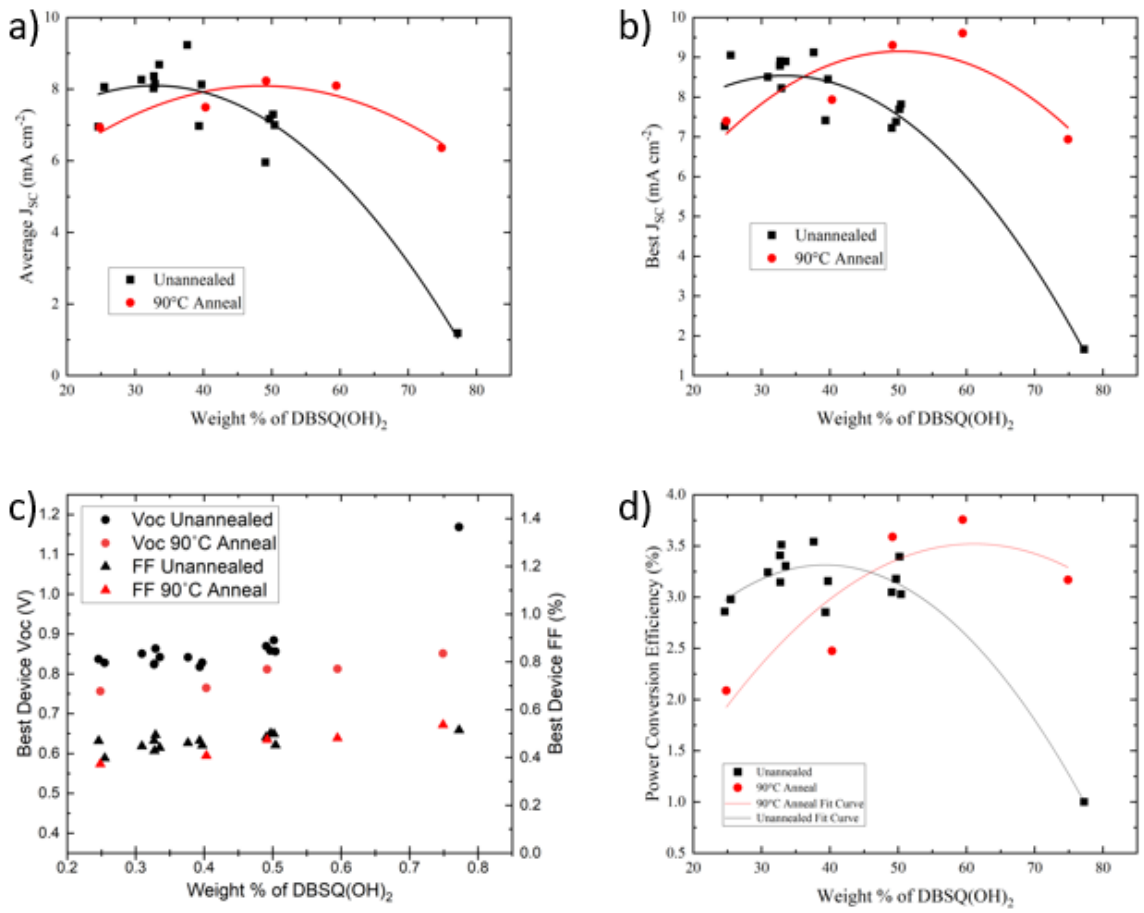


**Figure 3.5 – The a) average and b) best short circuit current density, c) best fill factor and open circuit voltage, and d) best power conversion efficiency measured for a series of DBSQ(OH)$_2$:PCBM devices with varying blend ratio, unannealed in black and annealed in red. 2$^{nd}$ order polynomials, where provided, are displayed solely as a guide to the eye for de-scribed trends; all reported values in the text are based on actual device measurements.**

For unannealed devices, the best device $V_{OC}$ stays more or less constant at about 0.8 V and a slight increase in the FF from about 0.4 to about 0.45 is observed as the DBSQ(OH)$_2$ weight percent increases (Figure 3.5c). The best device PCEs are those with a blend ratio of about 30–40 wt % DBSQ(OH)$_2$ for the unannealed devices, which largely follows $J_{SC}$, the primary PCE driver. The dominant influence of $J_{SC}$ on PCE is further supported by the gradually increasing $V_{OC}$ of the unannealed devices that still fails to improve a PCE of 75 wt.% DBSQ(OH)$_2$ devices relative to lower wt % cases.

For annealed films, we see a slightly different story. We see a peak $J_{SC}$ at 50 wt.% DBSQ(OH)$_2$ in Figure 3.5a, and the average $V_{OC}$ hovers just below 0.6 V (Figure A8.7), some 0.2

V lower than that of the unannealed devices. The average FF (Figure A8.8) increases from 0.3 at 24 wt.% DBSQ(OH)$_2$ to 0.37 at 49 wt.% DBSQ(OH)$_2$ and only rises above 0.4 when wt.% DBSQ(OH)$_2$ increases to 75%. However, the combination of $J_{SC}$, $V_{OC}$, and FF leads to a PCE maximum at 59 wt. % DBSQ(OH)$_2$ for both the best device and the average of all devices measured, as shown in Figure 3.5d and Figure A8.9, respectively. The optimal 59 wt.% DBSQ(OH)$_2$ blend ratio for annealed films is substantially higher than the 38 wt.% DBSQ(OH)$_2$ for optimal PCEs in unannealed DBSQ(OH)$_2$:PCBM devices, with $J_{SC}$ driving the efficiency, throughout. We now turn to interpretation of device performance in terms of the expected excited-state population distribution and the perceived mixing of DBSQ(OH)$_2$ and PCBM.

We start by considering the expected populations of M, DHA, and HCT at each of the peak efficiencies, at *ca.* 40 wt.% DBSQ(OH)$_2$ for unannealed films and *ca.* 60 wt.% for the 90°C annealed films. For the 40 wt.% DBSQ(OH)2 unannealed films, we expect 4–13% HCT, from Figure 3.2, and a small percentage of M. We expect the dimerization of DBSQ(OH)$_2$ to be substantial and we expect DBSQ(OH)$_2$ to be well mixed with PCBM. For the 60% DBSQ(OH)$_2$ 90°C annealed films, we propose approximately 90% HCT and 10% DHA (Figure 3.2, Table 3.1). These populations can be interpreted to mean that DBSQ(OH)$_2$ is largely phase separated, but the domain size will not be as large as that for a 100% SQ:PCBM annealed film, based on drawing parallels to domain size studies provided elsewhere. [54], [68], [84], [106]

In unannealed films, the highest efficiencies are measured in DBSQ(OH)$_2$ concentrations with high mixing of squaraine and PCBM in addition to a significant number of DHAs. We recognize from the data shown in Figure 3.2 that the percentage of HCT contribution is on the order of 4–13%. Therefore, in unannealed films, the efficiency is high when there is a significant amount of mixing of DBSQ(OH)$_2$ and PCBM. Yet, as the DBSQ(OH)$_2$ weight percent increases, the degree of DBSQ(OH)$_2$ mixing decreases, along with device efficiency.

Annealing increases the rate of phase separation and drives the formation of HCT in DBSQ(OH)$_2$ domains. Phase separation is driven thermodynamically by the enthalpy of interaction

between components and the entropy of mixing. Phase separation is also driven kinetically since, at higher temperatures, mass transfer is likely when heat energy can be distributed in translational motion. When the $DBSQ(OH)_2$ concentration is increased such that the SQs are no longer accommodated in PCBM, the devices perform optimally only when there is substantial evidence for aggregation and HCT formation, as is the case for our annealed devices with $DBSQ(OH)_2$ weight% exceeding 40%. The extensive phase separation achieved in higher weight% devices combined with thermal energy from annealing is expected to produce large, crystalline domains. The improved crystallinity and concomitantly mobility likely overcome any potential stifling of exciton diffusion due to HCT or large domain formation.

## 3.5 Discussion

At low temperatures, and a low $DBSQ(OH)_2$ percentage, mixed samples are more likely from spin-casting where geometry is "frozen-in". Some mixing will be maintained at subtly higher temperatures because of the entropy contribution. However, as temperatures increase to enable mass transport, some phase separation will be likely but may continue to trade off and balance with the higher entropy of a mixed state. As the blend ratio of $DBSQ(OH)_2$ increases, phase separation will continue to be driven thermodynamically, and an equilibrium phase separation and crystallinity for a given blend ratio will be achieved more quickly as the temperature of annealing increases. This work demonstrates how some level of mixing is valuable in select molecular devices, as in the highest efficiency unannealed films at *ca.* 40 wt.% $DBSQ(OH)_2$, in the same way that it has been demonstrated to be important for polymer devices. [135]

We also recognize a trade-off between exciton diffusion and charge mobility. In well mixed samples, the distance required for exciton diffusion to a BHJ interface is short, while the charge mobility would expectedly be low. On the other hand, when phase separation is substantial then the charge mobility is expected to be higher, and the efficiency of the device may remain high, despite larger distances for excitons to travel in order to reach domain boundaries. This is a possible explanation for the highest efficiency annealed films at *ca.* 60.wt % $DBSQ(OH)_2$. The device data

we present support the idea that phase separation and crystal packing ultimately help the efficiency of the device (through short-circuit current) despite the formation of intermolecular charge transfer coupled H-aggregates for which fluorescence would be quenched [68] and therefore for which energy transfer and exciton diffusion may be stifled. When we increase the concentration of $DBSQ(OH)_2$ such that $DBSQ(OH)_2$ molecules are no longer accommodated in PCBM, then the devices only perform well when there is substantial evidence for aggregation, demonstrated by the spectroscopic signatures of HCT, and calling into question the effects of HCT energy transfer limitations on device efficiency.

When we infer a mixing of $DBSQ(OH)_2$ and PCBM with AFM thickness measurements, we can confirm the importance of morphology as a critical attribute for all materials used in OPV. The entropy of mixing has a more dominant influence in molecular systems because the molecules have larger degrees of translational freedom. The enthalpy of mixing is more important as active layer materials become smaller in size. There is therefore a trade-off between molecules and polymers. With molecules, the packing properties are more closely associated with the intrinsic properties of those molecules derived from their functional groups. For polymers, the packing properties are influenced significantly by the molecular weight and associated restricted translational degrees of freedom.

## 3.6 Conclusions

This chapter demonstrates the power of spectroscopy for measuring the relative populations of species formed by aggregation and molecular mixing, or packing, in BHJ blends. Morphology measurements are typically based on microscopy or expensive X-ray diffraction techniques and in either case require substantial expertise in data interpretation and multiple measurements to obtain an appropriate statistical confidence in the conclusions. UV–vis spectroscopy is found in every university Chemistry building in the United States, if not the world, and when spectroscopy can be measured for small molecules like squaraines, for which there is a steady change in spectra with molecular packing, then these spectra can provide ready information to help understand the

importance of morphology and mixing on BHJ device efficiency. A second important recognition and conclusion from this chapter is that there may be two or more high efficiency blend ratios for a particular active layer combination. Specifically, one of these high efficiency blends is composed almost entirely of charge transfer H-aggregate of the SQ donor after annealing. Given that all films will move toward a stable thermodynamic equilibrium morphology after working for long hours in the field, we strongly recommend that production engineers work toward blend ratios for annealed films. This work further demonstrates how useful squaraines are for evaluating two or more different optimal blend ratios.

# 4 Chapter 4. Morphology Optimization and Excited State Disruption with Ternary Blends

Organic photovoltaic (OPV) devices will often degrade substantially with use in the field due to changes in active layer morphology associated with long-term demixing away from a kinetically stable pristine device. With Squaraine-Fullerene blends, the formation of H-aggregates will theoretically induce energy transfer limitations. However, questions remain unanswered about device implications of H-aggregates and ICT state coupling and concomitant phase separation. To address this, we consider here the incorporation of two different SQ donors, with different blending properties along with the PCBM acceptor. These will be combined in a 2 donor, 1 acceptor ternary blend of two Squaraines in a ternary blend with a fixed quantity of fullerene acceptor to better control active layer morphology by Squaraine intermixing leading to control over the extent of aggregation and changing excited state populations. While the two SQs have radically different behaviors in how they will blend with the acceptor, they also have similar crystal structures which is predicted to promote excellent blending with each other. The Squaraine which blends well with PCBM, is therefore hypothesized to be capable of breaking up pure SQ domains by acting as a surfactant between the poorly mixed Squaraine and the PCBM during casting. Morphological changes are inferred through absorbance spectroscopy, by known differences between the spectra of the aggregate and the monomer, and with kelvin probe force microscopy. The secondary Squaraine is shown to act as a form of surfactant, enhancing mixing between the primary Squaraine and the fullerene; suggesting that morphology changes opposite of annealing may be accessed through changing material combinations. Devices made from varying Squaraine-Squaraine-Fullerene blend ratios are measured for efficiency, thereby providing a measure of the relative importance of both morphology and H-aggregation on that efficiency. Data reveals that H-aggregates are not inherently bad for device performance but, rather, it is the co-existence of a multitude of species which is problematic, reducing power conversion efficiency by upwards of 15%. This raises concern for other OPV devices as the natural annealing of field operation induces

aggregation, changing morphology, and a similar potential co-existence of incompatible species. Because OPV devices are expected to undergo significant heating over the course of their operation, thermal annealing is used to predict long-term implications of morphology changes on device performance, and further elucidate the effect of aggregates on OPV efficiency.

## 4.1 Background Literature Review

Bulk heterojunction (BHJ) organic photovoltaics with an optimized stable morphology offer highly efficient solar cells with a variety of applications [4], [9], [16], [136], [137]. Recent advances in efficiency leading to values in excess of 18%[138]–[140] are achieved through accurate control of active layer morphology. Excellent morphology control leads to a balance between the competing device assets of exciton separation and charge mobility [71], [79], [110]. A morphology of small well-mixed domains lends itself to efficient exciton separation due to a large BHJ surface area and a shorter average distance to the interface [141]. Charge mobility, however, is shown to benefit from large pure domains which often provide longer, uniform diffusion pathways [142]. Striking a balance between these two morphology characteristics is essential to enhancing device efficiency [110]. Yet, lab-based device optimization in as-produced devices may carry no-value because the annealing effects of long-term high-temperature field operation will undoubtedly alter the morphology and molecular packing behaviors. Device morphology, and concomitant efficiency, must therefore be optimized for the full lifetime of application [12], [143].

Increasing thermal energy from field operation is expected to enhance phase separation within the active layer of organic photovoltaics [143] when kinetically stable devices are manufactured. A second consequence of phase separation is a tighter molecular packing order as molecules aggregate, changing the molecular photophysics [87]. As phase separation and reorganization occur, new energy levels create variability in the energy landscape the exciton must traverse to reach the BHJ interface, increasing in the density of traps [59] within the active layer. Increased

trap density halts the diffusion of nearby excitons to the interface and reduces the probability of separation.

While thermally stable polymeric materials have dominated as active layer components in recent years [18], [71], an effective alternative is the utilization of small, highly conjugated molecules [17], [141], [144], [145]. Small molecules offer potential for simplistic synthesis, with intrinsic batch to batch consistency at a reduced cost [17], [144]. The initially stable morphology in spin-cast thin films can vary, however, between otherwise very similar small molecules such as Squaraines [84]. The length of the squaraine anilinic alkyl sidechains influences both the drive for short-range packing, [68], [84], [106], [146] and the extent to which the material mixes with the chosen acceptor, [6, 6]- phenyl-C61-butyric acid methyl ester (PCBM). For example, 2,4-bis[4-(N,N-dibutylamino)-2,6-dihydroxyphenyl]squaraine ($DBSQ(OH)_2$) blends well with PCBM, leading to smaller domains, with limited dimer H-aggregate (DHA) formation, and higher average device efficiency [68], [84], [146]. In contrast, when blended with PCBM, 2,4-bis[4-(N,N-dihexylamino)-2,6-dihydroxyphenyl]squaraine ($DHSQ(OH)_2$) promotes larger, pure Squaraine domains with tight packing that prompts coupling between the DHA and the charge transfer species (HCT) [84], [106]. Rapid phase separation of $DHSQ(OH)_2$ from PCBM during spin-casting leads to aggregate formation, larger domains, and correlates with lower device efficiency [84]. Despite the extensive analysis of both Squaraines, questions remain as to whether the nature of the excited state (HCT, DHA, and monomers) or domain size differences is the primary cause for the difference in performance for devices made from each of the two Squaraines [68], [146]. We therefore look to further explore the impact of DHAs, HCTs, and domain size on device performance through ternary blends of PCBM, $DBSQ(OH)_2$, and $DHSQ(OH)_2$.

Excellent mixing between $DBSQ(OH)_2$ and $DHSQ(OH)_2$ is predicted as both molecules are from the same family and have similar molecular weights. A tightly packed morphology when mixed is expected based on their similar crystal dimensions and preferred slip-stack packing [84].

Films made to include a second Squaraine ($DBSQ(OH)_2$) that mixes well with the first ($DHSQ(OH)_2$) should reduce populations of pure $DBSQ(OH)_2$ or pure $DHSQ(OH)_2$ H-aggregate excited states. Additionally, because $DBSQ(OH)_2$ also mixes well with PCBM, it may act as a surfactant between $DHSQ(OH)_2$ and PCBM, enhancing blending and producing smaller domains than for otherwise binary $DHSQ(OH)_2$:PCBM films. Hence, through changing the ratio of the two Squaraines in a ternary blend device, we explore the relative importance of the excited state and domain size through a continuum of morphologies. We utilize a ternary blend with a fixed ratio of the PCBM electron acceptor while varying the relative ratios of $DBSQ(OH)_2$ and $DHSQ(OH)_2$ in the fixed fraction of Squaraine electron donor.

Incorporation of any third material to form a ternary blend organic photovoltaic can have a dramatic impact on cell properties, specifically on the morphology of the active layer [147]. The introduction of a third active layer material to form a ternary blend, while altering things like absorbance, charge pathways, and favorable exciton diffusion behaviors [148], [149], also alters the mixing of the active layer, having solvent additive like characteristics [35]. Several groups have shown how small molecule incorporation with polymeric donors in a ternary blend can drastically influence device morphology and performance [55], [150], [151]. For example, Zhang *et al*. identified how the combination of two miscible donors, a small molecule and polymer, formed an alloy with a beneficial morphology by purification and enhanced crystallinity of the donor domains leading to higher hole mobility and overall better device efficiency [152]. Additionally, Liang *et al*. used a polymeric donor as an additive at 4 wt% leading to a small increase in efficiency, for which a key explanation was the ability of the miscible polymer to reduce domain size and improve phase continuity within the BHJ, acting as a binder of the donor and acceptor at the interface. [153] However, research is much more limited for all-small-molecule (ASM) ternary blends and morphological effects. Tang *et al*. showed how an ASM ternary blend with two donors of similar chemical structure and different crystalline behavior could increase performance by enhancing

absorption, suppressing recombination, and optimizing morphology for charge mobility and extraction [141]. They identify exciton dissociation efficiency enhancements of less than 2%, attributed to smaller aggregated domains [141]. More recently, Hu *et al*. and Wang *et al*. both produced ASM ternary blends composed of one donor and two acceptors resulting in enhanced performance through improved charge carrier behavior, and morphology regulation leading to reduced domain size [145], [154]. However, these few studies do not consider the effects of H-aggregates on energy transfer and device performance, instead focusing solely on domain size. We therefore tackle here the question of how H-aggregate population and domain size together influence energy transfer and device performance in ASM devices. We claim that phase separation which happens over time at device operating temperatures will lead to shifting intermolecular interactions and changing excited state energies. We ultimately make the case that commercial success in organic photovoltaic must account for how well active layer materials mix and the final morphology at thermal equilibrium.

## 4.2 Ternary Blends for Morphology and Population Control

Absorption spectra for each of $DBSQ(OH)_2$ and $DHSQ(OH)_2$, are shown respectively in Figure 4.1a and Figure 4.1b, i) in chloroform solution (indicating the typical monomer absorbance spectrum of these Squaraines), ii) as spin cast films, and iii) in binary thin film mixtures with PCBM. The broadening for all film spectra relative to solution spectra is typical of these materials as shown in our previous work [84]. The absorbance spectrum of the neat $DHSQ(OH)_2$ film in Figure 4.1b shows two broad peaks at 559 nm and 660 nm while that of $DBSQ(OH)_2$ in Figure 4.1a is a single broadened peak at 657 nm with a high energy shoulder. The clearly apparent double hump spectral motif of $DHSQ(OH)_2$ neat films in Figure 4.1b has previously been attributed to HCT formation and is a consequence of tightly packed face-to-face oriented molecules in the crystal structure [90], [106]. On the other hand, the single broadened peak and high energy shoulder of $DBSQ(OH)_2$ indicates the presence of DHAs with a large variation in packing densities and without sufficient density for Intermolecular Charge Transfer state coupling [84]. After annealing,

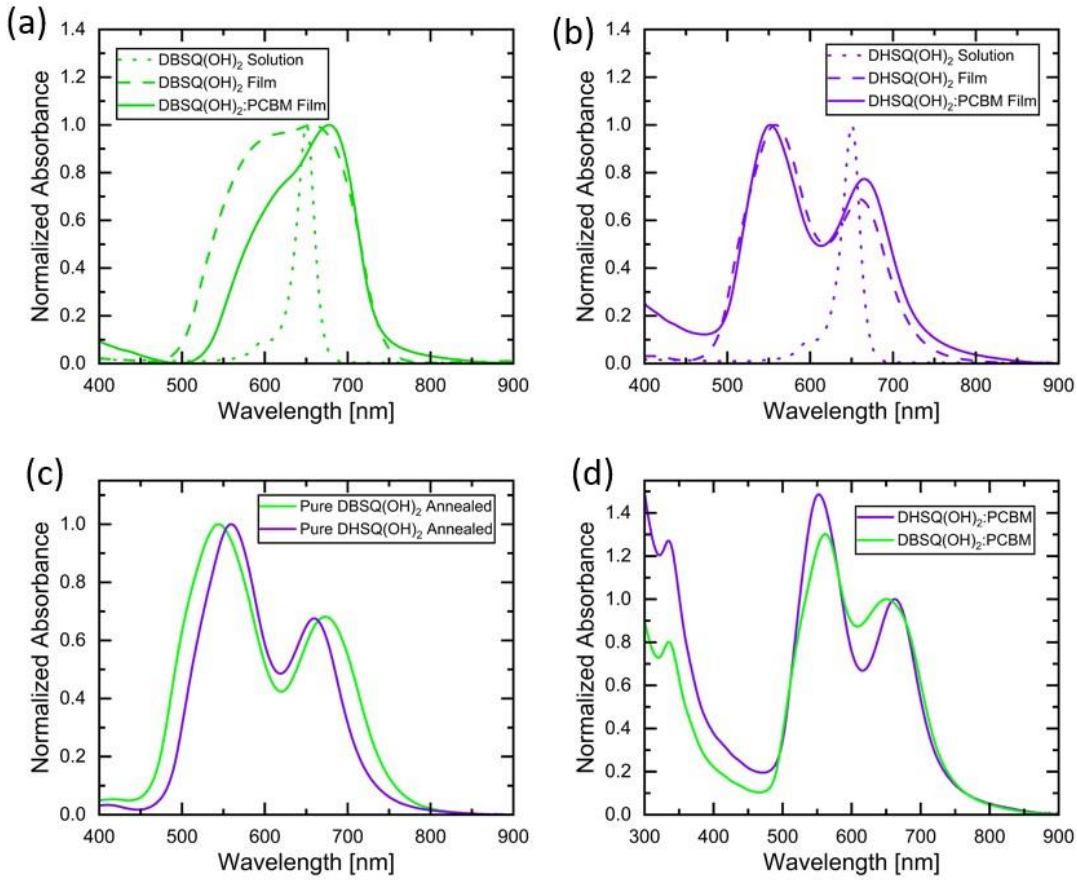


**Figure 4.1 - Normalized absorbance spectra of a)$DBSQ(OH)_2$ and b)$DHSQ(OH)_2$ in solution, a neat thin film, and a 1:1 blend film with PCBM. c) and d) compare the normalized annealed absorption spectra of $DBSQ(OH)_2$ and $DHSQ(OH)_2$ in a c) neat film and d) a 1:1 blend with PCBM. Unnormalized film absorption spectra may be found in the appendix in Figure A8.10.**

the spectra of both neat films in Figure 4.1c demonstrate double hump motifs corresponding to HCTs, induced by reorientation, and increased molecular density.

For PCBM film blends, absorbance spectra for both $DBSQ(OH)_2$ and $DHSQ(OH)_2$ show slight changes to peak position and intensity compared to those of their neat films (Figure 4.1a and b). Specifically, the low energy peak of the $DBSQ(OH)_2$:PCBM blend is red shifted to 676 nm and the high energy shoulder has lower intensity. This suggests $DBSQ(OH)_2$ tends to blend well with PCBM; the narrower peak and reduced high energy shoulder intensity indicate greater Squaraine separation consistent with homogeneous mixing in the PCBM, with therefore less DHA and more isolated monomer species [68]. In contrast, the $DHSQ(OH)_2$:PCBM blended thin film shows peak

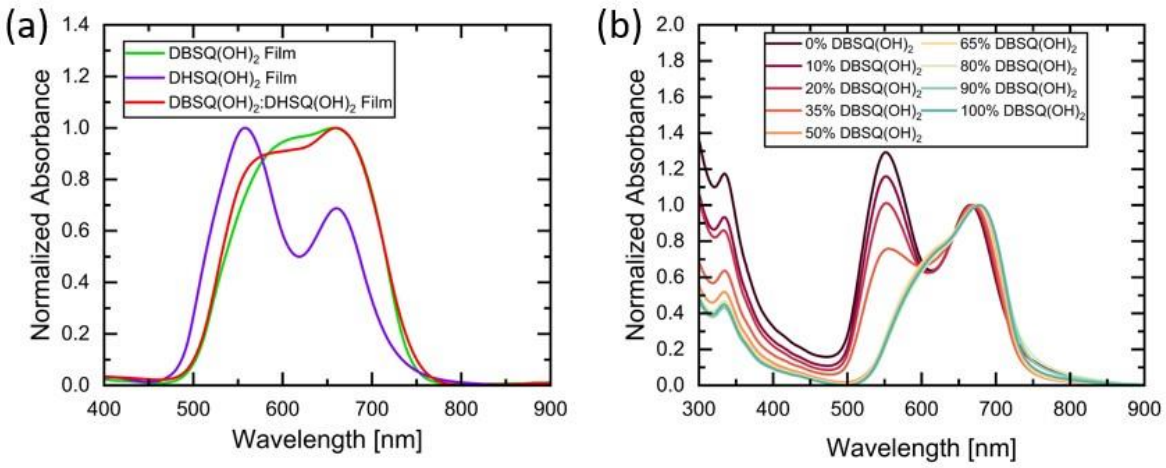


**Figure 4.2 - a) Normalized absorbance spectra of a binary blend of both Squaraine donors compared to individual neat films of each Squaraine molecule. b) Normalized absorbance of unannealed ternary blend films with changing DBSQ(OH)$_2$: DHSQ(OH)$_2$ weight ratio in the donor component while the donor:acceptor ratio is constant at 1:1. Unnormalized film absorption spectra may be found in the appendix in Figure A8.11.**

separation, with peaks now located at 556 nm and 664 nm. This is an indication of increased HCT population and increased domain size due to phase separation and poor mixing with PCBM [84], [106]. These inferences are further supported by contact angle studies for water deposited onto neat thin films. The PCBM contact angle of 81.23±0.60˚ is much closer to that of DBSQ(OH)$_2$ (87.57±1.26˚) than to that of DHSQ(OH)$_2$ (92.83±1.06˚). This confirms that the surface energy of DBSQ(OH)2 compares relatively well to PCBM and is consistent with better mixing for this pair than for DHSQ(OH)2 and PCBM pairing. Nevertheless, with annealing in Figure 4.1d, the double hump motif in the DBSQ(OH)$_2$:PCBM film spectrum demonstrates how phase separation of DBSQ(OH)2 films can be induced thermally. This thermally induced phase separation produces a transition in species from monomer and DHA to HCT, until finally HCT dominates as indicated by the double hump. In contrast, since there is minimal change to the DHSQ(OH)2:PCBM upon annealing, it is clear that the phase separation, increased packing density and HCT formation is initiated for DHSQ(OH)$_2$ during spin-casting [106]. We now consider the ability of these Squaraines to mix with one-another, allowing DBSQ(OH)$_2$ to break up the packing of DHSQ(OH)$_2$,

limiting HCT formation, and to act as a surfactant between $DHSQ(OH)_2$ and PCBM to improve blending.

In Figure 4.2a, a 1:1 binary blend of the two Squaraines is shown to have similar absorbance to that of the pure $DBSQ(OH)_2$ film with an absence of the double hump motif that would otherwise indicate HCT formation. Thus, introduction of $DBSQ(OH)_2$ effectively prevents HCT formation in $DHSQ(OH)_2$. Absorption spectra of unannealed ternary blends with a constant Squaraine:PCBM ratio and varying ratio of $DBSQ(OH)_2$ to $DHSQ(OH)_2$ are provided in Figure 4.2b. As the fraction of $DBSQ(OH)_2$ is decreased from 100% to 65%, there is very little change save for a blue shift in the peak from 678 nm to 667 nm. We infer that extensive HCT formation is prevented for 100%-65% $DBSQ(OH)_2$ blends, but some additional DHA is formed as the blend approaches 65% $DBSQ(OH)_2$, based on that slight blue shift [146]. From 50% to 0% $DBSQ(OH)_2$, a separated high energy peak forms at approximately 556 nm. This second high energy peak grows in intensity as the $DBSQ(OH)_2$ fraction decreases from 50% to 0%, representing the formation of HCT, with its double hump signature. The significant HCT formation results from higher crystallinity and greater phase separation as the $DBSQ(OH)_2$ falls below 50% of the Squaraine component. We note, however, that even small amounts of $DBSQ(OH)_2$ (10% $DBSQ(OH)_2$) still reduce the intensity of the high energy peak and prevent some HCT formation. These data in Figure 3b demonstrate a continuum, with a mix of higher DHA concentrations (and lower HCT concentrations) at 65% $DBSQ(OH)_2$ to a mix with higher HCT concentrations (and lower DHA concentrations) at 0% $DBSQ(OH)_2$.

To gain insight into the phase separation within the active layers of our ternary blends, including domain size and purity, representative films were studied using KPFM. We define a domain here as a region demonstrating contrast in KPFM, representing a section of the film that is chemically different and heterogeneously separated from surrounding regions. KPFM images, 300 nm and 1-micron, are shown in Figure 4.3 for several ternary blend ratios. Within these images,

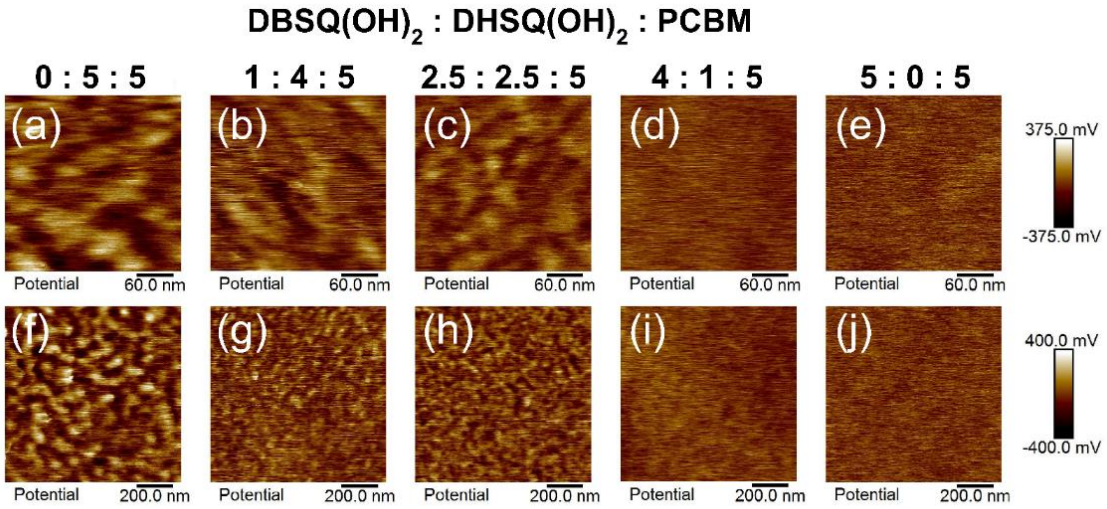


**Figure 4.3 - KPFM images ternary blends in (a)-(e) 300 nm and (f)-(j)1-micron sizes. Values provided at top of figure denote relative weight fractions of DBSQ(OH)2: DHSQ(OH)2: PCBM. Note that all figures in each row utilize the same provided potential scale on the right.**

separate dark and bright regions represent phase separation of Squaraine donors from the PCBM acceptor. Additionally, we attribute increased contrast between dark and bright regions to domain purification. A binary blend of $DHSQ(OH)_2$ and PCBM (0% $DBSQ(OH)_2$) is shown in Figure 4.3a and f. Significant phase separation is apparent with excellent contrast between large, pure regions of donor and acceptor. In the 80% $DHSQ(OH)_2$ blend (Figure 4.3b and g), domains are notably smaller with less contrast, but still remain largely intact. In the 50% $DHSQ(OH)_2$ blend, shown in Figure 4.3c and h, domain size and contrast is further reduced as $DHSQ(OH)_2$ is replaced by $DBSQ(OH)_2$. Finally, with significant decrease in the $DHSQ(OH)_2$ fraction of the donor component, to 20% (Figure 4.3d and i) and 0% (Figure 4.3e and j), excellent blending is observed, with little to no indication of separated domain formation.

In summary, KPFM data shows decreasing domain size and contrast as the relative weight percent of $DBSQ(OH)_2$ increases from 0% (Figure 4.3a) to 100% (Figure 4.3e) of the total Squaraine content. This illustrates markedly reduced phase separation and occurs alongside the spectroscopic assignments of Figure 4.2b, where increasing amounts of $DBSQ(OH)_2$ in a $DHSQ(OH)_2$:PCBM film show reduced double hump structure and reduced Intermolecular Charge

**Table 4.1 – Tabulated device performance parameters for ternary blend ratios. For all blends, the PCBM acceptor is 50% of the total mass, the remaining mass is split between the two Squaraine donors. Error values represent one standard deviation from the mean of all tested devices for the specified blend ratio.**

| *%DBSQ(OH)$_2$* | *$J_{sc}$ (mA/cm$^2$)* | *$V_{oc}$ (V)* | *FF (%)* | *PCE (%)* |
|---|---|---|---|---|
| ***100%*** | 7.16 ± 0.19 | 0.84 ± 0.01 | 47.79 ± 2.17% | 2.89 ±0.17% |
| ***90%*** | 7.22 ± 0.26 | 0.83 ± 0.03 | 47.64 ± 2.24% | 2.85 ±0.23% |
| ***80%*** | 6.76 ± 0.30 | 0.85 ± 0.01 | 50.84 ± 2.31% | 2.92 ±0.22% |
| ***65%*** | 6.33 ± 0.15 | 0.83 ± 0.02 | 45.39 ± 4.09% | 2.52 ±0.25% |
| ***50%*** | 5.81 ± 0.24 | 0.85 ± 0.02 | 46.64 ± 2.14% | 2.30 ±0.16% |
| ***35%*** | 5.64 ± 0.33 | 0.81 ± 0.02 | 44.43 ± 2.60% | 2.03 ±0.14% |
| ***20%*** | 5.68 ± 0.16 | 0.81 ± 0.02 | 44.19 ± 2.83% | 2.03 ±0.18% |
| ***10%*** | 6.40 ± 0.32 | 0.83 ± 0.02 | 44.74 ± 1.66% | 2.36 ±0.12% |
| ***0%*** | 6.29 ± 0.38 | 0.83 ± 0.02 | 46.16 ± 2.30% | 2.40 ±0.20% |

Transfer state coupling. DBSQ(OH)$_2$ therefore acts as a surfactant to not only break apart DHSQ(OH)$_2$ aggregation, but also encourage blending with the PCBM acceptor.

## 4.3 Device Efficiency Characteristics

Ternary blend device performance data are provided in Table 4.1 for a range of blend ratios with a fixed Squaraine:PCBM weight ratio of 1:1. In the range of all ternary blends in Table 4.1, we claim there to be no statistically significant trends or differences in either the open-circuit voltage ($V_{oc}$) or the fill factor (FF) across device blends. The consistent $V_{oc}$ is expected as it depends predominantly on the lowest unoccupied molecular orbital of the PCBM and the highest occupied molecular orbital of the Squaraine donors, neither of which are expected to change significantly [38]. We remind the reader at this point that device efficiencies are modest but that the primary scope of this work is to explore the effects of H-aggregation and active-layer mixing for comparable devices, made with 50% PCBM throughout, such that we could controllably modify a small number of experimental variables.

Short circuit current density ($J_{sc}$) and power conversion efficiency (PCE) are plotted in Figure 4.4 as a function of DBSQ(OH)$_2$ fraction of total Squaraine mass in the devices. We first note that binary DHSQ(OH)$_2$:PCBM devices had a consistently lower PCE (2.40%) than

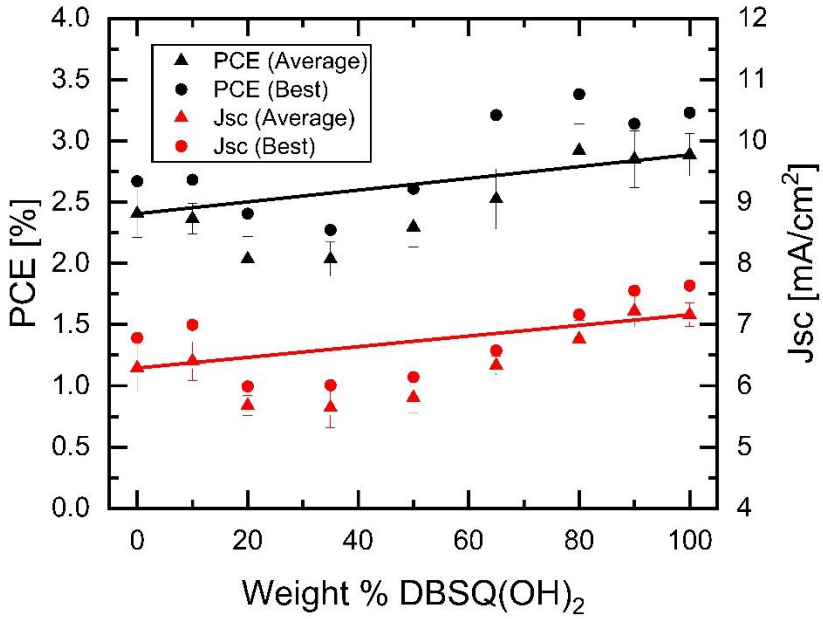


**Figure 4.4 - Plot of short-circuit current density and power conversion efficiency averages across all devices and the single best device. Solid lines represent weighted averages in the electrical properties between the two binary blends. Error bars represent one standard deviation from the mean of all tested devices for the specified blend ratio.**

DBSQ(OH)$_2$:PCBM devices (2.89%), agreeing with our previous work [84]. Below 20% and above 65% DBSQ(OH)$_2$ fractions, in Figure 4.4, the average $J_{sc}$ and PCE measurements align well with the "tie lines", which are simply straight lines connecting the efficiencies of the respective DHSQ(OH)$_2$:PCBM and DBSQ(OH)$_2$:PCBM binary devices. However, for DBSQ(OH)$_2$ fractions between 20% and 65%, the average and best-in-set $J_{sc}$ and PCE measurements all fall significantly below those tie lines, with average PCE falling as low as 2.03% for 20% and 35% DBSQ(OH)$_2$ devices. By considering Jsc and PCE measurements, we begin to explore the impacts on device performance of the i) phase separation/domain enlargement and ii) H-aggregate formation described above.

Significant phase separation (domain enlargement) has historically been associated with a loss of performance given that excitons would need to travel over longer diffusion lengths in order to enable the required electron transfer at the BHJ interface [110]. The device data of Table 4.1 shows high PCEs of 2.89%, 2.85%, and 2.92% for 100%, 90%, and 80% DBSQ(OH)$_2$ devices, respectively. We recall that these films show no significant phase separation in KPFM images

(Figure 4.3i and j). For the remaining blends, 0%-65% $DBSQ(OH)_2$, where phase separation was more observable in the KPFM images (Figure 4.3f-h), the average PCE never exceeds 2.52% and is as low as 2.03%. While a quantitative evaluation of the impact of phase separation is not provided here, these trends are certainly consistent with literature expectations; increasing phase separation and larger domains lead to lower device efficiency and provide some explanation for the typically lower performance of $DHSQ(OH)_2$ devices. However, phase separation alone fails to explain the further loss in performance of 20%-65% $DBSQ(OH)_2$ blends, identified by the dip below the tie lines of Figure 5. To illustrate, there is clear evidence of further phase separation moving from the 20% to the 0% $DBSQ(OH)_2$ blend, (Figure 4.3f and g). However, the 0% $DBSQ(OH)_2$ devices have an average PCE of 2.40%, much higher than the 2.03% average PCE of the 20% $DBSQ(OH)_2$ device, and significantly outside the error bars. Therefore, some characteristic other than phase separation must cause the dip below the tie lines of Figure 4.4.

The poor performance of the ternary blends in the 20% - 65% $DBSQ(OH)_2$ range is now investigated in the context of the mixture continuum between DHA and HCT apparent from the absorbance spectra shown in Figure 4.2. For 0% and 10% $DBSQ(OH)_2$ films, the pronounced double hump indicates a predominance of HCT. For fractions of $DBSQ(OH)_2$ increasing beyond 10%, the high energy peak of the double hump decreases in size, indicating gradual reduction in HCT until only DHA and monomer remain for films of 65% $DBSQ(OH)_2$ or more. It is during this same range of increase in $DBSQ(OH)_2$ weight percent (from 10% to 65%) that the identified dip below the PCE tie line occurs. A limitation in energy transfer across phase separated regions of HCT and DHA cannot be the main cause for efficiency loss since 0% and 10% $DBSQ(OH)_2$ devices retain higher efficiencies, and the phase separation and HCT populations are maximized in these devices. With this in mind, we further rationalize that previously discussed HCT and DHA species do not inherently restrict energy transfer as might be predicted from Förster energy transfer theory [40], [68], [88], [98]. Moreover, these data suggest that device efficiency may suffer as these HCT

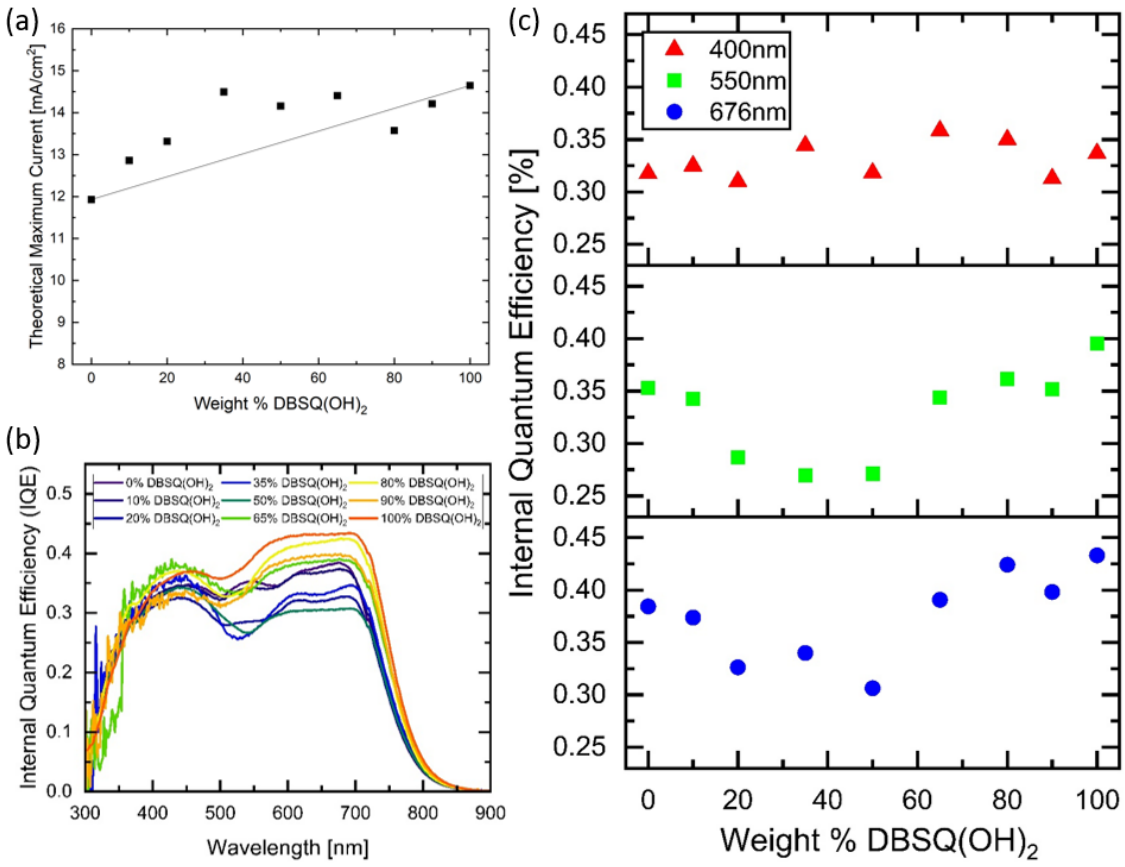


**Figure 4.5 – (a) Calculated maximum theoretical current density of unannealed ternary blend devices based on overlap integral of thin film absorbance and AM1.5 solar spectrum. (b) Internal Quantum efficiency spectra of ternary blends and c) Internal Quantum efficiency values at specified wavelengths from full spectra.**

and DHA species are more evenly distributed among a large diversity of other blended states. In other words, we hypothesize that the device efficiency drops because the distribution of states broadens to include a larger range of energies, with many different packing motifs.

To validate this conclusion, we must look to and invalidate alternative explanations. $J_{sc}$ is known to fluctuate with absorbance properties and the probability of carrier collection after exciton generation. The unnormalized absorbance spectra of the ternary blends provided in the appendix in Figure A8.11b indicates notable changes in the absorbance properties of these films. Changes to the absorption spectra will alter the overlap with available light in the solar spectrum and may provide an increase (or decrease) in the predicted number of absorbed photons. To explore this

possibility, we calculated the theoretical maximum current density for these devices based on the overlap of the absorbance spectrum of each film with the AM1.5 solar spectrum in

$$J_{SC,max} = -q \int \%Abs(\lambda)\phi_{\lambda}^{AM1.5} d\lambda \quad 4\text{-}1$$

where $q$ is the elementary charge constant, $\%Abs(\lambda)$ is the percentage of incident light predicted to be absorbed at a given wavelength based on the raw absorbance spectra [Figure A8.11b] and $\phi_{\lambda}^{AM1.5}$ is the AM1.5 solar spectrum in units of photons*$m^{-2}nm^{-1}$. We note here that this calculation is like calculating maximum $J_{sc}$ by external quantum efficiency, assuming that internal quantum efficiency is unity at all wavelengths. These theoretical maxima based on the measured absorption data are presented in Figure 4.5a. An increase in $J_{SC,max}$ is predicted between 0% and 65% $DBSQ(OH)_2$, above the simple weighted average tie line. Therefore, if all absorbed photons were collected, we would expect a significant $J_{SC}$ increase for the 20%-50% DBSQ(OH)2 devices whereas we observe a reduction. Therefore, the change in absorption spectra of these films is not the cause of device performance reduction.

To investigate further, internal quantum efficiency (IQE) spectra were measured for each donor blend ratio (Figure 4.5b) with IQE values reported at 400 nm, 550 nm, and 676 nm in Figure 4.5c. Given that only PCBM absorbs at 400 nm, the IQE for excitons generated only in PCBM can therefore be determined and is presented at the top of Figure 6b. The IQE at 400 nm varies randomly around an average IQE of 33%±2%. This provides a measure of the consistency across all our devices and strongly suggests PCBM behavior does not dramatically influence fluctuations in device performance.

The IQE data measured at 550 nm and 676 nm, the middle and bottom of Figure 4.5c respectively, correspond to each of the two double hump absorbance peaks for Squaraines in a ternary blend, with absorbance peaks occurring at 556 nm and 667-678 nm in Figure 4.2b. The IQE at 550 nm is found to average 36%±2% for devices with either less than 20% $DBSQ(OH)_2$ or more

than 65% DBSQ(OH)2. However, those devices with a $DBSQ(OH)_2$ percent between 20% and 65% have lower IQE values at 550 nm, averaging 28%±1%, well below the PCBM average. The data in Figure 4.5c show a similar trend with device IQE at 676 nm averaging 40%±2% with either below 20% $DBSQ(OH)_2$ or above 65% $DBSQ(OH)_2$; the remaining devices between 20% $DBSQ(OH)_2$ and 65% $DBSQ(OH)_2$ have much lower average IQEs of 32%±1%. The lower 550 nm/676 nm IQEs occur in the same 20%-65% $DBSQ(OH)_2$ devices for which there was a clear reduction in PCE and a steady change in population of HCT and DHA as evidenced by the absorbance spectra.

The higher IQE values, at both 550 nm and 676 nm, for devices of less than 20% $DBSQ(OH)_2$, where HCT dominates, are inconsistent with previous theories based on Förster energy transfer theories [40], [68], [88], [98]., which predict significantly lower energy transfer in HCTs and therefore lower quantum efficiencies. Furthermore, the IQE data at both 550 nm and 676 nm for devices with more than 65% $DBSQ(OH)_2$ are comparable with the efficiencies at <20% $DBSQ(OH)_2$. Therefore, we now frame the discussion again to consider that the PCE seems driven downwards by a broader range of DHA and HCT species combined, but not by a singular, narrow population of DHA nor by a narrow population of HCT. For devices where HCT and DHA coexist within the active layer, IQE is driven downwards by upwards of 8% for both the DHA and HCT species. We posit that this is a consequence of energy traps. Neighboring species, when excited, will naturally funnel their excited states into any lower energy levels in the surrounding species. Namely, excitations on the DHA species will fall into the lower energy levels of HCTs which are then unable to escape to the higher DHA energy levels. The result is the trapping of excitons and concomitant loss of efficiency in devices where these two species coexist.

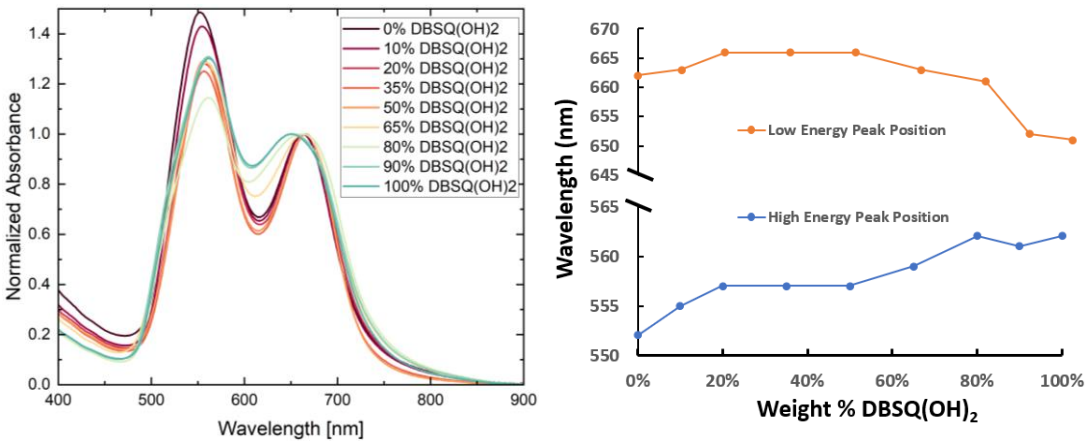


**Figure 4.6 – a) Normalized absorbance of annealed ternary blend films with changing $DBSQ(OH)_2$: $DHSQ(OH)_2$ weight ratio in the donor component while the donor:acceptor ratio is constant at 1:1. Annealing parameters were 5 minutes at 90˚C. Unnormalized film absorption spectra may be found in the appendix in Figure A8.12. b) Peak positions of the double hump spectral motif with increasing $DBSQ(OH)_2$ weight fraction.**

## 4.4 Focused Evaluation of Device Efficiency with HCT Formation

Increasing the fraction of $DHSQ(OH)_2$ in the total SQ contribution produced domain enlargement in Figure 4.3 and increased HCT formation based on the absorbance data of Figure 4.2b. We propose that by annealing the previous set of ternary blend devices at a lower temperature, we may limit further domain enlargement by preventing significant mass transfer but still provide sufficient energy for localized aggregation in already formed Squaraine domains of the kinetically stable morphology. Thus, through annealing at 90˚C for 5 minutes, we can focus on the energy transfer limitations of HCT formation, without domain enlargement which is known to limit energy transfer efficiency. By annealing at low temperatures, we move the morphology away from the kinetically stable state of each material ratio towards a more thermally stable state.

Absorbance data for the previously unannealed ternary blends (Figure 4.2b), now after annealing at 90˚C for 5 minutes, is provided in Figure 4.6a. All films demonstrate the double hump motif characteristic of HCTs with only subtle variation in peak position and broadness. As the $DBSQ(OH)_2$ fraction is increased from 0% to 50%, the entire spectrum has a 5nm red shift (high energy: 552→557nm, low energy 662→ 667nm) from the 0% sample to the 50% sample. At the same time, the height ratio of the high energy peak to low energy peak decreases. With further

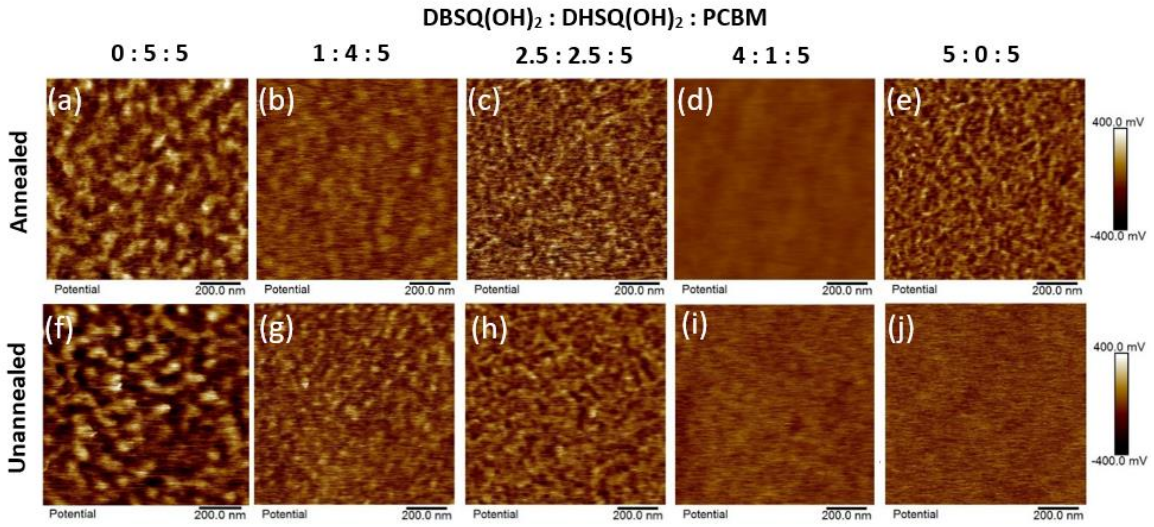


**Figure 4.7 - KPFM images ternary blends (a)-(e) annealed at 90˚C for 5 minutes and (f)-(j)unannealed. Values provided at top of figure denote relative weight fractions of DBSQ(OH)$_2$: DHSQ(OH)$_2$: PCBM. Note that all figures in each row utilize the same provided potential scale on the right.**

increase in the DBSQ(OH)$_2$ fraction from 50% to 100% of the SQ contribution, the peaks move closer together and the low energy peak shows significant broadening into shorter wavelengths. Lastly, as shown in the unnormalized annealed absorbance spectra of Figure A8.12, the increase in DBSQ(OH)$_2$ fraction produces an increase in the overall absorbance like what was observed when changing the DBSQ(OH)$_2$:DHSQ(OH)$_2$ ratio for the unannealed films (Figure A8.11b).

In addition to the positions of the individual peaks for each annealed ternary blend spectrum of Figure 4.6a, we may also consider the splitting for identifying HCT absorbance contribution. Recalling the absorbance of neat single squaraine annealed films, annealed DBSQ(OH)$_2$ was shown in Figure 4.1c to have a greater peak splitting (544nm and 675nm) than that of the annealed DHSQ(OH)$_2$ film in the same figure (560nm and 660nm). Yet an increase in DBSQ(OH)$_2$ fraction in our annealed ternary blends of Figure 4.6 produces narrower splitting between peak positions, Figure 4.6b. The reduced splitting (compared to films with no PCBM) as DBSQ(OH)$_2$ fraction is increased to 100% suggests a decrease in the average intermolecular separation of SQs in HCTs [90] along with less DBSQ(OH)$_2$ HCT formation in a blended film in comparison to a neat film. Furthermore, the red-shift and relative loss in height of the high energy peak when increasing the

**Table 4.2 – Tabulated device performance parameters for annealed ternary blend ratios. For all blends, the PCBM acceptor is 50% of the total mass, the remaining mass is split between the two Squaraine donors. Error values represent one standard deviation from the average of all tested devices for the specified blend ratio. PCE averages for annealed blends that are greater than one standard deviation above the average PCE of the unannealed are bolded in green. PCE averages for annealed blends that are less than one standard deviation below the PCE of the unannealed are bolded in red.**

| *%DBSQ(OH)$_2$* | *Jsc (mA/cm$^2$)* | *Voc (V)* | *FF (%)* | *PCE (%)* |
|---|---|---|---|---|
| ***100%*** | 8.56 ± 0.48 | 0.73 ± 0.04 | 45.00 ± 5.13% | 2.84 ±0.43% |
| ***90%*** | 8.51 ± 0.38 | 0.76 ± 0.02 | 51.50 ± 2.57% | **3.35 ±0.28%** |
| ***80%*** | 7.09 ± 0.23 | 0.79 ± 0.02 | 54.84 ± 4.73% | 3.08 ±0.36% |
| ***65%*** | 5.79 ± 0.14 | 0.77 ± 0.02 | 49.75 ± 2.44% | **2.21 ±0.11%** |
| ***50%*** | 6.40 ± 0.41 | 0.75 ± 0.08 | 50.52 ± 5.51% | **2.46 ±0.47%** |
| ***35%*** | 7.19 ± 0.32 | 0.79 ± 0.02 | 50.60 ± 1.85% | **2.86 ±0.21%** |
| ***20%*** | 6.47 ± 0.40 | 0.78 ± 0.02 | 49.27 ± 3.31% | **2.51 ±0.32%** |
| ***10%*** | 6.48 ± 0.40 | 0.79 ± 0.02 | 50.26 ± 2.22% | **2.59 ±0.21%** |
| ***0%*** | 5.66 ± 0.63 | 0.80 ± 0.03 | 47.61 ± 4.84% | 2.28 ±0.35% |

DBSQ(OH)$_2$ fraction indicates a reduced HCT contribution to the overall absorption. This is consistent with a simultaneous spectral broadening of the low energy peak (towards lower wavelengths), which suggests an increase in the presence of DHA. So, while all of the annealed films of Figure 4.6 show double hump character of HCT formation, it is clear that the incorporation of DBSQ(OH)2 leads to less HCT contribution and increased DHA formation. In summary, for annealed films, adding DBSQ(OH)$_2$ to DHSQ(OH)$_2$ increases the relative amount of DHA relative to HCT and this effect is more pronounced in the presence of PCBM.

KPFM images of ternary blended films with a gradual change in the percentage of DBSQ(OH)2 in the (50%) squaraine portion, before and after annealing, are presented in Figure 4.7. We note here that KPFM images of the unannealed films of Figure 4.7 are the same as those shown in Figure 4.3. For all ratios, except the binary blend of DBSQ(OH)$_2$:PCBM (Figure 4.7e and j), there is no clear increase in the domain size with low temperature annealing (90˚C for 5 minutes, Figure 4.7a-d and f-i). However, the annealed binary blend of DBSQ(OH)$_2$:PCBM (Figure 4.7e) shows some domain enlargement in comparison to its unannealed state (Figure 4.7j), although it is still less than what is observed in the unannealed DHSQ(OH)$_2$:PCBM film (Figure 4.7f).

Annealed ternary blend device data is provided in Table 4.2. In the table, PCE averages for annealed blends that are at least one standard deviation greater than the average PCE of the unannealed blend (Table 4.1) are bolded in green, while those which are less than one standard deviation lower than average PCE of the unannealed blend are bolded in red. Five of the nine ternary blend ratios studied here had a statistically significant PCE increase after annealing at 90˚C for 5 minutes, only one of the nine (65%$DBSQ(OH)_2$) had a statistically significant loss in efficiency, and the remaining three had no statistically significant change.

In the absorbance data for annealed films in Figure 4.6a there is clear evidence of HCT formation in all films based on the double hump spectral shape. In comparison, for the unannealed films in Figure 4.2b, only films with a DBSQ(OH)2 fraction of 35% or less had a double hump spectral motif and, furthermore, only the 10% and 0% DBSQ(OH)2 fractions had substantial HCT contribution based on the height ratio between the two humps. Simultaneously, the KPFM images of Figure 4.7 show limited increases in phase separation from annealing. Yet, the efficiency of all but one blend ratio either improved or showed minimal change, even with this significant HCT presence. If the HCT species was inherently a source of poor performance through poor energy transfer characteristics, we would expect devices to decrease in performance after low temperature annealing. Instead, the increase in PCE suggests that HCTs are not inherently bad for the performance of SQ based devices.

Furthermore, the combination of two SQs in a ternary blend is shown to preserve the morphology of the as-cast film through low temperature, 90˚C annealing; significant phase separation is prevented. Only the annealed binary blend of $DBSQ(OH)_2$ and PCBM in Figure 4.7e had significant phase separation after annealing with all other films showing no notable change in domain size after annealing. With additional annealing time, or higher temperatures, further phase separation may occur but the mixing of two anilinic squaraines seems promising in that it improves

the thermal stability of the active layer for organic photovoltaics without the need for costly additives or additional processing.

## 4.5 Discussion

The significant loss in device performance due to the co-existence of excited state species identified in unannealed devices raises concern about how the efficiency may decline over the lifetime of operation of organic photovoltaic devices. $DBSQ(OH)_2$:PCBM blends have been shown here to be one of the highest performing devices in Table 4.1 with an average PCE of around 2.90%. From the absorbance data, we infer that it is composed almost entirely of the monomer and DHA species, based on the single hump and high energy shoulder, in Figure 4.2a. However, upon annealing at 90ºC for 5 minutes, the absorbance shifts to the double hump motif of pure HCTs within the thin film, shown in Figure 4.2c. While field operation temperatures may not be so high over a device's lifetime, lower thermal energy of operation will still induce similar morphology changes, leading to a transition from DHA to HCT species over a longer time scale than just 5 minutes. It has been identified here how the co-existence of these two species is detrimental to device performance, producing a notable dip below the predicted tie-line in Figure 4.4, with over a 15% loss from predicted efficiencies. Yet, when HCT is the dominant SQ species within the active layer, and when problematic domain enlargement is limited, we tend to see an increase in device efficiency based on Table 4.2

In our system of Squaraines, the incompatibility between DHAs and HCTs is identified as problematic, and the negative impact is particularly accentuated because of the presence of both DHAs and HCTs. Many target materials for organic photovoltaic devices do not have such interesting, aggregated states that are so dependent on intermolecular separation and orientation. However, any two species with misaligned energy levels can be predicted to produce similar results due to the formation of energy traps. This concern can therefore be extended to other devices

composed of molecules which may aggregate, or rearrange, to form new species with different energy levels as the device is naturally annealed in the field.

Any loss in efficiency in a commercialized device caused by a slow transition between two species, leading to their temporary co-existence with different aggregation extents, would be a major concern; not only would it increase the payback period for the embodied energy costs of the device, but this might prevent commercial viability in the marketplace. Of course, accelerated lifetime tests are used to demonstrate compliance against industry standards during product development, but temperature cycling thermal tests can both over- or under-represent the true changes in efficiency for actual long-term performance [12]. In such high temperature and short duration tests, morphology changes occur over a short time scale and efficiency is only tested at a cycle's beginning and end [155]. However, we would predict that the mid-cycle morphology changes and associated efficiency effects representative of operation in normal conditions over long times would go unnoticed; subtle morphology changes that cause broad populations of differing energy states would not be accessed through the higher temperature accelerated lifetime testing.

Regarding devices in the field, whose long-term performance the solar cell industry attempts to predict through accelerated lifetime tests, the degradation of device efficiency over time has generally been observed to occur in stages. Following fabrication, organic photovoltaic devices tend to undergo a rapid loss of efficiency, referred to as burn-in. Efficiency then continues to degrade, but on a much slower time scale with a more linear decay rate. This more linear stage is most commonly indicated by measuring the Ts80 lifetime, the time the device lasts before 20% of its post burn-in efficiency is lost [12]. Studying solely the Ts80 lifetime hides the burn-in losses from the initially fabricated device, which are also likely associated with morphology change. Interestingly, burn-in losses have also been identified in devices while not in use [155]–[157] with Li *et al*. identifying efficiency losses of up to 40% after only 5 days of dark storage due to room temperature spontaneous phase separation [156], from the initial kinetically stable state to a

thermally stable morphology [158]. In addition, PCBM, the decades-old mainstay for commercial devices, has also been shown to significantly demix at moderate temperatures with a tendency to form large aggregates [159], [160]. Above all, such phase separation may occur at short and long time scales, at low and moderate temperatures, and over normal operating conditions. Shifting morphology leads to larger ranges of intermolecular distance and aggregation, and larger distributions of energy in the associated excited states. The key takeaway therefore is that, for all BHJ devices, an alignment of the optimal operating morphology and the thermally stable morphology is essential for commercial viability [158].

We think it valid to acknowledge here how many forms of morphology control have been proposed, and we ask whether they may lead to success by circumventing a need for optimal morphology to align with thermally stable morphology. The drive has always been to build the most efficient solar cell with a perfect trade-off between energy transfer and charge transport. Besides morphology control techniques such as thermal annealing and solvent annealing,

Finally, as we use a second Squaraine to illustrate and reinforce how an optimal morphology is needed in a thermally stable device, we also point to other work where the addition of a third active layer material has achieved such a stable morphology [148], [149], while also acting like a solvent additive for optimizing morphology. For example, Zhang *et al*. identified how the combination of two miscible donors, a small molecule and polymer, formed an alloy leading to ordering in the donor domains, with higher hole mobility, and overall better device efficiency [152]. Similarly, Liang *et al*. used a polymeric donor as an additive at 4 wt% to further enhance an already high efficiency ASM device; a key explanation was reduced domain size with improved phase continuity [153]. We therefore support how ternary blends may be a superior tool for maintaining higher efficiency after device burn-in, without any need for removal of orthogonal and potentially toxic solvent additives.

To review, when accelerated device testing is completed for industry compliance, it does not serve the need for improved understanding of failure mechanisms. Yet, we describe here how phase separation over time at the operating temperature is synonymous with dynamic molecular reorientation. Therefore, a continuous shifting of intermolecular interactions and associated excited state energies lead to changing device efficiencies in the field. We therefore make the case that commercial success must account for how well active layer materials mix, and for the final morphology at thermal equilibrium. We propose a need for careful selection and evaluation of organic photovoltaic molecules over their entire lifetime, not just the initial or final efficiency of devices with respect to accelerated testing. A narrow range of state energies for selected molecules, even as the packing changes and the molecular environment changes, is necessary to ensure limited diversity throughout operational lifetime. Without careful consideration of the intermediate stages of a device's operation, substantial temporary losses in efficiency may go unseen as one species gives way to another.

## 4.6 Conclusions

In summary, to discern the impact of Squaraine DHAs and HCTs on organic photovoltaic performance, two Squaraine donors, with different blending properties with a PCBM acceptor, were combined in a 2-donor, 1-acceptor ternary blend. $DBSQ(OH)_2$ was found to behave almost like a surfactant for $DHSQ(OH)_2$ and PCBM, by breaking apart pure $DHSQ(OH)_2$ domains, limiting H-aggregate formation, and enhancing $DHSQ(OH)_2$ blending with PCBM. The enhanced control over Squaraine aggregation in devices allowed us to reveal that the previously concerning DHA and HCT species are not inherently bad for devices individually. Rather, it is the co-existence of these two species which hurts performance, producing 15% lower PCEs in devices where both species exist simultaneously, as compared to devices where either species exists alone. The efficiency loss is proposed to be a consequence of increased energy trap density, a consequence of the different energy levels when both DHA and HCT co-exist within the active layer, leading to an 8% loss in internal quantum efficiency for both. This outcome is concerning with organic

photovoltaic commercialization approaching. Low temperature annealing during long-term field operation for any organic photovoltaic is likely to induce different levels of aggregation, as was observed here through decreasing fractions of $DBSQ(OH)_2$ in the ternary blends. Should such aggregation lead to the formation of a new species with incompatible energy level alignment, as here it led to combined DHA and HCT formation, the resulting loss of efficiency from their co-existence would be unfavorable. Thus, we posit a growing need for consideration of efficiency throughout device lifetime, rather than solely at the beginning or end. A highly efficient device is of little value if morphology and aggregation produce unfavorable diversity in the middle of device lifetime, leading to efficiency losses that may go unnoticed in accelerated testing.

Strategies for success may include incorporating material blends for which there are only a narrow range of state energies even as the packing changes or the molecular environment changes. If the goal is to obtain the highest possible device efficiency in the lab, then a kinetically stable mixture of donor and acceptor formed after spin-casting may lead to valuable and informative record-breaking efficiencies. For the goal of commercialization however, extensive annealing in laboratory devices of course moves the device to an equilibrium geometry that will result from many hours of use at elevated temperatures in the field. Consideration of stability of the morphology over the lifetime of the device and limited additional need for processing or additives is essential for elongating device operational lifetimes without substantial added cost. Beyond initial lab work for all small molecule devices, consideration of intrinsic miscibility in subsequent design phases is valuable; for example, side groups may be added to a promising active layer acceptor candidate such that it mixes appropriately with the target donor candidate, and vice versa, and maintains such mixing under greater thermal stress.

# 5 Chapter 5. Energy Transfer Mechanisms of Squaraine Charge Transfer H-aggregates

The previous chapters have shown that the formation of HCTs in organic photovoltaics (OPVs) is not inherently detrimental to overall device efficiency. Instead, the efficiency loss appears to be primarily due to larger domain sizes and a diverse excited state population, which can lead to trap formation. Furthermore, highly efficient OPVs typically have smaller domain sizes, even when HCTs are the predominant species within the active layer. However, our current understanding is limited to overall OPV efficiency measurements, which include confounding variables such as charge diffusion rates. These rates are expected to improve with the same crystallization process that leads to HCT formation. As a result, we aim to specifically evaluate the energy transfer properties of HCTs separately from other steps in the OPV mechanism. To analyze HCT energy transfer properties, we will use transient absorption measurements to monitor the excited state kinetics of Squaraine HCTs in thin films. We will assess HCT energy transfer rates in two different Squaraines, DHSQ(OH)2 and DBSQ(OH)2, under four conditions: i) unannealed neat film, ii) annealed neat film, iii) unannealed blended film with PCBM, and iv) annealed blend film with PCBM. Our findings indicate that energy transfer from HCT excited state populations to monomers occurs in less than 100 femtoseconds for both Squaraines. Moreover, in unannealed DBSQ(OH)2:PCBM blended films, initially populated HCT excited states reach the interface and achieve charge separation, forming a PCBM anion in less than 2 picoseconds. This is over ten times faster than timescales identified in other films. We propose that HCTs favor the Dexter energy transfer mechanism, which exhibits extremely fast energy transfer rates. These rates are only limited by the Dexter mechanism's preference for short-distance transitions, further emphasizing the importance of small domains for OPV efficiency.

## 5.1 Background Literature Review

In the literature, formation of HCTs in OPV active layers tends to correlate with a loss in device efficiency [53], [84]. However, formation of HCTs is often coupled with extensive phase separation

[53], [84], [120] from the PCBM acceptor during spin-casting [84] or from high temperature thermal annealing to produce a thermodynamically favored morphology of large domains [53]. Additionally, devices utilizing $DBSQ(OH)_2$ as the molecular donor consistently outperform devices using $DHSQ(OH)_2$ as the molecular donor when other processing parameters are consistent [84], [120]. However, $DHSQ(OH)_2$ preferentially forms notably larger domains than $DBSQ(OH)_2$ when blended with PCBM [120] and has absorption characteristics with poorer solar spectrum alignment (section 4.3), both of which are known contributors to a lower device performance.

In Section 4.4, we enhanced the excited state coupling and HCT formation without causing phase separation by employing low-temperature annealing. This process facilitated molecular reorientation without significant mass transport. As a result, the devices exhibited increased efficiency and greater HCT state formation compared to their pre-annealed states. It is worth noting that such molecular reorientation and crystallization are expected to improve charge diffusion efficiency, which may have contributed to the observed increase in overall device efficiency. Therefore, it is crucial to isolate the energy transfer efficiency of HCT species to determine their individual contribution to the device's overall efficiency.

To analyze the kinetics of excitons and polarons within OPV active layers, high-speed observations of excited states are required. Transient absorption (TA) spectroscopy serves as one of the most prominent tools for this purpose. Although the TA experimental setup used in this study was previously described in Section 2.2.4, we offer some supplementary information on the mechanism and signal interpretations for TA in this section.

In general, TA monitors subtle changes in the absorbance properties of a film or solution, in time frames on the order of pico- or femtoseconds, after a significant number of excitons are generated [68], [161]. TA initially hits the sample with many polarized photons at a selected wavelength to induce an excitation in a large fraction of the molecules in a sample, referred to as a “pump”. This pump results in a large population of excited states, reducing the number of molecules

in the ground state. At select delay times after the pump, a polarized probe beam measures the absorbance spectrum of the now excited sample. The difference in the absorbance of the probe beam, at a given delay time, and the steady state absorbance is the sample's transient absorption. The resulting spectra include both negative and positive signals that can be used to characterize the behavior of excited states. By adjusting the polarization orientation relationship of the probe and pump, we can determine a parallel and perpendicular response of the sample. Using both responses, the loss of anisotropy, may be measured by equations 2-3 and 2-4. What follows is a brief description of some of the signals in TA along with possible interpretations applicable to this work. The y-axis component for all the following TA data is the change in absorbance normalized to the original absorbance at a given wavelength, $\Delta A/A$. Therefore, a negative value means more transmission of the probe beam and a positive value means less transmission of the probe beam, with again some further detail to follow.

**Ground state bleach (GSB):** A negative signal is observed in transient absorption spectra when the ground state of the sample is depleted by the excitation pulse, thereby reducing its concentration and therefore, as described by the Beer-Lambert law, reducing the absorption of the sample. It is important here to emphasize that a ground state bleach does not guarantee the corresponding excited state is populated, only that the ground state capable of making the transition to that excited state has been depopulated.

**Stimulated emission (SE):** Stimulated emission from excited species leads to the amplification of the probe beam intensity and therefore it appears as if the transmission of the sample has increased at probe beam wavelengths pertaining to emission energies for that fluorescence.

**Excited state absorption (ESA):** Molecules in an excited state may be capable of experiencing a second photon event when the excited molecule can absorb another photon, inducing a second transition. The result is an increase in the absorption of the sample at that probe wavelength which pertains to the transition energy from excited state i to excited state j.

**Anions/Cations:** Charge separation between two components in a blend leads to the formation of radical anions and radical cations, also known as polarons in solid state physics [162]. The creation of these positively and negatively charged species alters the electronic structure of the molecules, subsequently leading to new absorption characteristics.

For a more detailed summary of various TA signals, the interested reader is directed to [163].

After the assignment of signals in a TA spectrum, kinetic studies are used to describe the dynamics of photoinduced processes in the sample. In a typical kinetic study, changes in the assigned signals (peak shifts, decay/growth rates) are monitored over the available range of time delays. By analyzing the temporal evolution of the transient absorption spectrum, kinetic parameters such as rate constants (or lifetimes) and mechanisms of photoinduced processes can be determined. A rate constant describes the dynamics of a photoinduced process in a material, or the speed at which a transition occurs. The lifetime typically refers to the reciprocal of the rate constant. Thus, a faster rate constant leads to a shorter lifetime and vice versa.

Power density studies enhance transient absorption spectroscopy as excitation laser intensity affects photoinduced process dynamics. High-power densities increase excited state populations, raising the rates of bimolecular processes such as exciton-exciton annihilation, which requires two excitons transferring energy to the same point, causing annihilation. Varying laser power density therefore varies exciton-exciton annihilation rates, which allow an assessment of the all-important energy transfer rate constant.

Lastly, transient anisotropy is important in the study of photoinduced processes because it provides information about the orientation and motion of molecules in a sample. By measuring the change in the relative absorbance of probe polarization parallel to the pump to absorbance perpendicular to the pump, a decay in anisotropy can be identified. Anisotropy decay can indicate a time-dependent motion of excitations. In a solid film, molecular reorientation is restricted, so

polarized excitations can only be measured by a probe beam perpendicular to the pump beam once the exciton has undergone energy transfer to a new molecule that is parallel to the probe orientation, or if there has been a relaxation to an excited state in the same molecule, dimer or aggregate with a transition dipole moment perpendicular to the transition dipole moment associated with the photoinduced transition. Thus, transient anisotropy measurements may be used to study the dynamics of energy transfer and charge separation in thin solid films. In general, the maximum anisotropy that can be obtained in a transient absorption measurement is 0.4, which corresponds to a completely aligned sample. A more complete description for the maximum anisotropy may be found in the appendix and interested readers will find more details in [164]. Significant reduction below the maximum value of 0.4 is therefore indicative of a more isotropic excited state population, implying significant energy transfer from the initially highly polarized population.

A significant amount of work has already bone done on the energy transfer properties of both Squaraine monomers and squaraine dimer H-aggregates. Somashekharappa *et al.* studied squaraine monomers in solution with PCBM and were able to observe evidence of successful charge separation through the formation of the Squaraine cation with a time constant of around 80 to 100ps [165]. Goh *et al.* identified energy transfer between two different squaraines in a thin film in time frames around 1ps through the FRET mechanism, achieved by selecting two squaraines with an excellent spectral overlap integral [166]. Zheng *et al.* previously interpreted TA measurements of $DBSQ(OH)_2$ molecules dispersed in a PMMA matrix [68]. Their findings revealed that excited monomers preferentially underwent energy transfer on pathways into progressively tighter packed dimer H-aggregates before exciton-exciton annihilation quenched the signal [68]. However, samples had a low SQ in PMMA concentration such that charge transfer coupling was stifled, preventing interpretation of HCT energy transfer properties. Similarly, de Miguel *et al.* evaluated six different squaraines in thin films where there was a coexistence of H- and J-aggregates [167]. They found a similar result where monomer excited states underwent rapid

**Table 5.1 – Quick reference table of the eight films studied using transient absorption spectroscopy to assess the energy transfer efficiency of charge transfer H-aggregates. Note that all films blended with PCBM are a 1:1 ratio of squaraine to PCBM. All annealed films were annealed at 90˚C for five minutes.**

| *Film* | *Shorthand Name* | *Absorbance Spectrum* | *Qualitative Description of Species* |
|---|---|---|---|
| *$DBSQ(OH)_2$ Neat Unannealed* | ButNeatUn | Figure 5.1a Dashed | DHA and M |
| *$DHSQ(OH)_2$ Neat Unannealed* | HexNeatUn | Figure 5.1b Dashed | Complete HCT |
| *$DBSQ(OH)_2$ Neat Annealed* | ButNeatAnn | Figure 5.1c Green | Complete HCT |
| *$DHSQ(OH)_2$ Neat Annealed* | HexNeatAnn | Figure 5.1c Purple | Complete HCT |
| *$DBSQ(OH)_2$:PCBM Unannealed* | ButPCUn | Figure 5.1a Solid | Mostly M, Some DHA |
| *$DHSQ(OH)_2$:PCBM Unannealed* | HexPCUn | Figure 5.1b Solid | Complete HCT |
| *$DBSQ(OH)_2$:PCBM Annealed* | ButPCAnn | Figure 5.1d Green | Complete HCT |
| *$DHSQ(OH)_2$:PCBM Annealed* | HexPCAnn | Figure 5.1 Purple | Complete HCT |

energy transfer to the aggregates in time frames on the order of picoseconds, followed by rapid loss of signal through exciton-exciton annihilation [167]. The apparent preferential motion of excitons from monomers to aggregates does not bode well for the performance of OPVs provided that the D:A interface is likely where monomer species are most common due to the intermixing of the two materials restricting significant aggregation. However, limited analysis has been done on the directional preferences of energy transfer in charge-transfer H-aggregates.

## 5.2 Transient Absorption Design of Experiment

In designing the transient absorption experiment, we aimed to identify the specific energy transfer contribution of HCTs to overall OPV efficiency. To achieve this, eight films were evaluated, summarized in Table 5.1, and discussed here for their key differences and value for the intended goal. All films were cast from solutions with a concentration of 4.5mg/ml, unless otherwise specified, to achieve a sufficiently low optical density for the TA instrument. Additionally, for these experiments we utilized two different pump excitation wavelengths (550nm and 645nm) and three different laser power densities for each measurement (selected from 10, 20,

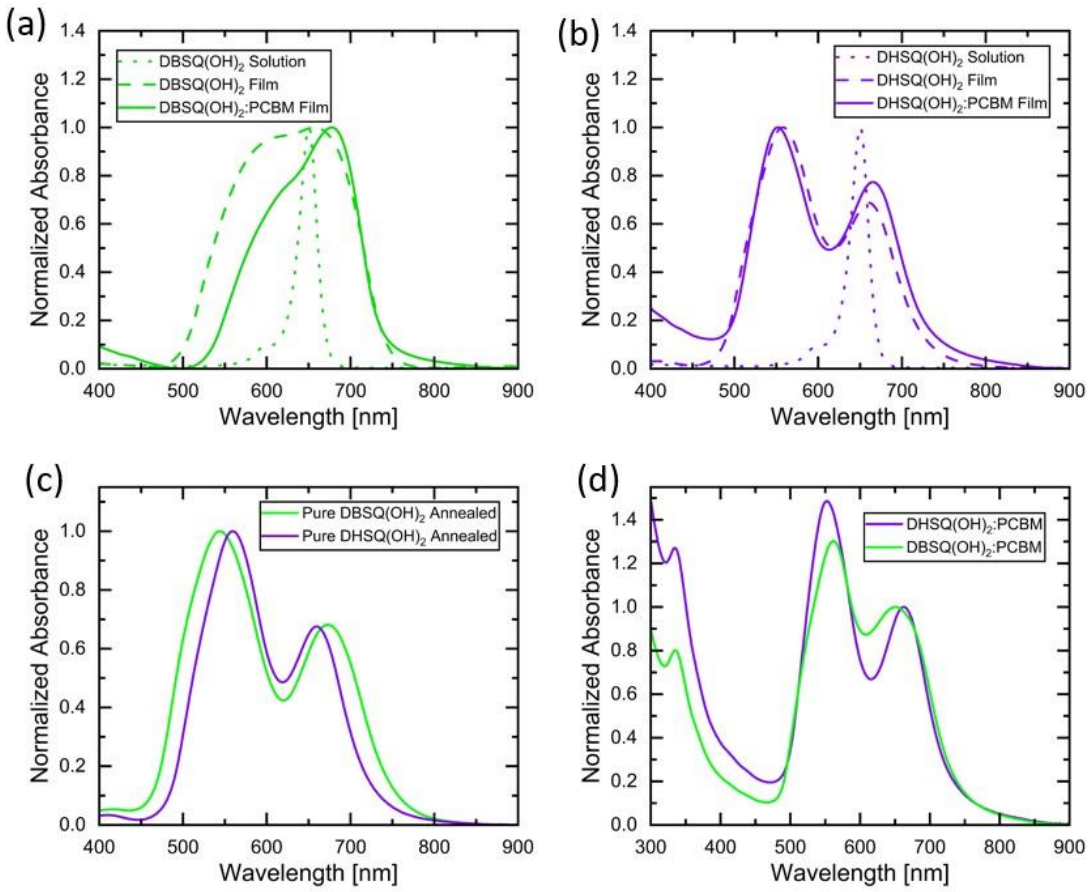


**Figure 5.1 (Repeat of Figure 4.1 for reference) – Normalized absorbance spectra of a)DBSQ(OH)$_2$ and b)DHSQ(OH)$_2$ in solution, a neat thin film, and a 1:1 blend film with PCBM. c) and d) compare the normalized annealed absorption spectra of DBSQ(OH)$_2$ and DHSQ(OH)$_2$ in a c) neat film and d) a 1:1 blend with PCBM.**

40, and 80 μW depending on response signal intensity). To be concise, in this section we will utilize the shorthand names given in Table 5.1 when referencing each film. All of the following qualitative assignments provided here and in Table 5.1 are made based on the corresponding absorbance spectra features in Figure 5.1 for each film.

All four of the neat films are utilized to monitor the kinetics of HCTs, DHAs, and Monomers in a neat thin film without the possibility for charge separation at an interface. ButNeatUn and HexNeatUn represent the as cast excited state population of each neat material where ButNeatUn is composed of a conglomeration of Monomers and DHAs while HexNeatUn is mostly composed of HCTs. Based on these descriptions, we expect smaller domains and a more

diverse energy landscape in the ButNeatUn film while the HexNeatUn film is predicted to have a less diverse energy landscape with larger individual domains. By annealing the films at 90˚C for five minutes, we identify complete HCT formation in both the ButNeatAnn and HexNeatAnn films and can more directly compare behavior of the HCT for both squaraines. From the neat films, we aim to identify if there is a preferential pathway for excitons to undergo energy transfer from monomers to tighter packed species such as DHAs or HCTs as seen in the literature [68], [167] or if the opposite direction is more preferred. By exciting at 550nm, we preferentially excite any HCTs and DHAs in the film given the complete lack of monomer absorbance at that wavelength. In contrast, by exciting at 645nm, we excite a conglomeration of monomers and low energy HCTs (through the HCT(-) state).

Upon blending the films with PCBM, we allow for charge separation to take place and aim to interpret whether the preferential directions of energy transfer identified in the neat films lead to efficient charge separation. To explain, we assume that HCTs will be most prominent near the center of squaraine domains as a consequence of the increased squaraine density and reduced mixing/increased purity [122]. In contrast, at the edge of domains, near the PCBM interface, there is likely some intermixing of the two materials such that PCBM may restrict significant aggregation leading to an increase in monomer population. The result is a sphere of densely packed HCTs surrounded by a "fuzzy shell" of monomers and DHAs. Consequently, this assumption implies that a preferential motion of excitons from HCTs to monomers would be greatly beneficial to devices. Additionally, we note here that the inclusion of PCBM should not lead to the formation of excitons on the PCBM from our chosen excitation wavelengths as the PCBM has negligible absorption at wavelengths above 500nm. As such, any observed photoinduced processes attributed to a PCBM species are necessarily indicative that charge transfer at the Squaraine:PCBM interface has occurred.

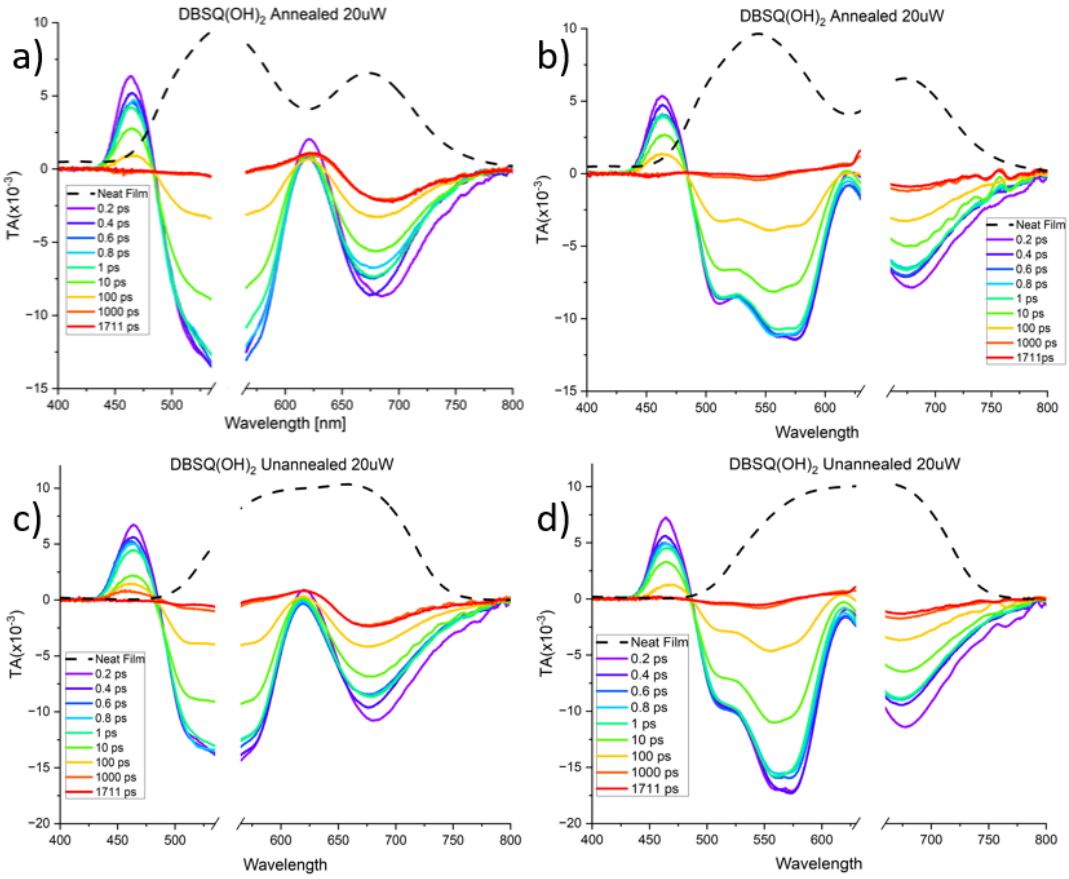


**Figure 5.2 – Transient absorption spectra of an annealed (a, b) and unannealed (c, d) $DBSQ(OH)_2$ neat film excited by a pump wavelength of 550 nm (a, c) and 645 nm (b, d).**

## 5.3 Transient Absorption of Neat Squaraine Films

The four sections below respectively describe the spectral features from the transient absorption experiment, assign the features and trends to phenomena and processes in the samples, explore the kinetics and then summarize the findings.

### 5.3.1 TA Spectral Features of Neat $DBSQ(OH)_2$ and $DHSQ(OH)_2$

Transient absorption spectra of $DBSQ(OH)_2$ neat films excited by pumps at 550nm and 645nm are provided in Figure 5.2. For all subfigures a through d, gaps in the spectral data result from the exclusion of the 30nm bandwidth around the excitation wavelength because pump photon scattering restricts data accuracy in this range. For this set of data, there are enough similarities in spectral behavior with changes in both the excitation wavelength and annealing that the following

signals and trends are present for all cases; differences will be called out specifically when they occur. Five clear signals are here identified for the TA spectra of Figure 5.2.

Ground State Bleach (550 nm, 675 nm)

Two clear negative signals *ca.* 550nm and 675nm, are present in all the TA spectra of $DBSQ(OH)_2$ neat films. Notably these signals align well with the steady state absorption of the $DBSQ(OH)_2$ annealed neat film, shown as a black dashed line in Figure 5.2a and b. This double hump spectral motif has been previously designated as the HCT species, we therefore assign these peaks to a GSB of the HCT species (HCT(-) at 675nm and HCT(+) at 550nm).

The HCT(-) GSB (675nm) blue shifts in the first 400fs and there is a notable loss of peak height in this signal between the 0.2 and 0.4 ps time slices in all cases except in Figure 5.2a (annealed, 550nm excitation). This feature decreases in height significantly over the first 1000ps but remains constant thereafter until the limits of the experiment at 1700ps. We also note that in Figure 5.2a, during the decay of the first 1000ps, the HCT(-) GSB shows a clear red-shift in peak position.

In contrast to the HCT(-) GSB, the HCT(+) GSB changes minimally in the first 800fs before decaying rapidly thereafter such that HCT(+) GSB is completely gone by 1000ps.

Excited State Absorption (465 nm, 620 nm, 525 nm)

In all spectra there is a clear positive signal at approximately 465nm which appears immediately after excitation and which decays completely by approximately 1000ps with no further change at later times. Another positive signal at 620nm, clearest in Figure 5.2a, appears in all cases, significantly raising the peak in this range beyond what is expected based on the steady state spectrum. The 620nm signal shows an early blue shift and peak height reduction in the first 400fs. Then the peak height of this signal increases in remaining time in all cases, except in Figure 5.2a, where the peak height remains unchanged for the rest of the experiment. Lastly, there is a positive

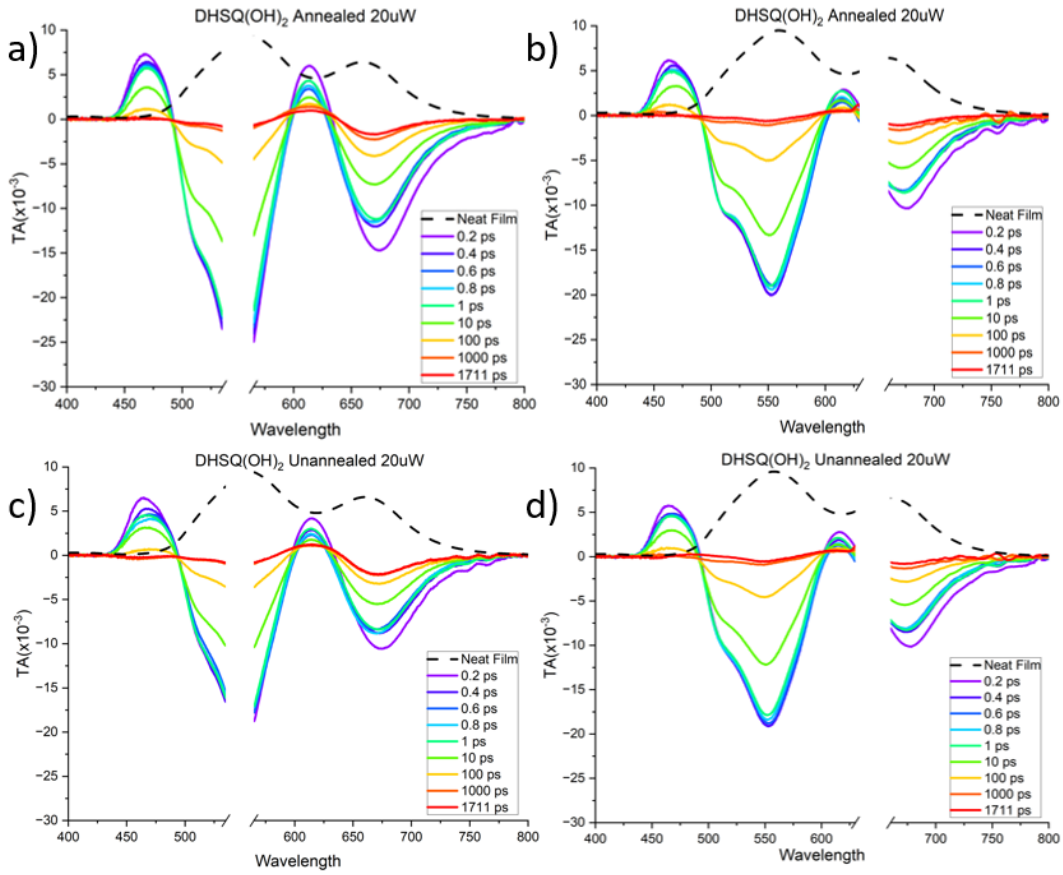


**Figure 5.3 – Transient absorption spectra of an annealed (a, b) and unannealed (c, d) $DHSQ(OH)_2$ neat film excited by a pump wavelength of 550 nm (a, c) and 645 nm (b, d).**

signal contribution at around 525nm in films excited at 645nm (Figure 5.2b and d) that can be identified by analyzing the disruption in the gaussian shape of the HCT(+) GSB. This feature is gone by 1000ps in all films.

For the $DHSQ(OH)_2$ neat films shown now in Figure 5.3, there are again significant similarities in spectral features and trends with the $DBSQ(OH)_2$ neat films discussed previously. The same five clear signals are identifiable in the TA spectra of Figure 5.3 with only subtle differences in position and height.

Ground State Bleach (550 nm, 675 nm)

Present in all films are the two clear negative signals *ca.* 550nm and 675nm, previously assigned to a GSB of the steady state absorption of the HCT species. The behavior of both negative

signals is comparable to their behavior in the $DBSQ(OH)_2$ films, though it is noted here that the long-lived characteristic of the HCT(-) GSB is blue-shifted from its starting position, rather than red-shifted or unchanged as in the $DBSQ(OH)_2$ films.

Excited State Absorption (465 nm, 620 nm, 525 nm)

There remains a clear positive signal at approximately 465nm, appearing immediately after excitation and fully decaying by approximately 1000ps. The positive signal at around 620nm appears again and is present until the conclusion of the experiment at 1711ps. However, there is a clear increase in height of this signal in all spectra of $DHSQ(OH)_2$ compared to the spectra of $DBSQ(OH)_2$ spectra; for example all features at 620 nm sit above the baseline and are positive in magnitude whereas the same feature in Figure 5.2 may often sit below the baseline and may only be inferred by direct reference to the steady state spectrum. Lastly, the positive signal at around 525nm is present in all $DHSQ(OH)_2$ experiments of Figure 5.3. The now consistent appearance of the positive feature at 525nm in the $DHSQ(OH)_2$ measurements of all subfigures of Figure 5.3 is notably different from the $DBSQ(OH)_2$ experiments where a positive feature at 525nm is only visible in films excited at 645nm (Figure 5.2b and d). The kinetics of the 525nm feature remain similar however for all appearances, with the signal having completely decayed by 1000ps.

### 5.3.2 Assignment of the TA Spectral Features of Neat Squaraine Films

All features identified for the neat films of both Squaraines (annealed and unannealed) have been summarized in Table 5.2 for reference.

Both the 550nm and the 675 nm TA features align with the steady state absorbance features of the HCT(+) species and the 675 nm absorbance features, respectively. Therefore, these features are assigned to ground state bleaching of the HCT(+) and HCT(-) species respectively. There are some small observable shifts in the position of the HCT(+) GSB at select time slices, but none are

**Table 5.2 – Summary table of all the features identified in the neat film TA spectra of Figure 5.2 and Figure 5.3 and key decay behaviors.**

| *Wavelength (nm)* | *+/- Signal* | *Decay Comments* |
|---|---|---|
| *465* | + | Signal appears immediately after excitation at both 550nm and 645nm, decays completely by approximately 1000ps. |
| *525* | + | Positive signal contribution present in all $DHSQ(OH)_2$ films and $DBSQ(OH)_2$ films excited at 645nm, gone by 1000ps in all films. |
| *550* | - | Signal appears immediately after excitation at both 550nm and 645nm, decays completely by approximately 1000ps. |
| *620* | + | Signal appears immediately after excitation, notable blue shift and peak height reduction in the first 400fs.<br>After 400fs in $DHSQ(OH)_2$, signal slowly decays during remainder of experiment but never completely disappears.<br>After 400fs in $DBSQ(OH)_2$, signal grows slightly and never disappears. |
| *675* | - | Signal appears immediately after excitation, notable blue shift and peak height reduction in the first 400fs in all cases.<br>Feature decreases in height significantly over the first 1000ps but remains constant thereafter until the limits of the experiment at 1700ps. |

large enough to refute this assignment. These small shifts are indicative of subtle changes in the average molecular packing around excited states leading to changes in the double hump splitting motif [90], [106]. There is also some complexity to explore below in that the HCT(-) GSB remains present after the HCT(+) GSB has completely recovered, for all cases. There is no obvious contribution from any GSBs other than the HCT following excitation. Therefore, HCT is inferred to be the *dominant* absorbing species by the pump, regardless of wavelength.

Since the double hump spectral motif has been previously assigned to HCTs [90], we expect that the height of each GSB feature would track the other. Yet, there remains a long-lived GSB at 675nm, after the 550nm GSB has recovered. There are two possible explanations: 1) An excited state for a different species that absorbs at ~675nm has been populated via energy transfer from the HCT or 2) HCT(+/-) states may be uncorrelated. Given that HCT(+) and HCT(-), are a result of coupling between CT and DHA excited states,[90] uncorrelated HCT(+/-) states is highly unlikely and we reject explanation 2. Thus, we conclude that energy transfer must be occurring from initially excited HCTs into a different species absorbing only at ~675nm.

The long-lasting component of the signal at *ca.* 675nm, still present after complete decay of the 550nm signal in all films, we propose to be a monomer GSB. The position of this long-lived GSB is somewhat variable in our experiments, appearing just below 670nm in $DHSQ(OH)_2$ films (Figure 5.3) in the 1000ps time slices, and above 670nm in $DBSQ(OH)_2$ films (Figure 5.2) in the 1000ps time slices. The position of the steady state absorbance peak for a Squaraine monomer in a thin film is confirmed by the literature to appear at around 678nm due to a changing dielectric constant of the environment [84], [106]. We note that assignment of this long-lived component to a monomer GSB necessarily implies that the overall negative signal at 675nm is a conglomeration of the GSB of the HCT(-) species and the now assigned monomer. We will further discuss the contributions of each species (Monomer and HCT(-)) to this overall signal (*ca.* 675 nm) in the next section.

Two positive features, 465nm (in all experiments) and 525nm (in all $DHSQ(OH)_2$ experiments and with 645nm excitation in $DBSQ(OH)_2$ experiments), emerge immediately after excitation and decrease to zero within the first 1000ps. Their kinetic behavior resembles the HCT(+) ground state bleach (GSB), suggesting they are excited state absorptions (ESAs) of the HCT. Considering 550nm excites HCT(+) and 645nm excites HCT(-), it's unexpected that both wavelengths produce identical ESAs. It's improbable that both HCT states have identical energy gaps; a more likely explanation is that the HCT state relaxes into another state, creating the ESA. Possible ESA origin states include HCT(-), charge transfer (CT), and bright and dark donor-acceptor (DHA) states.

Transitions to CT or DHA(bright) from HCT(-) would need an upward energy transition, making them less likely. We initially claim that the 465nm feature is an ESA from HCT(-), and the 525nm feature is an ESA from DHA(dark). The 465nm HCT(-) ESA is present when HCT is excited and may result from direct HCT(-) excitation or relaxation from HCT(+). The 525nm feature appears only in $DHSQ(OH)_2$ films or with 645nm excitations and doesn't coincide with new

GSBs. Its absence in 550nm-excited DBSQ(OH)2 films could be due to GSB masking or a small contribution from underlying species. Since relaxation is the only expected route to populate DHA(dark), likely from HCT(-) when excited at 645nm, we further confirm the 525nm feature as an ESA of the DHA(dark) state.

The final feature, a positive signal at 620nm, persists to the conclusion of the experiment, as does the GSB at 675nm that has been so far assigned to a GSB of the monomer species. We therefore posit that this 620 nm signal is an ESA of the monomer species. However, in making this assignment, and since the 620 nm signal appears immediately, we call into question an earlier assumption that HCT is the only species populated by the pump. Given that monomers in a thin film have narrow absorbance peaks that are shifted well away from the pump wavelengths, appearing at 678 nm [84], [106], we assume that the vast and measurable majority of these monomers are populated by rapid (<2ps) energy transfer from HCT excitations, a prediction which will be validated in a later section.

### 5.3.3 Interpretations of Neat Film TA Kinetics and Properties

The assignment of the 620 nm ESA to a monomer will now be discussed. In the steady-state absorbance of annealed $DHSQ(OH)_2$ (Figure 5.1c - Purple), annealed $DBSQ(OH)_2$ (Figure 5.1c-Green), and unannealed $DHSQ(OH)_2$ (Figure 5.1b - Dashed) neat films, there is no monomer absorbance evidence; each spectrum features the HCTs' double-hump motif. We assume HCT is the dominant absorbing species in these films. Without this assumption, we cannot directly excite monomer states with 550nm excitation. However, the 620nm ESA, thought to originate from excited state monomers, appears by the 200fs time slice and in all neat film TA spectra (Figure 5.2 and 5.3). This suggests monomer excited states are populated after HCT state excitation.

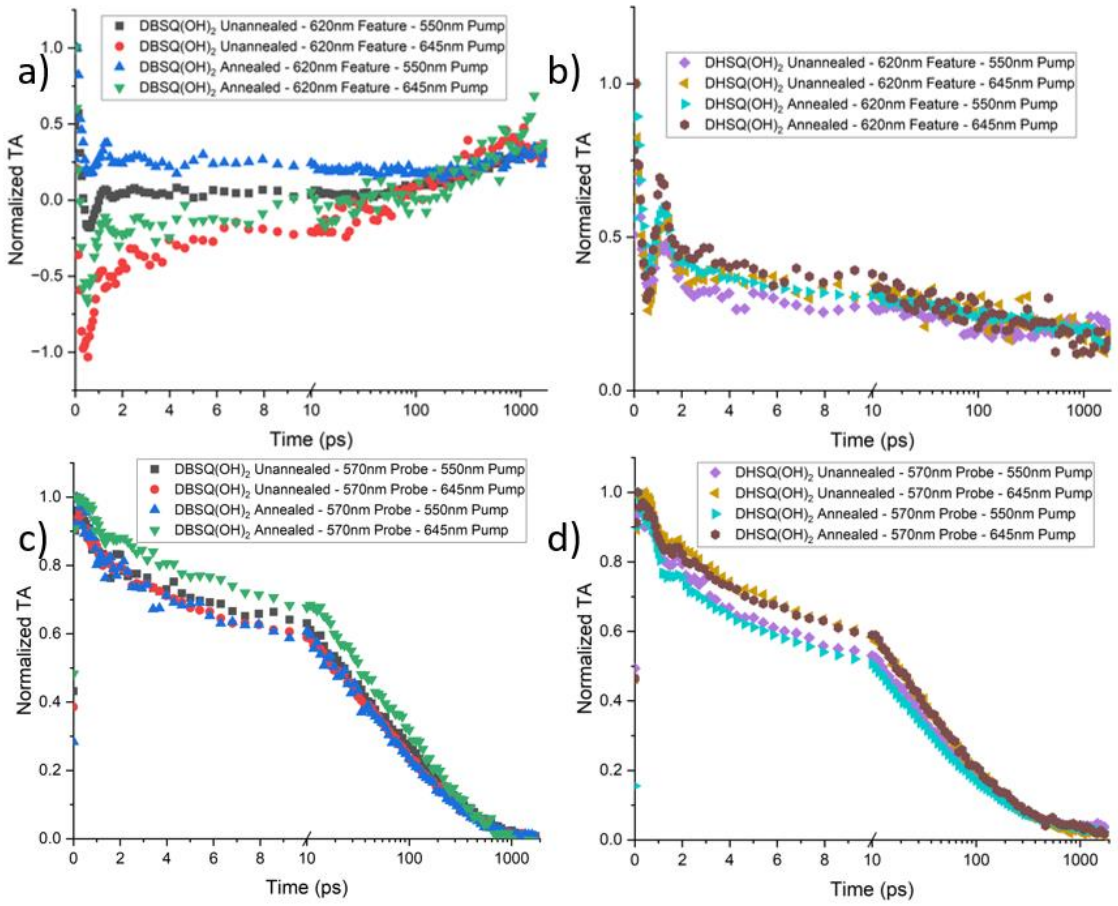


**Figure 5.4 – Kinetic Traces of the 620nm feature (a, b) and 550nm feature (c, d) for $DBSQ(OH)_2$ (a, c) and $DHSQ(OH)_2$ (b, d) neat film transient absorption measurements. Alternative versions of these Figures where the y-axis has been converted to a logarithmic scale are provided in the appendix in Figure A8.13**

In Figure 5.4, normalized kinetic traces are provided for the monomer ESA at 620nm (a and b) and the HCT(+) GSB at 570nm (c and d). In Figure 5.4a and b, monomer ESA kinetic traces of $DBSQ(OH)_2$ and $DHSQ(OH)_2$ films show a rapid decay in the first 1ps, followed by a notable regrowth and second rapid decay from time 1ps to 2ps. After the second decay, kinetic traces remain the same through the remainder of the experiment with some regrowth again at very late times for the DBSQ(OH)2 films of Figure 5.4a. In Figure 5.4c and d, the HCT(+) GSB shows a continuous rapid drop in signal during the same first 2ps, before the rate of decay slows dramatically for the remainder of the experiment. We note here that the x-axis switches to a log scale after 10 ps.

Based on the kinetic behaviors of these signals, with the assumption that these oscillations are not artifacts from the measurement, which seems unlikely, combined with the steady state and transient absorption spectral characteristics we provide the following interpretation. However, first the expected morphology is described. The steady state absorption spectrum of the neat films indicates that the samples are composed almost entirely of tightly packed HCT species with a near zero quantity of intermingled monomers between tightly packed regions [146]. We consider each film to be made up of a set of domains. In the center of each domain, we expect squaraines to be packed in a low energy structure similar to their crystal structure. As we move out from this center we expect a more random orientation of squaraines as we transition to a subsequent domain. Therefore, there will exist "isolated" monomers on the peripheral shell of each domain. The kinetic data from the first 2ps of all subfigures of Figure 5.4 is hypothesized here to arise from two competing rates. First, HCT excitons that are photoexcited next to the peripheral isolated monomers may instantaneously energy transfer into the monomer species, evidenced by the instant appearance of the 620nm signal assigned to the ESA of excited state monomers and the rapid decay in the HCT GSB signal over the first 2ps in Figure 5.4 c and d. The resulting population of excited monomers is spatially confined to a limited number of available sites based on the previous morphology description. Simultaneously, a second competing rate which depopulates the excited monomers is apparent by the rapid loss of the 620nm signal in the less than 1ps in Figure 5.4a and b. This is posited to be rapid exciton-exciton annihilation of monomer excitons as additional peripheral HCT excitons energy transfer into the already excited small population of available monomer sites. After HCT excited states close to the domain boundary have fully transitioned into the monomer sites, the rate at which monomer excited states are populated is dramatically slowed. This is because the remaining HCT excitons at the center of the domain must diffuse to the interface from greater distances through the slow Dexter mechanism. The result is an equilibrium between populating (via EnT from HCT sites) and depopulating (via Exciton-Exciton annihilation at already populated sites) for the remainder of the experiment. Since the exciton-exciton annihilation is a bimolecular

process, this decay stands out particularly in the first 2ps of the experiment but seems convoluted with the rate of steady energy transfer from central HCT states to peripheral monomers. Given that for $DBSQ(OH)_2$ the domains will be much smaller, likely because the thermodynamic drive to the crystal packing geometry is less pronounced than in $DHSQ(OH)_2$, the late time growth characteristic for the monomer ESA signal in Figure 5.4a is explained by a larger number of available monomer sites in $DBSQ(OH)_2$.

To better evaluate the behavior of excitons in our devices, where the concentration of casted solutions is typically 15mg/ml, an additional unannealed $DBSQ(OH)_2$ neat film was cast from a solution concentration of 7mg/ml, slightly greater than the other films for this experiment (4.5mg/ml). The TA response data for each of the films (4.5mg/ml and 7mg/ml) are provided in Figure A8.14 where two observations can be made. At early times, the contribution of the 620nm ESA of excited monomers is not present in the 7mg/ml (Figure A8.14a) film while clearly present in the 4.5mg/ml film (Figure A8.14b). Additionally, there is no long-lived characteristic in either the 620nm ESA of excited monomers or the 675nm monomer GSB in the 7mg/ml (Figure A8.14a). As described previously (Section 1.1.2.3), increases to the concentration of the casting solution will lead to a more crystalline film due to slower evaporation of trapped solvent within the film allowing for molecular reorganization. Consequently, we expect the higher concentration solution to produce a film with fewer available peripheral monomer sites and larger central domains of HCT given the additional reorganization time. We interpret that in a thicker film, the fewer available monomer sites and increased average HCT domain size substantially restrict energy transfer from HCT to monomer that has been identified in our lower concentration films. This is an important observation in the context of our OPV devices since solutions for device casting are at concentrations of 15mg/ml, a much greater concentration that may substantially reduce the predicted quantity of peripheral monomer sites to energy transfer into.

The 525nm signal (Table 5.2), assigned to the DHA(dark) state ESA, appears in all $DHSQ(OH)_2$ TA measurements (Figure 5.2) but only with 645nm excitation in $DBSQ(OH)_2$ films (Figure 5.3b and d). It is absent in 550nm-excited $DBSQ(OH)_2$ films (Figure 5.3a and c). The DHA(dark) state's low energy, further reduced by tighter packing [120], [168], may act as a trap, reducing OPV device performance if preferentially populated. The reduced likelihood of populating DHA(dark) in higher energy (550nm excitation) excitons in $DBSQ(OH)_2$ films, evidenced by the missing ESA in Figure 5.3a and c, and the increased monomer state availability, provide an initial explanation for higher performance $DBSQ(OH)_2$ OPV devices over $DHSQ(OH)_2$ OPV devices [84], [120]. Further evaluation of PCBM-containing films is needed and will be discussed in a later section.

### 5.3.4 Neat Film TA Conclusions

The following summary of processes is consistent with the above data. EnT from HCT to monomer occurs nearly instantaneously when these species are in close proximity at peripheral domain sites. EnT from excited HCT states that are centrally located in domains happens more slowly because of the greater distance to the domain boundaries. The Dexter energy transfer mechanism has a fast rate, faster than FRET, but only very small intermolecular spacing between energy donor and acceptor [40], [60]. Therefore, many subsequent transfers are necessary to reach the peripheral sites for HCTs that are initially excited far from the peripheral monomers at the center of domains. In contrast, that same rapid energy transfer at small intermolecular spacings allows HCT excitons initially generated near monomers at peripheral sites to EnT nearly instantly. Thus, Squaraine HCT species are posited to be extremely effective energy transfer contributors for OPV devices when the size of their corresponding domains are small because of the combination of proximal low energy monomer excited states. Energy transfer out of well-packed regions is fast initially but as the structural packing becomes less well ordered the rate of energy transfer reduces

unless monomers abound. These explanations can further be explored and validated with the inclusion of PCBM, a recognized energy sink for excited state energy in the squaraines.

In the context of OPV devices we remind the reader that the explanations provided for the trap like characteristics of the DHA(dark) state are consistent with a lower performance of DHSQ(OH)2 devices compared to DBSQ(OH)2, due to the increased likelihood of populating the DHA(dark) state in $DHSQ(OH)_2$, and a proportionally lower population of domain periphery sites for HCT excitons to energy transfer into. We will shortly see how those periphery sites will typically house the PCBM, rather than squaraine monomers, as we consider binary blends typical of OPV devices.

## 5.4 Addition of a PCBM Acceptor to Transient Absorption Measurements

Four sections below respectively describe the spectral features from the transient absorption experiment, assign the features and trends to phenomena and processes in the samples, explore the kinetics and then summarize the findings.

### 5.4.1 Blended Squaraine:PCBM Film Spectral Features

In Figure 5.5, transient absorption measurements of blended squaraine and PCBM acceptor films in a 1:1 ratio are shown for excitation at 550 nm and 645 nm, displayed on the left and right of each row respectively. The analysis combines annealed DBSQ(OH)2:PCBM (Figure 5.5a, b), annealed DHSQ(OH)2:PCBM (Figure 5.5c, d), and unannealed DHSQ(OH)2:PCBM (Figure 5.5e, f) due to their spectral similarities.

In these films, the same five signals from neat films are identified: three positive excited-state absorption (ESA) signals at 465 nm, 525 nm, and 620 nm, and two negative ground-state bleach (GSB) signals at 550 nm and 670 nm. The GSBs are attributed to HCT (550 nm and 670 nm) with some monomer GSB contribution at 670 nm. The 620 nm ESA is associated with monomer species, while the 465 nm ESA corresponds to HCT(-) species. The slight positive

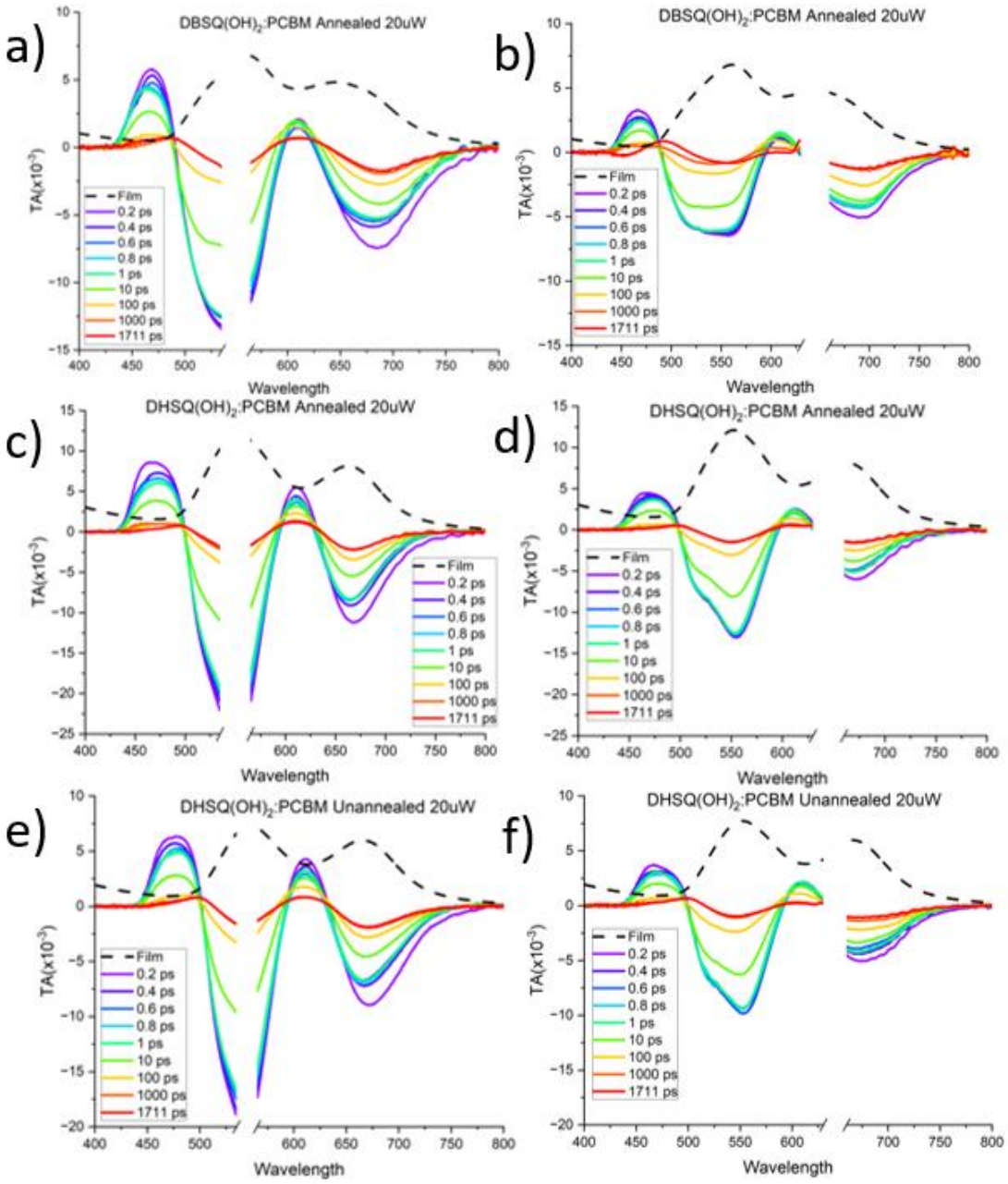


**Figure 5.5 – Transient absorption spectra of an annealed DBSQ(OH)$_2$:PCBM (a, b), annealed DHSQ(OH)$_2$:PCBM (c, d), and unannealed DHSQ(OH)$_2$:PCBM (e, f) films excited by pump wavelengths of 550nm (a, c, e) and 645nm (b, d, f).**

contribution around 525 nm that interrupts the Gaussian shape of HCT(+) GSB is still attributed to the DHA(dark) state.

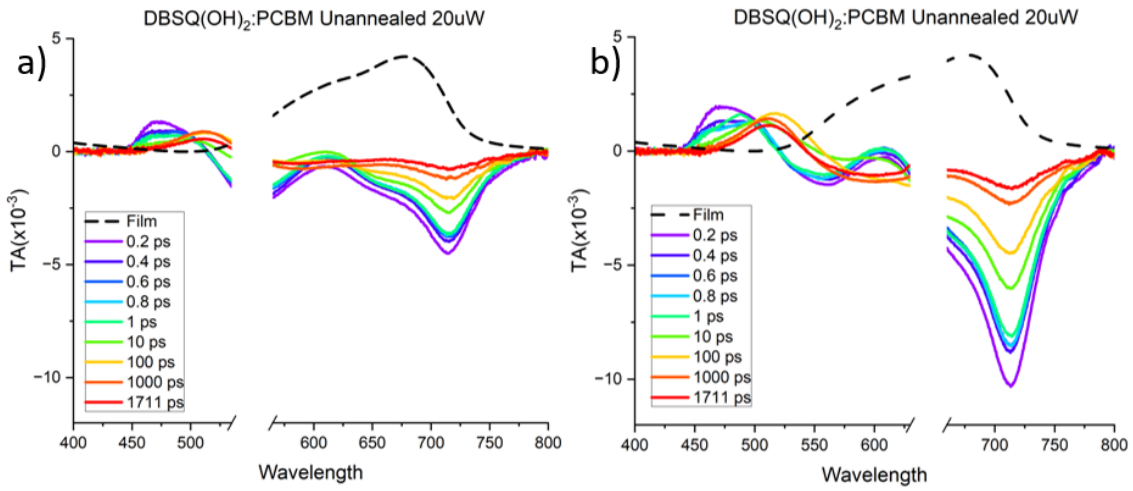


**Figure 5.6 – Transient absorption spectra of an unannealed DBSQ(OH)$_2$:PCBM film excited by a pump wavelength of a) 550 nm and b) 645 nm.**

It is important to note that the DHA(dark) state ESA remains in all films excited at 645 nm but is absent in films excited at 550 nm. The DHA(dark) state has a smaller contribution in the annealed DBSQ(OH)2:PCBM measurement (Figure 5.5b), appearing as a minor disturbance in the Gaussian, compared to both DHSQ(OH)2 measurements (Figure 5.5d and f), where it significantly disrupts the Gaussian structure of the 550 nm GSB.

For these three PCBM-containing films of Figure 5.5, there are two significant new characteristics. The first is the incomplete decay of the HCT(+) GSB at 550 nm, which persists past the conclusion of the experiment at 1711ps. In contrast, the HCT(+) GSB was largely gone by the 1000ps time slice for all neat films. This observation coincides with the second new characteristic, namely that the HCT(-) ESA remains until beyond 1711 ps. This HCT(-) ESA had decayed almost completely by 1000ps in the neat films. In addition to the persistence of the HCT(-) ESA, this feature also has a notable redshift at later times, which is not observed in the neat films.

In Figure 5.6, transient absorption spectra, with 550 nm and 645 nm excitation respectively, of the remaining unannealed DBSQ(OH)2:PCBM film are provided. The features of these measurements are quite different from all previous measurements. There is a new dominating negative signal at *ca.* 715nm that appears immediately after excitation, decaying continuously, but

remaining after the conclusion of the experiment at 1711 ps. Additionally, a broad negative signal, centered at around 600nm, begins to grow in between the 10 and 100ps time slices and remains until the conclusion of the experiment. Other signals, like those of previous measurements, are present, including the 465 nm HCT(-) ESA and the 550 nm HCT(+) GSB. The 465 nm HCT(-) ESA decays slowly until approximately 10ps, before undergoing a red shift to 515nm. This feature remains through the end of the experiment, at 1711ps. The HCT(+) GSB decays until approximately 10ps, before being overlapped by the red shifted HCT(-) ESA and the broad negative signal at *ca.* 600nm.

### 5.4.2 Identification of the TA Spectral Features of Blended Films

All features identified for the PCBM blended films of both Squaraines (annealed and unannealed) have been summarized in Table 5.3 for reference.

The assignments for the blended films are confirmed in the context of those made for the neat films. The GSBs at 550 and 675 nm are assigned to the HCT and the 465 nm ESA is assigned to the HCT(-) at least for early times before the red-shift. The 615 nm ESA is assigned to the monomer for the three films whose spectra are shown in Figure 5.5. As with the neat films some monomer GSB contributes to the overall negative signal centered at 675 nm. Finally, the subtle positive signal identified at early times around 525 nm for select experiments is still attributed to the ESA of the DHA(dark) state.

Regarding new signals, the red-shift of the 465 nm ESA at late times in all PCBM containing films is of particular interest. Since there was no red-shift in the 465 nm ESA signal in any of the neat films, it is likely a PCBM state. Keiderling *et al.* previously conducted transient absorption on neat PCBM films with a pump wavelength of 350 nm, at which PCBM absorbs [169]. They identified a positive signal at *ca.* 550 nm, which they attributed to excess free charge carrier generation in the neat PCBM film and was accompanied by a signal for the anion at wavelengths

**Table 5.3 – Summary table of all of the features identified in the PCBM blend film TA spectra of Figure 5.5 and Figure 5.6 and key decay behaviors.**

| *Wavelength (nm)* | *+/- Signal* | *Decay Comments* |
|---|---|---|
| *465* | + | **Assigned: HCT(-) ESA**<br>Signal still appears immediately after excitation at both 550nm and 645nm, never completely decays. Red-shifts to form new signal. |
| *490-515* | + | **New**<br>Positive signal appears as a red-shift of the 465nm ESA always at later times in the experiment. Extent of the red-shift varies between films. |
| *525* | + | **Assigned: DHA(dark) ESA**<br>Positive signal contribution only in films excited at 645nm of Figure 5.5 and more visible in $DHSQ(OH)_2$ films than the $DBSQ(OH)_2$ film. |
| *550* | - | **Assigned: HCT(+) GSB**<br>Signal appears immediately after excitation at both 550nm and 645nm.<br>Feature decreases in height significantly over the first 1000ps but remains constant thereafter until the limits of the experiment at 1700ps in $DHSQ(OH)_2$ and annealed $DBSQ(OH)_2$ (Figure 5.5).<br>In unannealed $DBSQ(OH)_2$ the signal is gone by 10ps (Figure 5.6). |
| *600* | - | **New**<br>Negative signal appears only in unannealed DBSQ(OH)2 film (Figure 5.6) from 10ps until the end of the experiment. |
| *620* | + | **Assigned: Monomer ESA**<br>Signal appears immediately after excitation in $DHSQ(OH)_2$ and annealed $DBSQ(OH)_2$ (Figure 5.5).<br>Signal slowly decays during remainder of experiment but never completely disappears. |
| *675* | - | **Assigned: Combination of HCT(-) GSB and Monomer GSB**<br>Signal appears immediately after excitation in $DHSQ(OH)_2$ and annealed $DBSQ(OH)_2$ (Figure 5.5).<br>Notable blue shift and peak height reduction in the first 400fs.<br>Feature decreases in height significantly over the first 1000ps but remains constant thereafter until the limits of the experiment at 1700ps. |
| *715* | - | **New**<br>Negative signal appears immediately in unannealed $DBSQ(OH)_2$ (Figure 5.6).<br>Feature decreases in height throughout experiment but never completely disappears. |

longer than 1000nm [169]. We note that this is a separation of excitons into free charge carriers within the PCBM is different from the bleaching effect of exciton generation. The red shift of the 465nm ESA is assigned to charge generation on the PCBM. Confirmation of the signal originating from a PCBM anion may require further transient absorption spectroscopy at wavelengths in the near infrared range, typical for measuring the presence of this species [169], [170] and outside of our chosen probe bandwidth. However, since we have blended Squaraine:PCBM films, and charge

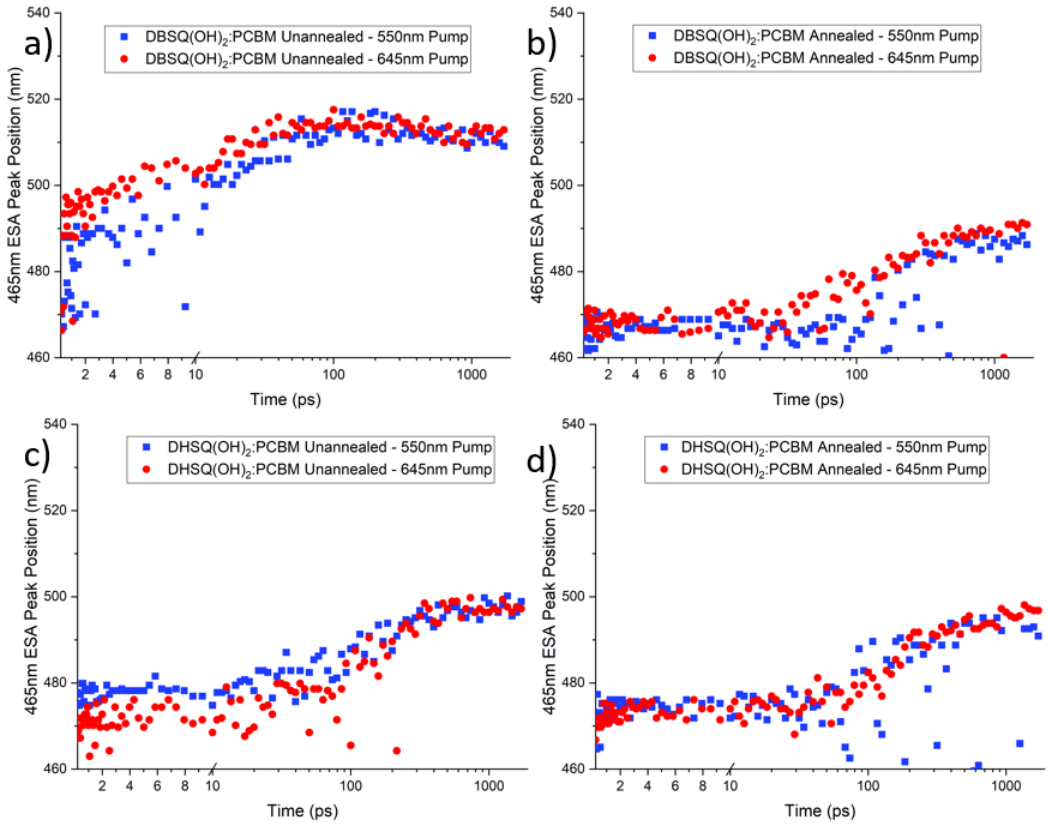


**Figure 5.7 – Transient peak position of the 465nm ESA in PCBM blended films of a)unannealed $DBSQ(OH)_2$, b)annealed $DBSQ(OH)_2$, c)unannealed $DBSQ(OH)_2$, and d)annealed $DHSQ(OH)_2$**

separation may occur at the interface between the two materials in the blend, we attribute the red shift of the 465nm ESA (the growth of the 500 nm feature) to a similar PCBM excited state. The shorter wavelength of this signal in our blended films, compared to Keiderling's 550 nm feature, may be attributed to the presence of the Squaraine altering the molecular environment around the PCBM. Hence, the extent of the red-shift and kinetics of the 465nm signal will later be used to describe the extent of charge transfer that has occurred to the PCBM.

The other signal to be discussed is the sharp negative signal at 715nm that appears only in the unannealed $DBSQ(OH)_2$:PCBM films of Figure 5.6. This signal appears immediately (sub 2ps) for both excitations and, while it decays continuously, it remains present throughout the experiment. We note that this signal is structured like the monomer of these squaraines in solution (*ca.* 650nm), albeit significantly red-shifted. Previous discussions have been made both here and

elsewhere [84], [106] regarding the red-shift of absorbance signals in thin films compared to solutions due to a changing electronic environment. Furthermore, electroluminescence from charge transfer states at the donor:acceptor interface have been shown to produce significantly red-shifted signals in transient absorption measurements for other material blends [171]. Therefore, we assign the sharp negative signal at 715nm to an electroluminescence of a Squaraine:PCBM charge-transfer complex. The lack of appearance of this signal in the other PCBM containing films in Figure 5.5 may be a consequence of its limited formation and will be discussed in the next section.

### 5.4.3 Interpretations of Squaraine:PCBM Blended Film TA Kinetics and Properties

The red-shift of the 465nm ESA in the PCBM blended films is assigned to an Squaraine:PCBM excited state complex. The population of this state can therefore be followed through its growth and, in particular, we note the loss of the 465 nm ESA feature as the Squaraine:PCBM excited state complex is populated. This apparent red-shift is illustrated in Figure 5.7 and is explored in more detail below. We first clarify how this apparent red shift must demonstrate energy transfer from HCT to monomer to a Squaraine:PCBM complex, particularly in the case of 550nm excitations where only HCT excited states may be populated by the pump. Thus, we argue that i) we excite HCT almost exclusively, ii) the red shift is absent in any neat SQ films, and iii) PCBM does not absorb at the pump wavelengths so there is neither expectation of direct absorbance nor any evidence of direct formation of PCBM excitons in short wavelength GSB. We note here for further clarification that the red-shift of the 465nm signal may also be from an isolated PCBM anion, but we are unable to confirm this from our chosen probe bandwidth. However, both our interpretation of an Squaraine:PCBM complex and a PCBM anion require that charge transfer has taken place at the interface. The great significance here is that size of this signal may be a metric for interpreting the efficiency of related devices as a charge transfer process is a necessary step in the performance of OPVs.

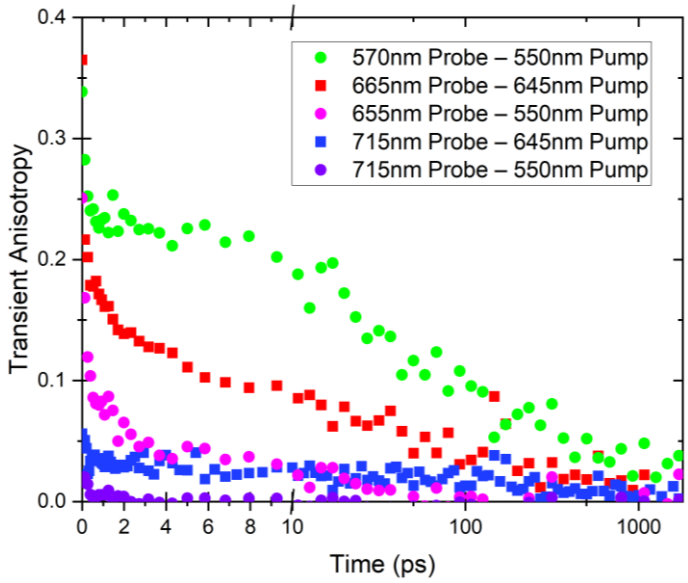


**Figure 5.8 – Transient anisotropy of select signals of unannealed DBSQ(OH)$_2$:PCBM films for both 550nm and 645nm excitations.**

The wavelength at the peak of the 460-520 nm ESA feature is plotted as a function of the pump probe delay time in the graphs shown in Figure 5.7 for all 4 films at both pump wavelengths. The graphs of Figure 5.7(b-d) all appear similar in that a red-shift, and therefore the charge transfer from monomer to SQ:PCBM charge transfer complex first occurs at approximately 20-40ps. In contrast, in Figure 5.7a, for the unannealed DBSQ(OH)$_2$:PCBM film, the red-shift begins within the first 2ps for both excitation wavelengths indicating rapid charge transfer. In considering the red-shift, we note how we cannot rule out charge transfer from HCT excited states. However, we restate that the red shift seems to imply that a charge transfer occurs from monomer squaraines at a bulk heterojunction interface with the PCBM. Nevertheless, it is important to also explore the red-shifted monomer signal at 715 nm for the unannealed DBSQ(OH)2:PCBM blend to determine its relationship with the fast formation of charged PCBM complexes.

The feature at 715 nm that we assign to a charge transfer state electroluminescence has almost insignificant overlap with the 645nm pump and zero overlap with the 550nm pump. For this reason, we claim that the species had to have been populated by energy transfer. This position is supported by data provided in Figure 5.8, where the transient anisotropy is plotted as a function of

**Table 5.4 – Time constants from exponential fitting of transient anisotropy kinetics in Figure 5.8. Percentages represent the fraction of the coefficient of each exponential to the overall amplitude.**

| *Lifetime* | *570nm Probe – 550nm Pump* | *665nm Probe – 645nm Pump* | *655nm Probe – 550nm Pump* |
|---|---|---|---|
| $\tau_1$ | 0.09 ps *(46%)* | 0.13 ps *(45%)* | 0.13 ps *(72%)* |
| $\tau_2$ | 50 ps *(36%)* | 4.8 ps *(33%)* | 5.01 ps *(25%)* |
| $\tau_3$ | 1001 ps *(18%)* | 300 ps *(22%)* | 300 ps *(3%)* |

time for unannealed $DBSQ(OH)_2$:PCBM films for both the 550nm pump (570nm, 655nm, 715nm) and 645nm pump (665nm and 715nm). The anisotropy values for 570 nm, 655 nm and 665 nm features are 0.25 or above at 0ps, with some expectation that they would approach a value of 0.4 [164] for perfect anisotropy. However, the initial anisotropy values for the 715 nm signal for each of the pump wavelengths is less than 0.06. Furthermore, any rapid decay of anisotropy for 715 nm features is complete within 500fs.

While the anisotropy of the 715nm signal is zero instantaneously, the more complex and longer-lived transient anisotropy traces in Figure 5.8 may be fit to exponential decays to better compare them. Decay time constants from fits to three exponentials are provided in Table 5.4 for probe wavelengths of 655nm (550nm excitation), 665nm (645nm excitation), and 570nm(550nm excitation). From the data in Table 5.4, each probed wavelength has a very small first decay time constant of around 100fs along with two longer lived components. The 655nm/665nm signals maintain a moderately fast decay of anisotropy (time constants of ~5ps and 300ps) while the anisotropic characteristic of the 570nm signal is very long lived (time constants of 50ps and 1001ps).

We interpret that the long-lived anisotropy of the HCT(+) 570 nm GSB results from a relatively slow energy transfer within the manifold of those HCT(+) states. Any energy transfer between HCT(+) states will likely occur without significant orientational change since relaxation

may occur through a longer-range crystal structure. These data are consistent with the slow decay of the 570 nm HCT(+) GSB feature in all graphs of Figure 5.4, representing films where either the domain size will have grown because of annealing or for $DHSQ(OH)_2$ where phase separation occurs during the spin coating process [84], [120]. Since energy transfer within a manifold of well-packed squaraines is based on a Dexter mechanism, it may be slow, since it depends critically on short intermolecular spacing and orientation.

The anisotropic decay of the 665nm/655nm signals of the unannealed DBSQ(OH)2:PCBM films is noticeably faster than the 570nm signal of the HCT species, likely due to the monomer GSB that overlaps with the HCT(-) GSB. We note that energy transfer to a monomer will necessarily lead to a loss of anisotropy since that monomer is differentiated, by definition, by different collective orientations and likely different transition dipole moment orientations relative to the pump beam polarization. Furthermore, the faster component of the anisotropic decay can be attributed to the population of a diverse array of these monomer species. This interpretation is consistent with the analysis of the neat films where fast energy transfer from HCT to monomer was attributed to the proximity of HCT to monomer at the periphery of the squaraine domains.

Again, the 715nm feature appears instantaneously, has no apparent anisotropy, and has been assigned to an electroluminescence from a Squaraine:PCBM charge transfer species. It is populated here not by direct photoexcitation but by rapid energy transfer likely from both the HCT (in the case of the 550/645nm excitation) or less red-shifted monomers (645nm excitation). Additionally, we infer that the exciton undergoes charge transfer at the interface to the PCBM, evidenced by an equally rapid red-shift of the 465nm ESA in Figure 5.7a. For 550nm excitations, where HCT must be the only initially excited species, we further infer a rapid energy transfer from HCT to the charge transfer species of interfacial Squaraines and PCBM.

### 5.4.4 PCBM Blend Films TA Discussion and Conclusions

By introducing a PCBM acceptor into the SQ film, we provide a pathway for charge separation at the interface of the SQ:PCBM. This charge separated state introduces the possibility of a SQ cation and PCBM anion signal as an indicator of successful charge separation. It is important to recognize that the appearance of either of these signals necessitates that the exciton was able to reach the interface through energy transfer or in the case that it was populated directly.

Additionally, PCBM will influence the aggregation properties of SQs, particularly at domain interfaces between the two materials. Because PCBM will introduce impurities to otherwise pure SQ domains, the interface of the two materials can be predicted to have a greater monomer population due to the intermixing of the SQ and PCBM. This is particularly expected for $DBSQ(OH)_2$ which blends well with the PCBM. Because of this intermixing at the interface, we expect an increase in the volume of our shell of monomers, as described in a microstructure description in section 5.3.3. However, annealed blends will still likely have a reduction in this volume when the system moves towards a thermodynamic equilibrium defined by phase separation.

The sub 2ps formation of the SQ:PCBM charge transfer complex in unannealed DBSQ(OH)2:PCBM films is interesting in that it correlates with the highest performing devices discussed in previous chapters.

In summary, we conclude that i) rapid energy transfer from HCT to monomers occurs within squaraine domains, ii) rapid charge transfer occurs at the interface of Squaraines and PCBM once an excited state has been populated at the periphery of a squaraine domain, either via direct excitation or through energy transfer, iii) the time for diffusion of any excited state to the domain periphery, (and hence for charge transfer to PCBM) depends on the distance to that periphery from the location of initial photoexcitation, iv) HCT species may undergo efficient energy transfer through the Dexter mechanism but generation of charged PCBM (and therefore higher

photocurrent) is limited by the diffusion distance, and indeed by overly large material domains rather than the excited state species within those domains. In the case of annealed blended films, or even unannealed $DHSQ(OH)_2$:PCBM films, domains are dramatically enlarged due to the marked phase separation. The result is a dramatic increase in the average distances excitons must travel to reach the interfaces. Furthermore, a reduction in total interfacial surface area, due to increased phase separation, further depletes the capacity of excitons to reach the interface due to fewer available monomer sites relative to the number of HCTs. The result therefore is that HCT states must be capable of efficient energy transfer through the Dexter mechanism and are not inherently bad for the performance of OPVs. Rather it is the coexistence of the larger Squaraine domains and a reduction in monomer interface sites which limits their performance and necessarily reduces the efficiency of corresponding devices.

## 5.5 Conclusions

The original goal of this chapter was evaluating the energy transfer properties of charge transfer H-aggregates, in a variety of Squaraine morphologies, and identifying the contribution of their energy transfer efficiency to OPV efficiency without other influential variables such as charge mobility. Previous studies on dimer H-aggregates have produced results pointing to preferential energy transfer from monomers to the dimer species. However, results here have identified sub picosecond energy transfer from charge-transfer H-aggregates to peripheral monomers in both neat films and in PCBM blended films, evidenced by the rapid formation of excited state monomer associated signals in all transient absorption spectra presented here. Furthermore, the overall direction of excitons in squaraines was shown to proceed preferentially from HCTs to monomers, the opposite of what literature has shown for DHAs and monomers where excitons preferentially moved from monomer to DHA. However, energy transfer from HCTs to monomers was shown here to be heavily restricted in films with larger HCT domains due to the longer necessary distance to peripheral monomers. The rapid energy transfer characteristics of these charge transfer H-

aggregates for short intermolecular separations strongly suggests that the Dexter energy transfer mechanism is responsible. After population of the few available monomer sites, rapid depletion follows through an exciton-exciton annihilation mechanism due to limited available monomer sites.

We also identified the formation of a Squaraine:PCBM charge transfer complex in as little as 2-4ps after excitation of the charge transfer H-aggregate, evidenced by the instantaneous appearance of charge transfer electroluminescence and excess charge generation on the PCBM. This is an essential feature in the consideration of how these species contribute to overall OPV efficiency as formation of the charge transfer state is a key step in the OPV mechanism. However, once again deeper HCT excitations, populated far from peripheral monomers, in larger domains of HCT were identified as undergoing much slower formation of the Squaraine:PCBM charge transfer complex with times closer to 20-40ps, an order of magnitude slower than in highly mixed films with smaller domains. In the context of OPV this leads to two key conclusions. The first is that charge-transfer H-aggregates can undergo rapid energy transfer at short intermolecular separations, likely through the dexter mechanism. The second, a consequence of the first, is that phase separation must be limited, and highly mixed films are essential to reap the benefits of this rapid energy transfer and ensure that HCT excitons may reach the interface. In the next chapter we will draw key connections of the TA work and conclusions presented here to OPV device performance of the previous chapters.

# 6 Summary, Conclusions, and Future Work

This dissertation examines how Squaraine HCTs impact the efficiency of OPV devices, focusing on the role of morphology and energy transfer properties. By studying the limitations of the charge transfer H-aggregate and identifying the optimal morphology for a squaraine-based OPV device, this research aims to provide a framework for improving device efficiency and lifespan, with the goal of commercialization for Squaraine based OPVs.

Chapter 3 focuses on the efficiency contribution of the squaraine molecule $DBSQ(OH)_2$ in its monomer, DHA, and HCT forms in devices, specifically quantifying the populations of each species. In section 3.2, $DBSQ(OH)_2$ excited state populations were quantified using detailed absorption measurements of $DBSQ(OH)_2$:PCBM unannealed and annealed films with a varying $DBSQ(OH)_2$ fraction. A transition from mostly Squaraine monomers to an increasing absorption and population of DHAs was observed in the unannealed films with increasing $DBSQ(OH)_2$ fraction. In the annealed films, increasing $DBSQ(OH)_2$ fraction instead produced a transition from Squaraine monomers to mostly HCT excited states at higher fractions. In all films, the fraction of Squaraine HCTs was quantified using separate spectral subtraction and gaussian fit approaches with similar results for both shown in Figure 3.2. A population interchange between monomers in dilute mixtures, dimers in concentrated mixtures, and HCTs in pure/crystalline regions was identified.

In section 3.3, we sought to measure the extinction coefficient (α) of the HCT species. Film thicknesses for each blend ratio, annealed and unannealed, were measured using atomic force microscopy. A measured thickness of a 100% $DBSQ(OH)_2$ annealed film ($d$), assumed to be entirely crystalline HCT, combined with absorbance ($A$) yielded the extinction coefficient of the HCT species according to $A = \alpha d$, plotted in Figure 3.4. With this extinction coefficient, we were able to determine the effective thickness associated with the HCT species in any film. $DBSQ(OH)_2$:PCBM films were then dissolved to determine the exact mass of $DBSQ(OH)_2$ and

PCBM on each film which, when combined with known thickness data, allowed us to determine Squaraine density upon changes to blend ratio and annealing. The thickness data in Figure 3.3 deviated from the linear tie between 0%$DBSQ(OH)_2$ and 100% $DBSQ(OH)_2$ that was expected for two materials with fixed densities. The observed thicknesses suggested an incorporation of smaller $DBSQ(OH)_2$ molecules into PCBM at low SQ wt.% blend ratios and confirmed our interpretation that $DBSQ(OH)_2$ mixes well with PCBM.

Organic solar cells of each blend ratio, annealed and unannealed, were fabricated and tested in section 3.5. The device data, presented in Figure 3.4, revealed two optimized device blends of 38% $DBSQ(OH)_2$ in unannealed devices and 59% $DBSQ(OH)_2$ in annealed devices. For the 40 wt.% $DBSQ(OH)_2$ unannealed films, dimerization of $DBSQ(OH)_2$ was substantial, yet $DBSQ(OH)_2$ remained well mixed with PCBM. We interpreted therefore that $DBSQ(OH)_2$, while largely phase separated, retained small domain sizes through the preferential mixing of $DBSQ(OH)_2$ and PCBM. For the annealed 60% $DBSQ(OH)_2$ films, approximately 90% of the Squaraine was HCT (Figure 3.2). The extensive phase separation likely in higher weight% devices, combined with thermal energy from annealing, was predicted to produce highly crystalline domains. The improved crystallinity and concomitant mobility likely overcome any *possible* stifling of exciton diffusion due to HCT or large domain formation.

Chapter 3 demonstrated how some level of mixing is valuable in molecular devices. In well-mixed samples, the distance required for exciton diffusion to a BHJ interface is short, while the charge mobility would expectedly be lowered. On the other hand, device data also supported the possibility that crystal packing may ultimately help the efficiency of the device despite the formation of charge transfer coupled H-aggregates for which fluorescence is quenched and therefore for which energy transfer *may* be stifled. However, questions remained unanswered about device implications of HCTs specifically and concomitant phase separation.

In chapter 4 we considered the incorporation of two different Squaraine donors in a two donor, one acceptor ternary blend with PCBM. $DBSQ(OH)_2$ which blends well with PCBM, was hypothesized to be capable of breaking up pure Squaraine domains by acting as a surfactant between $DHSQ(OH)_2$ and PCBM, which were shown to phase separate upon casting otherwise. It was hypothesized that Squaraine intermixing would therefore allow some control over the extent of aggregation and phase separation.

In section 4.2, absorbance spectra and KPFM images provided a clear description of the extent of HCT formation and phase separation in Squaraine:PCBM blends. $DBSQ(OH)_2$ tended to blend well with PCBM, demonstrated by homogeneous mixing and absorption features that indicated predominantly monomer and dimer H-aggregate formation. In contrast, $DHSQ(OH)_2$ blended poorly with PCBM, with increases to both HCT populations and domain size. Upon combining both Squaraines with PCBM, ternary blend absorption spectra showed reduced HCT formation for $DHSQ(OH)_2$, even with $DBSQ(OH)_2$ weight fractions as low as 10%. Furthermore, ternary blend KPFM images showed decreasing domain size as the relative weight percent of $DBSQ(OH)_2$ increased, illustrating markedly reduced phase separation with added $DBSQ(OH)_2$. The combination of spectroscopic assignments and KPFM images confirmed that $DBSQ(OH)_2$ acted not only by breaking apart $DHSQ(OH)_2$ aggregation, but also as a surfactant encouraging blending with the PCBM acceptor.

In section 4.3, the performance of ternary blend devices was correlated with the changing morphology properties identified in section 4.2. For 0%-65% $DBSQ(OH)_2$ blends, where phase separation was clearly observable in the KPFM images, average PCE never exceeded 2.52%. Phase separation and larger domains partly explained the lower performance of higher $DHSQ(OH)_2$ weight fraction devices. However, phase separation alone failed to explain the notable dip in performance of 20%-65% $DBSQ(OH)_2$ blends below a predicted tie line in Figure 4.4. Devices with 0% and 10% $DBSQ(OH)_2$ fractions, where phase separation was maximized, had higher

efficiencies than 20%-65% $DBSQ(OH)_2$ blends. Limited energy transfer across phase separated regions of HCT was thus refuted as the main cause for efficiency loss. IQE measurements revealed that PCE was driven further downwards due to the broad distribution of states and increased likelihood of low-energy traps from diverse excited state populations.

In section 4.4, we evaluated the effects of low temperature annealing on the morphology and efficiency of ternary blend devices. KPFM images revealed limited further domain enlargement after annealing when compared to unannealed films. However, there was sufficient thermal energy for crystallization in already formed Squaraine domains, significantly increasing HCT formation spectral motifs in all annealed absorbance. However, we observed slightly less HCT formation in annealed films containing large fractions of $DBSQ(OH)_2$, further indicating that $DBSQ(OH)_2$ can break up $DHSQ(OH)_2$ aggregates. Because phase separation was not observed in annealed blends while HCT formation was extensive, we could evaluate the effects of HCT formation without concomitant domain enlargement. Annealed ternary blend device data revealed that five of the nine ternary blends had a statistically significant increase in PCE after annealing while only one blend ratio had a significant efficiency loss. If the HCT species was inherently a source of poor performance through *potential* poor energy transfer characteristics, we would expect devices to decrease in performance. Instead, the increase in PCE indicated that HCTs, or crystallization, were not bad for device performance. Furthermore, the combination of two Squaraines in a ternary blend was shown to help preserve the morphology of the as-cast film by preventing significant phase separation. Since an enhancement in device performance was observed with increased HCT formation when phase separation was restricted, further investigation into specifically energy transfer of HCTs was required.

Chapters 3 and 4 showed that the formation of HCTs in organic photovoltaics (OPVs) is not inherently detrimental to overall device efficiency. Instead, the efficiency loss appears to be primarily due to larger domain sizes and diverse excited state populations. Furthermore, highly

efficient OPVs typically have smaller domain sizes, even when HCTs are the predominant species within the active layer as shown in chapter 4. In chapter 5, we wanted to specifically evaluate the energy transfer properties of HCTs and their contribution to device efficiency, separate from other steps in the OPV mechanism.

To analyze HCT energy transfer properties, we utilized transient absorption measurements to monitor the excited state kinetics of Squaraine excited states in thin films. In section 5.3, transient absorption spectra of neat Squaraine films were presented. In neat films we observed only the kinetics of Squaraine excited states as there was no possibility for charge separation at a donor:acceptor interface. We assumed a morphology where HCTs are most prominent near the center of Squaraine domains, due to increased squaraine density and reduced mixing, while near domain interfaces there is likely an increase in monomer population. This assumption implied that a preferential motion of excitons from HCTs to monomers would benefit devices. A key observation in all neat films was the appearance of multiple monomer signals. This was particularly of interest after 550nm excitations, where only the HCT species absorbs. It was determined that *monomer excited states were populated through energy transfer after HCT state excitation*. Isolated monomers on the peripheral shell of each domain were determined to be instantaneously populated by HCT excitons photoexcited nearby. This was attributed to the Dexter energy transfer mechanism which is very rapid for small intermolecular spacing. Simultaneously, a rapid depopulation of excited monomers was identified and posited to be rapid exciton-exciton annihilation due to the small population of available monomer sites already excited. At longer probe delay times, the rate at which monomers were populated was dramatically slowed and was attributed to HCT excitons nearer to the center of the domain diffusing to the interface from greater distances.

When considering neat film observations in the context of our device work in chapter 3 and 4, it further confirms the interpretation that small domain sizes are essential to the performance of the device, particularly for the HCT species. Squaraine HCT species were determined to be

extremely effective energy transfer contributors for OPV devices, capable of transferring energy to monomer sites nearly instantaneously via the Dexter mechanism. Consequently, devices with fewer available monomer sites and increased average HCT domain size due to extensive phase separation and crystallization will have substantially restricted Dexter energy transfer from HCT to monomer.

To better understand the behavior of HCTs in a complete OPV device, PCBM blended films were subsequently measured using TA. In section 5.4, the TA measurements of blended films of squaraine with a PCBM acceptor in a 1:1 ratio were provided. New signals were assigned specifically to the formation of a Squaraine-PCBM charge transfer complex in all films. It was determined that charge separation at the interface first occurs at approximately 20-40 ps in films with large domains (unannealed $DHSQ(OH)_2$:PCBM, annealed $DHSQ(OH)_2$:PCBM, and annealed $DBSQ(OH)_2$:PCBM). In contrast, the unannealed $DBSQ(OH)_2$:PCBM film showed charge transfer complex formation in as little as 2 ps. Additionally, long-lived anisotropy of the HCT(+) signal confirmed a relatively slow energy transfer mechanism within the manifold of HCT states, a consequence of the critical dependence on short intermolecular spacing and orientation of the Dexter energy transfer mechanism.

The goal of chapter 5 was evaluating specifically the energy transfer properties of HCTs, and thus determining HCT contributions to overall OPV efficiency. Sub picosecond energy transfer from HCTs to peripheral monomers, in both neat films and in PCBM blended films, likely proceeding through the Dexter mechanism, was observed. Additionally, the preferred direction of excitons in Squaraines proceeds from HCTs to monomers, a key outcome in the context of enhancing the efficiency of OPV devices. Furthermore, identification of the formation of a Squaraine:PCBM charge transfer complex, in as little as 2-4ps after excitation of HCTs, further confirms significant potential for HCT contribution to OPV efficiency. However, energy transfer from HCTs to monomers and eventual charge transfer species was shown to be heavily influenced by the size of domains with excessive domain enlargement dramatically slowing exciton motion.

Deeper HCT excitations in larger domains of HCT were identified as undergoing a slower formation of the Squaraine:PCBM charge transfer complex with times closer to 20-40ps. It is clear from this work that *HCTs can undergo rapid energy transfer, likely through the dexter mechanism*. However, *well mixed films with small domains are essential* to benefit from the rapid energy transfer and ensure that all HCT excitons may reach the interface.

In conclusion, the work in this dissertation has led to several key outcomes in the push towards both the commercialization and research value of Squaraine based OPVs. There is a clear importance in the mixing properties of materials and a need for materials which remain well mixed in their thermodynamic equilibrium. Dramatic differences in the blending characteristics of similar Squaraine derivatives has been shown to allow for a diverse array of active layer morphologies in both as cast films and in thermally equilibrated films. Furthermore, the diverse series of excited state species for Squaraines separates them from other materials, making them fantastic candidates for critical evaluation of excited state properties. Dexter energy transfer in Squaraines has been observed to occur remarkably fast and despite a lack of fluorescence from the charge transfer H-aggregate species. Direct observation of a Squaraine:PCBM charge transfer complex provides a key advantage for Squaraines regarding evaluation of OPVs. Formation of the charge transfer species at the donor:acceptor interface is a key step in the OPV operation mechanism, making the ability to observe and study it essential for improving devices. Further consideration of Squaraines and their beneficial properties for the OPV clearly has the potential to drive OPV research towards technological improvement and commercialization.

To continue the development of OPV technology, there are several potential steps that could be taken to further develop Squaraines as a commercial opportunity. While we identified the formation of a Squaraine:PCBM charge transfer complex, it was without confirmation of the PCBM anion formation. The charge transfer complex may have trap-like characteristics, preventing separation into free charge carriers. To ensure that there is no significant exciton loss from trapping

at the interface, it would be valuable to verify the efficiency of formation of a PCBM anion from the Squaraine:PCBM charge transfer complex.

Additionally, it has been confirmed that small, well mixed domains are essential to device performance for all underlying species. Identifying materials that mix ideally for OPV in their thermodynamic equilibrium is therefore essential. Ensuring that long term phase separation is limited, or entirely prevented, is essential to commercialization. We confirmed ternary blends with two Squaraines have reduced phase separation for short duration, low temperature annealing while still allowing for beneficial crystallization in small, already formed domains. Thus, combining multiple Squaraines may provide a pathway to limiting phase separation over a device's lifetime. Identifying the limitations of the observed reduction in phase separation for mixed Squaraines, both at longer times and with higher temperatures, may lead to a solution for phase separation concerns in longer lifetime devices.

Throughout this thesis, we consistently used PCBM as the acceptor, which inherently limits device efficiency. While PCBM's consistent packing and limited performance variability helped simplify our study, its poor absorption characteristics restrict device performance. In contrast, Squaraines have high extinction coefficients, and the HCT species' broadened absorbance aligns well with the solar spectrum (500-800nm). Pairing Squaraines with a more suitable acceptor that promotes a well-mixed morphology and provides complementary absorbance could lead to substantial efficiency improvements.

# 7 References


[1] D. M. Chapin, C. S. Fuller, and G. L. Pearson, “A New Silicon p-n Junction Photocell for Converting Solar Radiation into Electrical Power,” *J. Appl. Phys.*, vol. 25, no. 5, pp. 676–677, May 1954, doi: 10.1063/1.1721711.

[2] “Crystalline Silicon Photovoltaics Research,” *Energy.gov*. https://www.energy.gov/eere/solar/crystalline-silicon-photovoltaics-research (accessed May 15, 2021).

[3] G. Conibeer, “Third-generation photovoltaics,” *Mater. Today*, vol. 10, no. 11, pp. 42–50, Nov. 2007, doi: 10.1016/S1369-7021(07)70278-X.

[4] K. A. Mazzio and C. K. Luscombe, “The future of organic photovoltaics,” *Chem. Soc. Rev.*, vol. 44, no. 1, pp. 78–90, Dec. 2014, doi: 10.1039/C4CS00227J.

[5] D. Kearns and M. Calvin, “Photovoltaic Effect and Photoconductivity in Laminated Organic Systems,” *J. Chem. Phys.*, vol. 29, no. 4, p. 950, Aug. 2004, doi: 10.1063/1.1744619.

[6] M. Zhang *et al.*, “Single-layered organic photovoltaics with double cascading charge transport pathways: 18% efficiencies,” *Nat. Commun.*, vol. 12, no. 1, Art. no. 1, Jan. 2021, doi: 10.1038/s41467-020-20580-8.

[7] S.-I. Na, S.-S. Kim, J. Jo, and D.-Y. Kim, “Efficient and Flexible ITO-Free Organic Solar Cells Using Highly Conductive Polymer Anodes,” *Adv. Mater.*, vol. 20, no. 21, pp. 4061–4067, 2008, doi: 10.1002/adma.200800338.

[8] X. Fu, L. Xu, J. Li, X. Sun, and H. Peng, “Flexible solar cells based on carbon nanomaterials,” *Carbon*, vol. 139, pp. 1063–1073, Nov. 2018, doi: 10.1016/j.carbon.2018.08.017.

[9] K. Fukuda, K. Yu, and T. Someya, “The Future of Flexible Organic Solar Cells,” *Adv. Energy Mater.*, vol. 10, no. 25, p. 2000765, 2020, doi: 10.1002/aenm.202000765.

[10] J. Zhang *et al.*, “Highly Efficient Semitransparent Organic Solar Cells with Color Rendering Index Approaching 100,” *Adv. Mater.*, vol. 31, no. 10, p. 1807159, 2019, doi: 10.1002/adma.201807159.

[11] X. Li *et al.*, “Semitransparent Organic Solar Cells with Vivid Colors,” *ACS Energy Lett.*, vol. 5, no. 10, pp. 3115–3123, Oct. 2020, doi: 10.1021/acsenergylett.0c01554.

[12] Y. Zhang, I. D. W. Samuel, T. Wang, and D. G. Lidzey, “Current Status of Outdoor Lifetime Testing of Organic Photovoltaics,” *Adv. Sci.*, vol. 5, no. 8, p. 1800434, 2018, doi: https://doi.org/10.1002/advs.201800434.

[13] S. A. Gevorgyan *et al.*, “Lifetime of Organic Photovoltaics: Status and Predictions,” *Adv. Energy Mater.*, vol. 6, no. 2, p. 1501208, 2016, doi: 10.1002/aenm.201501208.

[14] F. Campana, C. Kim, A. Marrocchi, and L. Vaccaro, “Green solvent-processed organic electronic devices,” *J. Mater. Chem. C*, vol. 8, no. 43, pp. 15027–15047, Nov. 2020, doi: 10.1039/D0TC03610B.

[15] S. Zhang, L. Ye, H. Zhang, and J. Hou, “Green-solvent-processable organic solar cells,” *Mater. Today*, vol. 19, no. 9, pp. 533–543, Nov. 2016, doi: 10.1016/j.mattod.2016.02.019.

[16] G. Bernardo, T. Lopes, D. G. Lidzey, and A. Mendes, “Progress in Upscaling Organic Photovoltaic Devices,” *Adv. Energy Mater.*, vol. 11, no. 23, p. 2100342, 2021, doi: 10.1002/aenm.202100342.

[17] R. Po and J. Roncali, “Beyond efficiency: scalability of molecular donor materials for organic photovoltaics,” *J. Mater. Chem. C*, vol. 4, no. 17, pp. 3677–3685, Apr. 2016, doi: 10.1039/C5TC03740A.

[18] R. Po, G. Bianchi, C. Carbonera, and A. Pellegrino, “‘All That Glisters Is Not Gold’: An Analysis of the Synthetic Complexity of Efficient Polymer Donors for Polymer Solar Cells,” *Macromolecules*, vol. 48, no. 3, pp. 453–461, Feb. 2015, doi: 10.1021/ma501894w.

[19] Y. Cui *et al.*, “Over 16% efficiency organic photovoltaic cells enabled by a chlorinated acceptor with increased open-circuit voltages,” *Nat. Commun.*, vol. 10, no. 1, pp. 1–8, Jun. 2019, doi: 10.1038/s41467-019-10351-5.

[20] Y. Cai *et al.*, “A Well-Mixed Phase Formed by Two Compatible Non-Fullerene Acceptors Enables Ternary Organic Solar Cells with Efficiency over 18.6%,” *Adv. Mater.*, vol. 33, no. 33, p. 2101733, 2021, doi: 10.1002/adma.202101733.

[21] J. Yuan *et al.*, “Single-Junction Organic Solar Cell with over 15% Efficiency Using Fused-Ring Acceptor with Electron-Deficient Core,” *Joule*, vol. 3, no. 4, pp. 1140–1151, Apr. 2019, doi: 10.1016/j.joule.2019.01.004.

[22] W. Zhao *et al.*, “Molecular Optimization Enables over 13% Efficiency in Organic Solar Cells,” *J. Am. Chem. Soc.*, vol. 139, no. 21, pp. 7148–7151, May 2017, doi: 10.1021/jacs.7b02677.

[23] J. Sun *et al.*, “Dithieno[3,2-b:2’,3’-d]pyrrol Fused Nonfullerene Acceptors Enabling Over 13% Efficiency for Organic Solar Cells,” *Adv. Mater.*, vol. 30, no. 16, p. 1707150, 2018, doi: 10.1002/adma.201707150.

[24] W. Li, L. Ye, S. Li, H. Yao, H. Ade, and J. Hou, “A High-Efficiency Organic Solar Cell Enabled by the Strong Intramolecular Electron Push–Pull Effect of the Nonfullerene Acceptor,” *Adv. Mater.*, vol. 30, no. 16, p. 1707170, 2018, doi: 10.1002/adma.201707170.

[25] L. Zuo, X. Shi, S. B. Jo, Y. Liu, F. Lin, and A. K.-Y. Jen, “Tackling Energy Loss for High-Efficiency Organic Solar Cells with Integrated Multiple Strategies,” *Adv. Mater.*, vol. 30, no. 16, p. 1706816, 2018, doi: 10.1002/adma.201706816.

[26] X. Che, Y. Li, Y. Qu, and S. R. Forrest, “High fabrication yield organic tandem photovoltaics combining vacuum- and solution-processed subcells with 15% efficiency,” *Nat. Energy*, vol. 3, no. 5, p. 422, May 2018, doi: 10.1038/s41560-018-0134-z.

[27] L. Meng *et al.*, “Organic and solution-processed tandem solar cells with 17.3% efficiency,” *Science*, vol. 361, no. 6407, pp. 1094–1098, Sep. 2018, doi: 10.1126/science.aat2612.

[28] C. J. M. Emmott *et al.*, “In-situ, long-term operational stability of organic photovoltaics for off-grid applications in Africa,” *Sol. Energy Mater. Sol. Cells*, vol. 149, pp. 284–293, May 2016, doi: 10.1016/j.solmat.2016.01.036.

[29] R. Po, A. Bernardi, A. Calabrese, C. Carbonera, G. Corso, and A. Pellegrino, “From lab to fab: how must the polymer solar cell materials design change? – an industrial perspective,” *Energy Environ. Sci.*, vol. 7, no. 3, pp. 925–943, Feb. 2014, doi: 10.1039/C3EE43460E.

[30] M. Tian, M. Furuki, I. Iwasa, Y. Sato, L. S. Pu, and S. Tatsuura, “Search for Squaraine Derivatives That Can Be Sublimed without Thermal Decomposition,” *J. Phys. Chem. B*, vol. 106, no. 17, pp. 4370–4376, May 2002, doi: 10.1021/jp013698r.

[31] G. Chen, H. Sasabe, T. Igarashi, Z. Hong, and J. Kido, “Squaraine dyes for organic photovoltaic cells,” *J. Mater. Chem. A*, vol. 3, no. 28, pp. 14517–14534, Jul. 2015, doi: 10.1039/C5TA01879J.

[32] M. C. Scharber and N. S. Sariciftci, “Efficiency of bulk-heterojunction organic solar cells,” *Prog. Polym. Sci.*, vol. 38, no. 12, pp. 1929–1940, Dec. 2013, doi: 10.1016/j.progpolymsci.2013.05.001.

[33] C. Guillén and J. Herrero, “High-Performance Electrodes for Organic Photovoltaics,” in *Organic Photovoltaics: Materials, Device Physics, and Manufacturing Technologies*, 2009, pp. 399–423. doi: 10.1002/9783527623198.ch14.

[34] K. Wang, C. Liu, T. Meng, C. Yi, and X. Gong, “Inverted organic photovoltaic cells,” *Chem. Soc. Rev.*, vol. 45, no. 10, pp. 2937–2975, May 2016, doi: 10.1039/C5CS00831J.

[35] C. McDowell, M. Abdelsamie, M. F. Toney, and G. C. Bazan, “Solvent Additives: Key Morphology-Directing Agents for Solution-Processed Organic Solar Cells,” *Adv. Mater.*, vol. 30, no. 33, p. 1707114, 2018, doi: 10.1002/adma.201707114.

[36] V. Negi, O. Wodo, J. J. van Franeker, R. A. J. Janssen, and P. A. Bobbert, “Simulating Phase Separation during Spin Coating of a Polymer–Fullerene Blend: A Joint Computational and Experimental Investigation,” *ACS Appl. Energy Mater.*, vol. 1, no. 2, pp. 725–735, Feb. 2018, doi: 10.1021/acsaem.7b00189.

[37] M. Shibata, Y. Sakai, and D. Yokoyama, “Advantages and disadvantages of vacuum-deposited and spin-coated amorphous organic semiconductor films for organic light-emitting diodes,” *J. Mater. Chem. C*, vol. 3, no. 42, pp. 11178–11191, Oct. 2015, doi: 10.1039/C5TC01911G.

[38] A. F. Huq, A. Ammar, A. M. Al-Enizi, and A. Karim, “In-situ orientation and crystal growth kinetics of P3HT in drop cast P3HT:PCBM films,” *Polymer*, vol. 113, pp. 200–213, Mar. 2017, doi: 10.1016/j.polymer.2017.01.067.

[39] F. C. Krebs, “Fabrication and processing of polymer solar cells: A review of printing and coating techniques,” *Sol. Energy Mater. Sol. Cells*, vol. 93, no. 4, pp. 394–412, Apr. 2009, doi: 10.1016/j.solmat.2008.10.004.

[40] N. J. Turro, J. C. Scaiano, and V. Ramamurthy, *Modern Molecular Photochemistry of Organic Molecules*, 1st edition. Sausalito, Calif: University Science Books, 2010.

[41] S. M. Menke and R. J. Holmes, “Exciton diffusion in organic photovoltaic cells,” *Energy Env. Sci*, vol. 7, no. 2, pp. 499–512, 2014, doi: 10.1039/C3EE42444H.

[42] O. V. Mikhnenko, P. W. M. Blom, and T.-Q. Nguyen, “Exciton diffusion in organic semiconductors,” *Energy Environ. Sci.*, vol. 8, no. 7, pp. 1867–1888, Jul. 2015, doi: 10.1039/C5EE00925A.

[43] J. D. A. Lin *et al.*, “Systematic study of exciton diffusion length in organic semiconductors by six experimental methods,” *Mater. Horiz.*, vol. 1, no. 2, pp. 280–285, Feb. 2014, doi: 10.1039/C3MH00089C.

[44] M.-H. Jao, H.-C. Liao, and W.-F. Su, “Achieving a high fill factor for organic solar cells,” *J. Mater. Chem. A*, vol. 4, no. 16, pp. 5784–5801, Apr. 2016, doi: 10.1039/C6TA00126B.

[45] B. Qi and J. Wang, “Fill factor in organic solar cells,” *Phys. Chem. Chem. Phys.*, vol. 15, no. 23, pp. 8972–8982, May 2013, doi: 10.1039/C3CP51383A.

[46] H.-C. Liao, C.-C. Ho, C.-Y. Chang, M.-H. Jao, S. B. Darling, and W.-F. Su, “Additives for morphology control in high-efficiency organic solar cells,” *Mater. Today*, vol. 16, no. 9, pp. 326–336, Sep. 2013, doi: 10.1016/j.mattod.2013.08.013.

[47] H.-S. Lee, H. Ahn, J. W. Jo, B. Kim, and H. J. Son, “Synergistic effects of solvent and polymer additives on solar cell performance and stability of small molecule bulk heterojunction solar cells,” *J. Mater. Chem. A*, vol. 4, no. 47, pp. 18383–18391, Nov. 2016, doi: 10.1039/C6TA08278E.

[48] Y. Liang *et al.*, “For the Bright Future—Bulk Heterojunction Polymer Solar Cells with Power Conversion Efficiency of 7.4%,” *Adv. Mater.*, vol. 22, no. 20, pp. E135–E138, 2010, doi: 10.1002/adma.200903528.

[49] L. Chang, H. W. A. Lademann, J.-B. Bonekamp, K. Meerholz, and A. J. Moulé, “Effect of Trace Solvent on the Morphology of P3HT:PCBM Bulk Heterojunction Solar Cells,” *Adv. Funct. Mater.*, vol. 21, no. 10, pp. 1779–1787, 2011, doi: 10.1002/adfm.201002372.

[50] A. Tournebize, A. Rivaton, H. Peisert, and T. Chassé, “The Crucial Role of Confined Residual Additives on the Photostability of P3HT:PCBM Active Layers,” *J. Phys. Chem. C*, vol. 119, no. 17, pp. 9142–9148, Apr. 2015, doi: 10.1021/acs.jpcc.5b01733.

[51] B. J. Tremolet de Villers *et al.*, “Removal of Residual Diiodooctane Improves Photostability of High-Performance Organic Solar Cell Polymers,” *Chem. Mater.*, vol. 28, no. 3, pp. 876–884, Feb. 2016, doi: 10.1021/acs.chemmater.5b04346.

[52] S. D. Oosterhout *et al.*, “Mixing Behavior in Small Molecule:Fullerene Organic Photovoltaics,” *Chem. Mater.*, vol. 29, no. 7, pp. 3062–3069, Apr. 2017, doi: 10.1021/acs.chemmater.7b00067.

[53] T. Coffey *et al.*, “Nanoscale characterization of squaraine-fullerene-based photovoltaic active layers by atomic force microscopy mechanical and electrical property mapping,” *Thin Solid Films*, vol. 669, pp. 120–132, Jan. 2019, doi: 10.1016/j.tsf.2018.10.046.

[54] T. Coffey *et al.*, “Nanoscale characterization of squaraine-fullerene-based photovoltaic active layers by atomic force microscopy mechanical and electrical property mapping,” *Thin Solid Films*, vol. 669, pp. 120–132, Jan. 2019, doi: 10.1016/j.tsf.2018.10.046.

[55] D. Galli *et al.*, “Suppressing the Surface Recombination and Tuning the Open-Circuit Voltage of Polymer/Fullerene Solar Cells by Implementing an Aggregative Ternary Compound,” *ACS Appl. Mater. Interfaces*, vol. 10, no. 34, pp. 28803–28811, Aug. 2018, doi: 10.1021/acsami.8b09174.

[56] Z. Cui *et al.*, “Seeing Down to the Bottom: Nondestructive Inspection of All-Polymer Solar Cells by Kelvin Probe Force Microscopy,” *Adv. Mater. Interfaces*, vol. 3, no. 18, p. 1600446, 2016, doi: https://doi.org/10.1002/admi.201600446.

[57] J. Hachmann *et al.*, “Lead candidates for high-performance organic photovoltaics from high-throughput quantum chemistry – the Harvard Clean Energy Project,” *Energy Environ. Sci.*, vol. 7, no. 2, pp. 698–704, Jan. 2014, doi: 10.1039/C3EE42756K.

[58] J. Hou, O. Inganäs, R. H. Friend, and F. Gao, “Organic solar cells based on non-fullerene acceptors,” *Nat. Mater.*, vol. 17, no. 2, pp. 119–128, Feb. 2018, doi: 10.1038/nmat5063.

[59] D. Hertel and H. Bässler, “Photoconduction in amorphous organic solids,” *Chemphyschem Eur. J. Chem. Phys. Phys. Chem.*, vol. 9, no. 5, pp. 666–688, Apr. 2008, doi: 10.1002/cphc.200700575.

[60] D. L. Dexter, “A Theory of Sensitized Luminescence in Solids,” *J. Chem. Phys.*, vol. 21, pp. 836–850, May 1953, doi: 10.1063/1.1699044.

[61] Th. Förster, “Zwischenmolekulare Energiewanderung und Fluoreszenz,” *Ann. Phys.*, vol. 437, no. 1–2, pp. 55–75, 1948, doi: 10.1002/andp.19484370105.

[62] L. G. Kaake, D. Moses, and A. J. Heeger, “Coherence and Uncertainty in Nanostructured Organic Photovoltaics,” *J. Phys. Chem. Lett.*, vol. 4, no. 14, pp. 2264–2268, Jul. 2013, doi: 10.1021/jz4010569.

[63] S. R. Forrest, “The Limits to Organic Photovoltaic Cell Efficiency,” *MRS Bull.*, vol. 30, no. 1, pp. 28–32, Jan. 2005, doi: 10.1557/mrs2005.5.

[64] T. Zhu, Y. Wan, and L. Huang, “Direct Imaging of Frenkel Exciton Transport by Ultrafast Microscopy,” *Acc. Chem. Res.*, vol. 50, no. 7, pp. 1725–1733, Jul. 2017, doi: 10.1021/acs.accounts.7b00155.

[65] Y.-J. Luo, Z.-Y. Lu, and Y. Huang, “Triplet fusion delayed fluorescence materials for OLEDs,” *Chin. Chem. Lett.*, vol. 27, no. 8, pp. 1223–1230, Aug. 2016, doi: 10.1016/j.cclet.2016.06.002.

[66] C. J. Bardeen, “The Structure and Dynamics of Molecular Excitons,” *Annu. Rev. Phys. Chem.*, vol. 65, no. 1, pp. 127–148, 2014, doi: 10.1146/annurev-physchem-040513-103654.

[67] O. V. Mikhnenko, P. W. M. Blom, and T.-Q. Nguyen, “Exciton diffusion in organic semiconductors,” *Energy Environ. Sci.*, vol. 8, no. 7, pp. 1867–1888, Jul. 2015, doi: 10.1039/C5EE00925A.

[68] C. Zheng *et al.*, “Measurement and Theoretical Interpretation of Exciton Diffusion as a Function of Intermolecular Separation for Squaraines Targeted for Bulk Heterojunction Solar Cells,” *J. Phys. Chem. C*, p. acs.jpcc.9b11816, Feb. 2020, doi: 10.1021/acs.jpcc.9b11816.

[69] J. Wang, H. Yao, Y. Xu, L. Ma, and J. Hou, “Recent progress in reducing voltage loss in organic photovoltaic cells,” *Mater. Chem. Front.*, vol. 5, no. 2, pp. 709–722, Jan. 2021, doi: 10.1039/D0QM00581A.

[70] C. Deibel and V. Dyakonov, “Polymer–fullerene bulk heterojunction solar cells,” *Rep. Prog. Phys.*, vol. 73, no. 9, p. 096401, Sep. 2010, doi: 10.1088/0034-4885/73/9/096401.

[71] R. S. Gurney, D. G. Lidzey, and T. Wang, “A review of non-fullerene polymer solar cells: from device physics to morphology control,” *Rep. Prog. Phys.*, vol. 82, no. 3, p. 036601, Feb. 2019, doi: 10.1088/1361-6633/ab0530.

[72] R. Ganesamoorthy, G. Sathiyan, and P. Sakthivel, “Review: Fullerene based acceptors for efficient bulk heterojunction organic solar cell applications,” *Sol. Energy Mater. Sol. Cells*, vol. 161, pp. 102–148, Mar. 2017, doi: 10.1016/j.solmat.2016.11.024.

[73] N. Tessler, Y. Preezant, N. Rappaport, and Y. Roichman, “Charge Transport in Disordered Organic Materials and Its Relevance to Thin-Film Devices: A Tutorial Review,” *Adv. Mater.*, vol. 21, no. 27, pp. 2741–2761, 2009, doi: 10.1002/adma.200803541.

[74] N. Karl, “Charge carrier transport in organic semiconductors,” *Synth. Met.*, vol. 133–134, pp. 649–657, Mar. 2003, doi: 10.1016/S0379-6779(02)00398-3.

[75] H. Xu, F. Yuan, D. Zhou, X. Liao, L. Chen, and Y. Chen, “Hole transport layers for organic solar cells: recent progress and prospects,” *J. Mater. Chem. A*, vol. 8, no. 23, pp. 11478–11492, Jun. 2020, doi: 10.1039/D0TA03511D.

[76] C. Anrango-Camacho, K. Pavón-Ipiales, B. A. Frontana-Uribe, and A. Palma-Cando, "Recent Advances in Hole-Transporting Layers for Organic Solar Cells," *Nanomaterials*, vol. 12, no. 3, p. 443, Jan. 2022, doi: 10.3390/nano12030443.

[77] Q. Van Le, J.-Y. Choi, and S. Y. Kim, "Recent advances in the application of two-dimensional materials as charge transport layers in organic and perovskite solar cells," *FlatChem*, vol. 2, pp. 54–66, Apr. 2017, doi: 10.1016/j.flatc.2017.04.002.

[78] D. Baran *et al.*, "Reducing the efficiency–stability–cost gap of organic photovoltaics with highly efficient and stable small molecule acceptor ternary solar cells," *Nat. Mater.*, vol. 16, no. 3, pp. 363–369, Mar. 2017, doi: 10.1038/nmat4797.

[79] N. E. Jackson, B. M. Savoie, T. J. Marks, L. X. Chen, and M. A. Ratner, "The Next Breakthrough for Organic Photovoltaics?," *J. Phys. Chem. Lett.*, vol. 6, no. 1, pp. 77–84, Jan. 2015, doi: 10.1021/jz502223t.

[80] G. Griffini *et al.*, "Long-Term Thermal Stability of High-Efficiency Polymer Solar Cells Based on Photocrosslinkable Donor-Acceptor Conjugated Polymers," *Adv. Mater.*, vol. 23, no. 14, pp. 1660–1664, 2011, doi: https://doi.org/10.1002/adma.201004743.

[81] J. W. Rumer and I. McCulloch, "Organic photovoltaics: Crosslinking for optimal morphology and stability," *Mater. Today*, vol. 18, no. 8, pp. 425–435, Oct. 2015, doi: 10.1016/j.mattod.2015.04.001.

[82] F.-J. Kahle, C. Saller, A. Köhler, and P. Strohriegl, "Crosslinked Semiconductor Polymers for Photovoltaic Applications," *Adv. Energy Mater.*, vol. 7, no. 16, p. 1700306, 2017, doi: https://doi.org/10.1002/aenm.201700306.

[83] T. Ameri, P. Khoram, J. Min, and C. J. Brabec, "Organic Ternary Solar Cells: A Review," *Adv. Mater.*, vol. 25, no. 31, pp. 4245–4266, 2013, doi: 10.1002/adma.201300623.

[84] C. Zheng *et al.*, "Impact of Alkyl Chain Length on Small Molecule Crystallization and Nanomorphology in Squaraine-Based Solution Processed Solar Cells," *J. Phys. Chem. C*, vol. 121, no. 14, pp. 7750–7760, Apr. 2017, doi: 10.1021/acs.jpcc.7b01339.

[85] C. Zheng *et al.*, "Contribution of Aggregate States and Energetic Disorder to a Squaraine System Targeted for Organic Photovoltaic Devices," *Langmuir*, vol. 31, no. 28, pp. 7717–7726, Jul. 2015, doi: 10.1021/acs.langmuir.5b01045.

[86] N. J. Hestand and F. C. Spano, "Expanded Theory of H- and J-Molecular Aggregates: The Effects of Vibronic Coupling and Intermolecular Charge Transfer," *Chem. Rev.*, vol. 118, no. 15, pp. 7069–7163, Aug. 2018, doi: 10.1021/acs.chemrev.7b00581.

[87] F. C. Spano, "The Spectral Signatures of Frenkel Polarons in H- and J-Aggregates," *Acc. Chem. Res.*, vol. 43, no. 3, pp. 429–439, Mar. 2010, doi: 10.1021/ar900233v.

[88] M. Kasha, H. R. Rawls, and E.-B. M. Ashraf, "The exciton model in molecular spectroscopy," *Pure Appl. Chem.*, vol. 11, no. 3–4, pp. 371–392, 1965, doi: 10.1351/pac196511030371.

[89] M. Más-Montoya and R. A. J. Janssen, “The Effect of H- and J-Aggregation on the Photophysical and Photovoltaic Properties of Small Thiophene–Pyridine–DPP Molecules for Bulk-Heterojunction Solar Cells,” *Adv. Funct. Mater.*, vol. 27, no. 16, p. 1605779, 2017, doi: 10.1002/adfm.201605779.

[90] N. J. Hestand *et al.*, “Confirmation of the Origins of Panchromatic Spectra in Squaraine Thin Films Targeted for Organic Photovoltaic Devices,” *J. Phys. Chem. C*, vol. 119, no. 33, pp. 18964–18974, Aug. 2015, doi: 10.1021/acs.jpcc.5b05095.

[91] C. Zheng, C. Zhong, C. J. Collison, and F. C. Spano, “Non-Kasha Behavior in Quadrupolar Dye Aggregates: The Red-Shifted H-Aggregate,” *J. Phys. Chem. C*, vol. 123, no. 5, pp. 3203–3215, Feb. 2019, doi: 10.1021/acs.jpcc.8b11416.

[92] K. M. Shafeekh, S. Das, C. Sissa, and A. Painelli, “Asymmetric Squaraine Dyes: Spectroscopic and Theoretical Investigation,” *J. Phys. Chem. B*, vol. 117, no. 28, pp. 8536–8546, Jul. 2013, doi: 10.1021/jp401099g.

[93] C. Sissa *et al.*, “Dimers of Quadrupolar Chromophores in Solution: Electrostatic Interactions and Optical Spectra,” *J. Phys. Chem. B*, vol. 114, no. 2, pp. 882–893, Jan. 2010, doi: 10.1021/jp909475d.

[94] F. Terenziani and A. Painelli, “Supramolecular interactions in clusters of polar and polarizable molecules,” *Phys. Rev. B*, vol. 68, no. 16, p. 165405, Oct. 2003, doi: 10.1103/PhysRevB.68.165405.

[95] F. Terenziani and A. Painelli, “Collective and cooperative phenomena in molecular materials: dimers of polar chromophores,” *J. Lumin.*, vol. 112, no. 1, pp. 474–478, Apr. 2005, doi: 10.1016/j.jlumin.2004.09.079.

[96] F. Terenziani, A. Painelli, C. Katan, M. Charlot, and M. Blanchard-Desce, “Charge Instability in Quadrupolar Chromophores: Symmetry Breaking and Solvatochromism,” *J. Am. Chem. Soc.*, vol. 128, no. 49, pp. 15742–15755, Dec. 2006, doi: 10.1021/ja064521j.

[97] A. Olaya-Castro, A. Nazir, and G. R. Fleming, “Quantum-coherent energy transfer: implications for biology and new energy technologies,” *Philos. Transact. A Math. Phys. Eng. Sci.*, vol. 370, no. 1972, pp. 3613–3617, Aug. 2012, doi: 10.1098/rsta.2012.0192.

[98] M. Kasha, “Energy Transfer Mechanisms and the Molecular Exciton Model for Molecular Aggregates,” *Radiat. Res.*, vol. 20, no. 1, pp. 55–70, 1963, doi: 10.2307/3571331.

[99] A. A. Mohapatra, V. Tiwari, and S. Patil, “Energy transfer in ternary blend organic solar cells: recent insights and future directions,” *Energy Environ. Sci.*, vol. 14, no. 1, pp. 302–319, Jan. 2021, doi: 10.1039/D0EE03170D.

[100] S. Athanasopoulos, H. Bässler, and A. Köhler, “Disorder vs Delocalization: Which Is More Advantageous for High-Efficiency Organic Solar Cells?,” *J. Phys. Chem. Lett.*, vol. 10, no. 22, pp. 7107–7112, Nov. 2019, doi: 10.1021/acs.jpclett.9b02866.

[101] S. Athanasopoulos, E. V. Emelianova, A. B. Walker, and D. Beljonne, “Exciton diffusion in energetically disordered organic materials,” *Phys. Rev. B*, vol. 80, no. 19, p. 195209, Nov. 2009, doi: 10.1103/PhysRevB.80.195209.

[102] O. V. Mikhnenko, F. Cordella, A. B. Sieval, J. C. Hummelen, P. W. M. Blom, and M. A. Loi, “Temperature Dependence of Exciton Diffusion in Conjugated Polymers,” *J. Phys. Chem. B*, vol. 112, no. 37, pp. 11601–11604, Sep. 2008, doi: 10.1021/jp8042363.

[103] G. J. Hedley, A. Ruseckas, and I. D. W. Samuel, “Light Harvesting for Organic Photovoltaics,” *Chem. Rev.*, vol. 117, no. 2, pp. 796–837, Jan. 2017, doi: 10.1021/acs.chemrev.6b00215.

[104] B. Movaghar, M. Grünewald, B. Ries, H. Bassler, and D. Würtz, “Diffusion and relaxation of energy in disordered organic and inorganic materials,” *Phys. Rev. B*, vol. 33, no. 8, pp. 5545–5554, Apr. 1986, doi: 10.1103/PhysRevB.33.5545.

[105] S. Wang *et al.*, “High efficiency organic photovoltaic cells based on a vapor deposited squaraine donor,” *Appl. Phys. Lett.*, vol. 94, no. 23, p. 233304, Jun. 2009, doi: 10.1063/1.3152011.

[106] C. Zheng *et al.*, “Phase separation, crystallinity and monomer-aggregate population control in solution processed small molecule solar cells,” *Sol. Energy Mater. Sol. Cells*, vol. 157, pp. 366–376, Dec. 2016, doi: 10.1016/j.solmat.2016.05.060.

[107] R. Bernhardt *et al.*, “Structural Disorder as the Origin of Optical Properties and Spectral Dynamics in Squaraine Nano-Aggregates,” *J. Am. Chem. Soc.*, vol. 144, no. 42, pp. 19372–19381, Oct. 2022, doi: 10.1021/jacs.2c07064.

[108] R. Xue, J. Zhang, Y. Li, and Y. Li, “Organic Solar Cell Materials toward Commercialization,” *Small*, vol. 14, no. 41, p. 1801793, 2018, doi: https://doi.org/10.1002/smll.201801793.

[109] N. Li, I. McCulloch, and C. J. Brabec, “Analyzing the efficiency, stability and cost potential for fullerene-free organic photovoltaics in one figure of merit,” *Energy Environ. Sci.*, vol. 11, no. 6, pp. 1355–1361, Jun. 2018, doi: 10.1039/C8EE00151K.

[110] F. Zhao, C. Wang, and X. Zhan, “Morphology Control in Organic Solar Cells,” *Adv. Energy Mater.*, vol. 8, no. 28, p. 1703147, 2018, doi: 10.1002/aenm.201703147.

[111] C. W. Dirk *et al.*, “Squarylium Dyes: Structural Factors Pertaining to the Negative Third-Order Nonlinear Optical Response,” *J. Am. Chem. Soc.*, vol. 117, no. 8, pp. 2214–2225, Mar. 1995, doi: 10.1021/ja00113a011.

[112] G. Chen, H. Sasabe, T. Igarashi, Z. Hong, and J. Kido, “Squaraine dyes for organic photovoltaic cells,” *J. Mater. Chem. A*, vol. 3, no. 28, pp. 14517–14534, Jul. 2015, doi: 10.1039/C5TA01879J.

[113] R. W. Bigelow and H.-J. Freund, “An MNDO and CNDO / S(S + DES CI) study on the structural and electronic properties of a model squaraine dye and related cyanine,”

*Chem. Phys.*, vol. 107, no. 2, pp. 159–174, Sep. 1986, doi: 10.1016/0301-0104(86)85001-7.

[114] J. Heier, R. Steiger, F. Nüesch, and R. Hany, "Fast Assembly of Cyanine Dyes into Aggregates onto [6,6]-Phenyl C61-Butyric Acid Methyl Ester Surfaces from Organic Solvents," *Langmuir*, vol. 26, no. 6, pp. 3955–3961, Mar. 2010, doi: 10.1021/la903313k.

[115] G. Cerullo, M. Nisoli, S. Stagira, and S. De Silvestri, "Sub-8-fs pulses from an ultrabroadband optical parametric amplifier in the visible," *Opt. Lett.*, vol. 23, no. 16, pp. 1283–1285, Aug. 1998, doi: 10.1364/ol.23.001283.

[116] G. Cerullo and S. Silvestri, "Ultrafast optical parametric amplifiers. Rev. Sci. Instrum. 74, 1-18," *Rev. Sci. Instrum.*, vol. 74, pp. 1–18, Jan. 2003, doi: 10.1063/1.1523642.

[117] R. Trebino *et al.*, "Measuring ultrashort laser pulses in the time-frequency domain using frequency-resolved optical gating," *Rev. Sci. Instrum.*, vol. 68, no. 9, pp. 3277–3295, Sep. 1997, doi: 10.1063/1.1148286.

[118] K. M. Pelzer and S. B. Darling, "Charge generation in organic photovoltaics: a review of theory and computation," *Mol. Syst. Des. Eng.*, vol. 1, no. 1, pp. 10–24, Jun. 2016, doi: 10.1039/C6ME00005C.

[119] L. Ye, B. A. Collins, X. Jiao, J. Zhao, H. Yan, and H. Ade, "Miscibility–Function Relations in Organic Solar Cells: Significance of Optimal Miscibility in Relation to Percolation," *Adv. Energy Mater.*, vol. 8, no. 28, p. 1703058, 2018, doi: 10.1002/aenm.201703058.

[120] T. Wiegand, J. Godoy, S. Gupta, J. Cody, T. Coffey, and C.-J. Collison, "Optimal morphology, H-aggregation, and ternary blend excited state disruption in equilibrated squaraine-based all small molecule solar-cells.," *Thin Solid Films*, p. 139623, Dec. 2022, doi: 10.1016/j.tsf.2022.139623.

[121] L. Ye *et al.*, "High-Efficiency Nonfullerene Organic Solar Cells: Critical Factors that Affect Complex Multi-Length Scale Morphology and Device Performance," *Adv. Energy Mater.*, vol. 7, no. 7, p. 1602000, 2017, doi: 10.1002/aenm.201602000.

[122] D. R. Kozub, K. Vakhshouri, L. M. Orme, C. Wang, A. Hexemer, and E. D. Gomez, "Polymer Crystallization of Partially Miscible Polythiophene/Fullerene Mixtures Controls Morphology," *Macromolecules*, vol. 44, no. 14, pp. 5722–5726, Jul. 2011, doi: 10.1021/ma200855r.

[123] C. Müller *et al.*, "Binary Organic Photovoltaic Blends: A Simple Rationale for Optimum Compositions," *Adv. Mater.*, vol. 20, no. 18, pp. 3510–3515, Sep. 2008, doi: 10.1002/adma.200800963.

[124] H. Gaspar, F. Figueira, L. Pereira, A. Mendes, J. C. Viana, and G. Bernardo, "Recent Developments in the Optimization of the Bulk Heterojunction Morphology of Polymer: Fullerene Solar Cells," *Materials*, vol. 11, no. 12, p. 2560, Dec. 2018, doi: 10.3390/ma11122560.

[125] T. M. Burke and M. D. McGehee, “How High Local Charge Carrier Mobility and an Energy Cascade in a Three-Phase Bulk Heterojunction Enable >90% Quantum Efficiency,” *Adv. Mater.*, vol. 26, no. 12, pp. 1923–1928, 2014, doi: 10.1002/adma.201304241.

[126] C. J. Collison, L. J. Rothberg, V. Treemaneekarn, and Y. Li, “Conformational Effects on the Photophysics of Conjugated Polymers: A Two Species Model for MEH−PPV Spectroscopy and Dynamics,” *Macromolecules*, vol. 34, no. 7, pp. 2346–2352, Mar. 2001, doi: 10.1021/ma001354d.

[127] C. J. Collison, M. J. O’Donnell, and J. L. Alexander, “Complexation between Rhodamine 101 and Single-Walled Carbon Nanotubes Indicative of Solvent−Nanotube Interaction Strength,” *J Phys Chem C*, vol. 112, no. 39, pp. 15144–15150, 2008, doi: 10.1021/jp804359j.

[128] J. Wu *et al.*, “Tail state limited photocurrent collection of thick photoactive layers in organic solar cells,” *Nat. Commun.*, vol. 10, no. 1, Art. no. 1, Nov. 2019, doi: 10.1038/s41467-019-12951-7.

[129] J. R. Tumbleston, Y. Liu, E. T. Samulski, and R. Lopez, “Interplay between Bimolecular Recombination and Carrier Transport Distances in Bulk Heterojunction Organic Solar Cells,” *Adv. Energy Mater.*, vol. 2, no. 4, pp. 477–486, 2012, doi: 10.1002/aenm.201100677.

[130] D. Bartesaghi *et al.*, “Competition between recombination and extraction of free charges determines the fill factor of organic solar cells,” *Nat. Commun.*, vol. 6, no. 1, Art. no. 1, May 2015, doi: 10.1038/ncomms8083.

[131] R. C. Hilborn, “Einstein coefficients, cross sections, f values, dipole moments, and all that,” *Am. J. Phys.*, vol. 50, no. 11, pp. 982–986, Nov. 1982, doi: 10.1119/1.12937.

[132] H. A. Benesi and J. H. Hildebrand, “A Spectrophotometric Investigation of the Interaction of Iodine with Aromatic Hydrocarbons,” *J. Am. Chem. Soc.*, vol. 71, no. 8, pp. 2703–2707, Aug. 1949, doi: 10.1021/ja01176a030.

[133] G. Paternò *et al.*, “Micro-focused X-ray diffraction characterization of high-quality [6,6]-phenyl-C61-butyric acid methyl ester single crystals without solvent impurities,” *J. Mater. Chem. C*, vol. 1, no. 36, pp. 5619–5623, Aug. 2013, doi: 10.1039/C3TC31075B.

[134] Y. Sun, Y. Han, and J. Liu, “Controlling PCBM aggregation in P3HT/PCBM film by a selective solvent vapor annealing,” *Chin. Sci. Bull.*, vol. 58, no. 22, pp. 2767–2774, Aug. 2013, doi: 10.1007/s11434-013-5944-6.

[135] O. G. Reid *et al.*, “The influence of solid-state microstructure on the origin and yield of long-lived photogenerated charge in neat semiconducting polymers,” *J. Polym. Sci. Part B Polym. Phys.*, vol. 50, no. 1, pp. 27–37, 2012, doi: https://doi.org/10.1002/polb.22379.

[136] S. B. Darling and F. You, “The case for organic photovoltaics,” *RSC Adv.*, vol. 3, no. 39, pp. 17633–17648, Sep. 2013, doi: 10.1039/C3RA42989J.

[137] Y. Cui, L. Hong, and J. Hou, “Organic Photovoltaic Cells for Indoor Applications: Opportunities and Challenges,” *ACS Appl. Mater. Interfaces*, vol. 12, no. 35, pp. 38815–38828, Sep. 2020, doi: 10.1021/acsami.0c10444.

[138] W. Peng *et al.*, “Over 18% ternary polymer solar cells enabled by a terpolymer as the third component,” *Nano Energy*, vol. 92, p. 106681, Feb. 2022, doi: 10.1016/j.nanoen.2021.106681.

[139] F. Liu *et al.*, “Organic Solar Cells with 18% Efficiency Enabled by an Alloy Acceptor: A Two-in-One Strategy,” *Adv. Mater.*, vol. 33, no. 27, p. 2100830, 2021, doi: 10.1002/adma.202100830.

[140] L. Zhu *et al.*, “Single-junction organic solar cells with over 19% efficiency enabled by a refined double-fibril network morphology,” *Nat. Mater.*, vol. 21, no. 6, Art. no. 6, Jun. 2022, doi: 10.1038/s41563-022-01244-y.

[141] H. Tang *et al.*, “Donor Derivative Incorporation: An Effective Strategy toward High Performance All-Small-Molecule Ternary Organic Solar Cells,” *Adv. Sci.*, vol. 6, no. 21, p. 1901613, 2019, doi: 10.1002/advs.201901613.

[142] J. Razzell-Hollis, S. Limbu, and J.-S. Kim, “Spectroscopic Investigations of Three-Phase Morphology Evolution in Polymer: Fullerene Solar Cell Blends,” *J. Phys. Chem. C*, vol. 120, no. 20, pp. 10806–10814, May 2016, doi: 10.1021/acs.jpcc.6b02898.

[143] Q. Burlingame, M. Ball, and Y.-L. Loo, “It’s time to focus on organic solar cell stability,” *Nat. Energy*, vol. 5, no. 12, Art. no. 12, Dec. 2020, doi: 10.1038/s41560-020-00732-2.

[144] R. Zhou *et al.*, “All-small-molecule organic solar cells with over 14% efficiency by optimizing hierarchical morphologies,” *Nat. Commun.*, vol. 10, no. 1, pp. 1–9, Nov. 2019, doi: 10.1038/s41467-019-13292-1.

[145] D. Hu *et al.*, “14.7% all-small-molecule organic solar cells enabled by fullerene derivative incorporation,” *Sustain. Energy Fuels*, vol. 5, no. 14, pp. 3593–3597, Jul. 2021, doi: 10.1039/D1SE00501D.

[146] T. Wiegand *et al.*, “Quantifying Squaraine Phase Separation, Aggregate Populations, and Solar Cell Performance with a Correlated Multimethod Approach,” *J. Phys. Chem. C*, vol. 126, no. 35, pp. 14791–14800, Sep. 2022, doi: 10.1021/acs.jpcc.2c01286.

[147] T. Ameri, P. Khoram, J. Min, and C. J. Brabec, “Organic Ternary Solar Cells: A Review,” *Adv. Mater.*, vol. 25, no. 31, pp. 4245–4266, 2013, doi: 10.1002/adma.201300623.

[148] L. Lu, M. A. Kelly, W. You, and L. Yu, “Status and prospects for ternary organic photovoltaics,” *Nat. Photonics*, vol. 9, no. 8, Art. no. 8, Aug. 2015, doi: 10.1038/nphoton.2015.128.

[149] B. M. Savoie, S. Dunaisky, T. J. Marks, and M. A. Ratner, “The Scope and Limitations of Ternary Blend Organic Photovoltaics,” *Adv. Energy Mater.*, vol. 5, no. 3, p. 1400891, 2015, doi: 10.1002/aenm.201400891.

[150] Y. Cai *et al.*, "A Well-Mixed Phase Formed by Two Compatible Non-Fullerene Acceptors Enables Ternary Organic Solar Cells with Efficiency over 18.6%," *Adv. Mater.*, vol. 33, no. 33, p. 2101733, 2021, doi: 10.1002/adma.202101733.

[151] M. Nam *et al.*, "Ternary blend organic solar cells with improved morphological stability," *J. Mater. Chem. A*, vol. 7, no. 16, pp. 9698–9707, 2019, doi: 10.1039/C9TA00382G.

[152] J. Zhang *et al.*, "Conjugated Polymer–Small Molecule Alloy Leads to High Efficient Ternary Organic Solar Cells," *J. Am. Chem. Soc.*, vol. 137, no. 25, pp. 8176–8183, Jul. 2015, doi: 10.1021/jacs.5b03449.

[153] H. Liang *et al.*, "15.8% efficiency all-small-molecule solar cells enabled by a combination of side-chain engineering and polymer additive," *J. Mater. Chem. A*, vol. 10, no. 20, pp. 10926–10934, May 2022, doi: 10.1039/D2TA01690G.

[154] Y. Wang *et al.*, "Ternary-organic photovoltaics with J71 as donor and two compatible nonfullerene acceptors," *J. Polym. Sci.*, vol. n/a, no. n/a, doi: 10.1002/pol.20210118.

[155] L. Duan and A. Uddin, "Progress in Stability of Organic Solar Cells," *Adv. Sci.*, vol. 7, no. 11, p. 1903259, 2020, doi: 10.1002/advs.201903259.

[156] N. Li *et al.*, "Abnormal strong burn-in degradation of highly efficient polymer solar cells caused by spinodal donor-acceptor demixing," *Nat. Commun.*, vol. 8, p. 14541, Feb. 2017, doi: 10.1038/ncomms14541.

[157] S. Li *et al.*, "A spirobifluorene and diketopyrrolopyrrole moieties based non-fullerene acceptor for efficient and thermally stable polymer solar cells with high open-circuit voltage," *Energy Environ. Sci.*, vol. 9, no. 2, pp. 604–610, Feb. 2016, doi: 10.1039/C5EE03481G.

[158] K. Zhou, J. Xin, and W. Ma, "Hierarchical Morphology Stability under Multiple Stresses in Organic Solar Cells," *ACS Energy Lett.*, vol. 4, no. 2, pp. 447–455, Feb. 2019, doi: 10.1021/acsenergylett.8b02383.

[159] M. Jørgensen, K. Norrman, S. A. Gevorgyan, T. Tromholt, B. Andreasen, and F. C. Krebs, "Stability of Polymer Solar Cells," *Adv. Mater.*, vol. 24, no. 5, pp. 580–612, 2012, doi: 10.1002/adma.201104187.

[160] C. Lindqvist *et al.*, "Nucleation-limited fullerene crystallisation in a polymer–fullerene bulk-heterojunction blend," *J. Mater. Chem. A*, vol. 1, no. 24, pp. 7174–7180, May 2013, doi: 10.1039/C3TA11018D.

[161] H. Ohkita and S. Ito, "Transient absorption spectroscopy of polymer-based thin-film solar cells," *Polymer*, vol. 52, no. 20, pp. 4397–4417, Sep. 2011, doi: 10.1016/j.polymer.2011.06.061.

[162] C. Franchini, M. Reticcioli, M. Setvin, and U. Diebold, "Polarons in materials," *Nat. Rev. Mater.*, vol. 6, no. 7, Art. no. 7, Jul. 2021, doi: 10.1038/s41578-021-00289-w.

[163] C. Ruckebusch, M. Sliwa, P. Pernot, A. de Juan, and R. Tauler, “Comprehensive data analysis of femtosecond transient absorption spectra: A review,” *J. Photochem. Photobiol. C Photochem. Rev.*, vol. 13, no. 1, pp. 1–27, Mar. 2012, doi: 10.1016/j.jphotochemrev.2011.10.002.

[164] J. R. Lakowicz, Ed., “Fluorescence Anisotropy,” in *Principles of Fluorescence Spectroscopy*, Boston, MA: Springer US, 2006, pp. 353–382. doi: 10.1007/978-0-387-46312-4_10.

[165] G. M. Somashekharappa, M. Paul, C. Govind, R. Mathew, and V. Karunakaran, “Ultrafast Intermolecular Interaction Dynamics between NIR-Absorbing Unsymmetrical Squaraines and PCBM: Effects of Halogen Substitution,” *J. Phys. Chem. B*, vol. 126, no. 24, pp. 4509–4519, Jun. 2022, doi: 10.1021/acs.jpcb.1c10840.

[166] T. Goh *et al.*, “Coevaporated Bisquaraine Inverted Solar Cells: Enhancement Due to Energy Transfer and Open Circuit Voltage Control,” *ACS Photonics*, vol. 2, no. 1, pp. 86–95, Jan. 2015, doi: 10.1021/ph500282z.

[167] G. de Miguel *et al.*, “Photophysics of H- and J-Aggregates of Indole-Based Squaraines in Solid State,” *J. Phys. Chem. C*, vol. 116, no. 17, pp. 9379–9389, May 2012, doi: 10.1021/jp210281z.

[168] M. Kasha, H. Rawls, and M. El-Bayoumi, “The exciton model in molecular spectroscopy, Pure Appl. Chem.11, 371-392,” *Pure Appl. Chem. - PURE APPL CHEM*, vol. 11, pp. 371–392, Jan. 1965, doi: 10.1351/pac196511030371.

[169] C. Keiderling, S. Dimitrov, and J. R. Durrant, “Exciton and Charge Generation in PC60BM Thin Films,” *J. Phys. Chem. C*, vol. 121, no. 27, pp. 14470–14475, Jul. 2017, doi: 10.1021/acs.jpcc.7b03962.

[170] D. M. Guldi and M. Prato, “Excited-State Properties of C60 Fullerene Derivatives,” *Acc. Chem. Res.*, vol. 33, no. 10, pp. 695–703, Oct. 2000, doi: 10.1021/ar990144m.

[171] S. D. Dimitrov *et al.*, “Spectroscopic Investigation of the Effect of Microstructure and Energetic Offset on the Nature of Interfacial Charge Transfer States in Polymer: Fullerene Blends,” *J. Am. Chem. Soc.*, vol. 141, no. 11, pp. 4634–4643, Mar. 2019, doi: 10.1021/jacs.8b11484.

# 8 Appendix

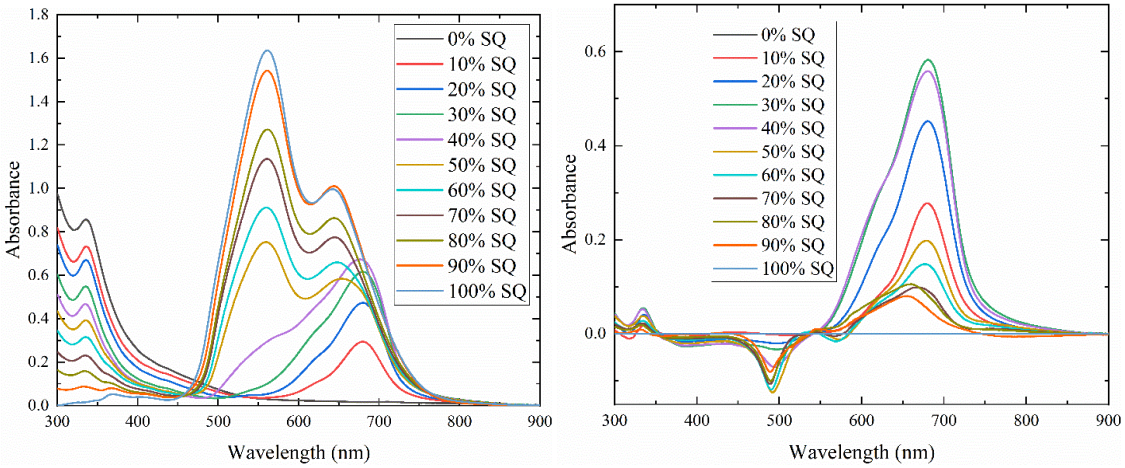


**Figure A8.1 – (left)Spectra of annealed $DBSQ(OH)_2$ film absorbance where percentages represent targeted SQ weight% values, with the remaining percentage made up by $PC_{60}BM$. (right) The spectra that remain after subtraction of the PCBM contribution and a 100% $DBSQ(OH)_2$ spectrum for the 90°C 5 minute anneal film multiplied by a coefficient. The subtraction was made such that the new baseline values summed to zero over six different ranges, 550-570 nm, 540-570 nm, 530-570 nm, 520-560 nm, 500-560 nm, 480-560 nm. The subtraction coefficient for all these cases was then averaged, which considers that a larger range provides greater accuracy for smaller SQ weight percent films, and a smaller range provides greater accuracy for larger SQ weight percent films. The errors provided in Table A8.1 provide the truest depiction of uncertainty for all blend ratios.**

**Table A8.1 - The relative contributions of the HCT state for each 90°C annealed squaraine film.**

| Wt% SQ | Contribution of HCT[a]. (Standard Deviation) [Spectral Subtraction Coefficient] | % of SQ that is HCT[b]. [Zero Baseline] | Area of fitted peak divided by 100% HCT area[c] | % of SQ that is HCT[d]. [Gaussian Fit] |
|---|---|---|---|---|
| 0 | 0 | 0 | | |
| 10 | 0.0056 (0.0013) | 5.6 ± 1.3 | | |
| 20 | 0.0138 (0.0060) | 7 ± 3 | | |
| 30 | 0.0376 (0.0120) | 13 ± 4 | | |
| 40 | 0.1528 (0.0180) | 38 ± 5 | | |
| 50 | 0.4452 (0.0166) | 89 ± 4 | 0.424 | 84.9 |
| 60 | 0.5489 (0.0128) | 92 ± 4 | 0.532 | 88.7 |
| 70 | 0.6865 (0.0112) | 98 ± 4 | 0.675 | 96.4 |
| 80 | 0.7634 (0.0145) | 95 ± 4 | 0.746 | 93.3 |
| 90 | 0.9336 (0.0120) | 104 ± 4 | 0.916 | 102 |
| 100 | 1 (0) | 100 | 1 | 100 |

[a] Average Raw coefficient (wavelength ranges 550-570nm, 540-570 nm, 530-570 nm, 520-560 nm, 500-560 nm, 480-560 nm) multiplied by the 100% SQ, 90°C annealed spectrum (defined to be HCT only), and subtracted. Provides an average baseline of zero over the wavelength range stated. (Standard deviation is calculated from the averages over the six wavelength ranges stated)

[b] Fraction of SQ that is HCT is calculated by dividing the Average Raw coefficient by the blend ratio fraction of SQ in the associated film, thereby normalizing the coefficient to yield a per SQ weight percent value. Percent error is obtained by dividing the standard deviation from the averages over all six wavelength ranges by that average, and by compounding that error with the 3.2% uncertainty in blend ratio. Blend ratio uncertainty was determined for 16 films with varying SQ:PCBM blend ratio. After comparing the target blend ratio with the actual amount of each material on the film, as measured by dissolving off the film into a known volume of chloroform and back-calculating the mass from molar absorptivity, we determined the average error to be 3.2%.

[c] Area obtained from fitting for the high energy annealed peak divided by that for the 100% SQ annealed film.

[d] Fraction of SQ that is HCT: Area of Gaussian peak fit divided by 100% SQ Gaussian peak fit, subsequently divided by the fraction of SQ in the sample. This is done because as the concentration of SQ increases we must account for the associated increase in absorbance, according to the Beer Lambert Law.

**Table A8.2 – Gaussian peak fitting parameters of unannealed films**

| Wt% SQ | High Energy Peak Posn. | Width | Area | Low Energy Peak Posn. | Width | Area |
|---|---|---|---|---|---|---|
| 10 | 667.5 | 139.34 | 19.65 | 679.25 | 48.18 | 9 |
| 20 | 657.73 | 126.97 | 39.56 | 681.8 | 46.19 | 10.98 |
| 30 | 611.04 | 92.74 | 29.22 | 681.45 | 75.98 | 45 |
| 40 | 607.01 | 93.27 | 45.92 | 681.28 | 75.31 | 56.61 |
| 50 | 605.9 | 96.35 | 67.3 | 681.9 | 74.07 | 67.38 |
| 60 | 605.29 | 98.28 | 83.13 | 682.39 | 73.6 | 74.64 |
| 70 | 603.93 | 101.38 | 106.6 | 682.34 | 72.95 | 82.68 |
| 80 | 600.84 | 102.66 | 120.46 | 681.31 | 74 | 88.78 |
| 90 | 596.31 | 107.31 | 146.8 | 679.92 | 76.54 | 97.71 |
| 100 | 591.34 | 111.96 | 165.92 | 678.27 | 79.72 | 102.6 |

**Table A8.3 - Gaussian peak fitting parameters of 50°C Annealed Films**

| Wt% SQ | High Energy Peak Posn. | Width | Area | Low Energy Peak Posn. | Width | Area |
|---|---|---|---|---|---|---|
| 0 | | | | | | |
| 10 | 670.19 | 137.9 | 17.26 | 679.1 | 48.54 | 8.743 |
| 20 | 659.83 | 126.6 | 36.12 | 681.8 | 46.41 | 10.36 |
| 30 | 650.12 | 131.8 | 62.27 | 684.3 | 46.39 | 13.28 |
| 40 | 608.12 | 93.31 | 44.24 | 681.8 | 75.08 | 55.53 |
| 50 | 607.65 | 97.42 | 65.61 | 682.66 | 72.92 | 63.85 |
| 60 | 606.28 | 98.19 | 80.09 | 682.62 | 73.21 | 72.97 |
| 70 | 606.22 | 103.44 | 109.16 | 683.3 | 70.83 | 78.79 |
| 80 | 601.01 | 106.89 | 118.3 | 681.5 | 73.24 | 80.61 |
| 90 | 554.44 | 83.73 | 116.86 | 650.18 | 101.91 | 97.31 |
| 100 | 552.51 | 85.96 | 136.89 | 650.64 | 102.01 | 97.78 |

**Table A8.4 - Gaussian peak fitting parameters of 90°C Annealed Films**

| Wt% SQ | High Energy Peak Posn. | Width | Area | Low Energy Peak Posn. | Width | Area |
|---|---|---|---|---|---|---|
| 0 | | | | | | |
| 10 | 667.03 | 117.7 | 16.04 | 680.26 | 45.78 | 7.87 |
| 20 | 659.55 | 123.7 | 35.4 | 681.75 | 47.6 | 11.88 |
| 30 | 653.82 | 131.95 | 56.38 | 683.4 | 48.5 | 14.4 |
| 40 | 619.61 | 155.9 | 65.38 | 680.12 | 62.68 | 27.2 |
| 50 | 552.83 | 79.84 | 59.53 | 656.99 | 100.89 | 61.62 |
| 60 | 551.93 | 82.7 | 74.68 | 654.45 | 102.05 | 68.19 |
| 70 | 551.88 | 84.29 | 94.7 | 652.1 | 101.26 | 77.14 |
| 80 | 552.42 | 83.79 | 104.69 | 650.97 | 101.53 | 85.45 |
| 90 | 552.12 | 84.11 | 128.54 | 650.85 | 101.06 | 98.84 |
| 100 | 551.68 | 86.37 | 140.3 | 651.74 | 102.43 | 96.94 |

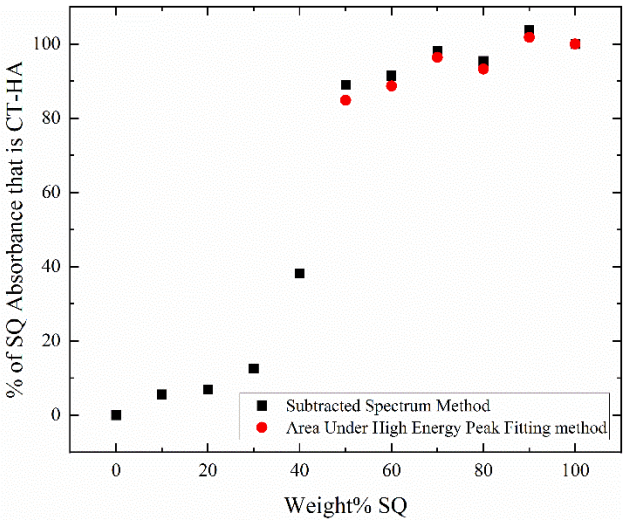


**Figure A8.2 - These data for the 90°C Annealed film are taken from Table A8.1, from the 3rd and 5th columns respectively. Black squares represent the % of SQ absorption that is HCT based on the spectroscopic subtraction method. The red Circles represent the % of SQ absorption that is HCT, determined by normalizing (dividing) the area of the high energy peak for the film by the fitted peak area for the 100% SQ sample, then divided by the wt% SQ in the film. The red circle data has been determined only for the spectra in which the high energy peak is a 550nm peak, as shown in Figure A8.1 above.**

The HCT Contribution Indicator

The percentage HCT can be determined through spectroscopy analysis as described below.

Gaussian Fitting Approach: To explain Figure SI3, we first assume that absorbance at 550nm can only come from the HCT. We then assume that after 5 minutes of 90°C annealing, any phase separation and crystallization is complete for that film. We then claim that the high energy peak originates from HCT absorbance. When we divide the area for the 550nm peak for a given film by the peak area for the 100% SQ 90°C annealed film, and then divide by the fraction of that film that is SQ, this normalizes the peak area in relative units of "per % SQ". This allows us to know the percent of the SQ that is HCT.

Spectral subtraction approach: On the other hand, we have the second assessment of the contribution of the HCT absorbance based on spectral subtraction. We note that absorbance increases linearly as the concentration of a particular species increases, or as the path length of a particular species increases. Therefore, the coefficient used to allow successful subtraction of the

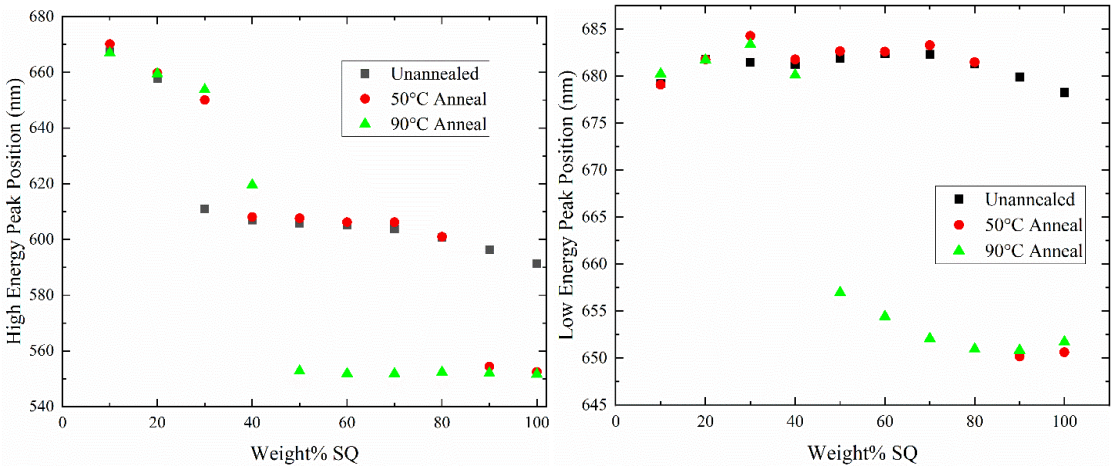


**Figure A8.3 - The peak positions from Table A8.2, Table A8.3, and Table A8.4 for the high (left) and low (right) energy peaks that are arbitrarily fit to the spectra measured for SQ:PCBM blend ratios.**

HCT when divided by the wt% of SQ in the film provides an independent measure of HCT aggregation.

Determining the Predicted Fraction of HCT as a function of Weight percent SQ

A "Gaussian Fit" approach is used to quantify the measured spectra for both the annealed and unannealed samples used in this paper. The spectra are fit to two Gaussian functions. The fits provide parameters which describe i) peak position, ii) area under each curve, and iii) the width of the Gaussian, as shown in Table A8.2, Table A8.3, and Table A8.4. (In each table, we not only include parameters from fits to spectra of films annealed at 90°C but also from fits to spectra from unannealed films, and a set annealed at 50°C).

Given that there is no 500-540nm peak for the unannealed films because HCT concentrations are very low, we explore the parameters for peak position from our Gaussian fits, The high energy (low wavelength) peak positions and low energy (high wavelength) peak positions are plotted respectively in Figure A8.3.

We subsequently plot, in Figure A8.4, the low energy peak position for each film as a function of contribution of HCT for that film, determined by the Gaussian Fit Area Method (Column 7, Table SI1, Black Squares) and the Spectral Subtraction Method (Column 2, Table SI1, Red Squares).

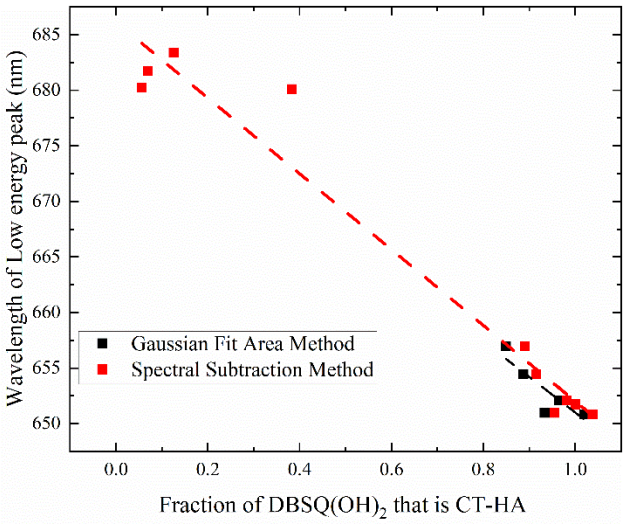


**Figure A8.4 - A plot of the wavelength of the low energy peak as a function of the percentage fraction of HCT, determined by spectral subtraction and Gaussian fit area method.**

The equations for the linear fits to the plots of wavelength of lowest energy peak to the fraction of SQ that is in the HCT state (determined using the two approaches described above) are shown in Figure A8.4 and have the following parameters in Table A8.5. We note that these fits are low in quality with an uncertainty in the fit to Gaussian Fit Area Percentage of ±28%. Finally, these slopes are used to estimate the percentage of SQ that is in the HCT state for both unannealed and annealed film spectra, based on a determination of the lowest energy peak position found from Gaussian fitting.

**Table A8.5 - Parameters for calibration curve linking the wavelength of the low energy peak and the %HCT.**

| %HCT Calculation method for x-axis. | Slope (Error) in nm per percentage point. | Intercept (Error) in nm. | $R^2$ |
|---|---|---|---|
| Spectral subtraction | -34.1 (±2.5) | 686.1 (±1.9) | 0.960 |
| Gaussian Fit Area percentage | -32.0 (± 8.9) | 683.0 (± 8.4) | 0.763 |

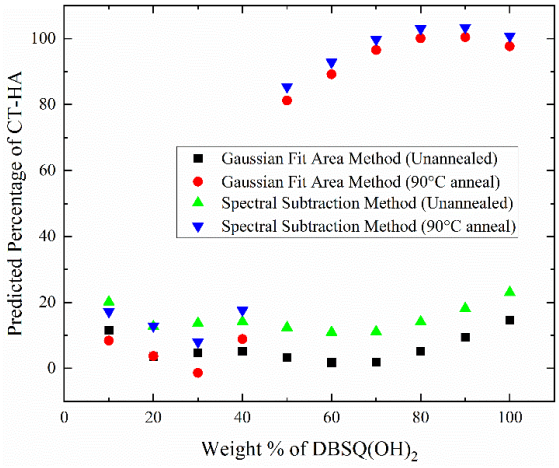


**Figure A8.5 (Same as Figure 3.2) - Predicted percentages of SQ molecules in films associated with HCT species calculated by absorbance curve fitting methods.**

Figure A8.5 and Figure 3.2 both plot data where the fraction of HCT is predicted from the position of the Lambda-Max of the low energy peak in the spectrum as a function of the blend ratio that accompanies each spectrum. The predicted values use the equations for the straight lines presented in Table A8.5 to estimate these fractions, noting that the percentage uncertainty is ±7.3%, based on slope errors for the fitting of peak position to spectral subtraction data.

Calculation of number of molecules in a Charge-Transfer H-aggregate of Squaraine

We first measure the extinction coefficient for the monomer, $\alpha_{mon,1}$ in equation A3-2. We make a key assumption that the integral of the extinction coefficient plotted against energy for the monomer in a *solid* solution is equivalent to the integral of the molar absorptivity versus energy for the squaraine in *liquid* solution when the unit of path length is the centimeter in both cases. Thus, the extinction coefficient is the molar absorptivity multiplied by the molar concentration. Note that in this paper we always use the path length in units of cm. For a low concentration blended film (here SQ is the analyte), the volume (in L) of the solid solvent (here PCBM) can be measured by AFM, as described in the experimental section, and the mass of the SQ in the film can be determined with absorption spectroscopy of redissolved films. Hence,

$$\alpha_{mon,1} = \varepsilon_{mon} c = \frac{\varepsilon n_{SQ}}{V_{PCBM}} \quad \text{A3-2}$$

where $\varepsilon_{mon}$ is the molar absorptivity of dilute isolated DBSQ(OH)$_2$ in units of L mol$^{-1}$ cm$^{-1}$, and $\alpha_{mon,1}$ is the extinction coefficient in cm$^{-1}$, and $V_{PCBM}$ is the volume of the solid solvent.

A comparison between the measured extinction coefficients is shown in Figure 3.4. The ratio of the integrals under the curves for HCT to M using the approach described in equation 3-1 (repeated here) and equation A3-2 is found to be 4.997, which indicates that the HCT encompasses 5 squaraine molecules.

$$\int_{band} \alpha_{CT-HA}(eV) = \frac{x n_{SQ,mon}}{V_{PCBM}} \int_{band} \varepsilon_{mon}(eV) \quad \text{A3-3}$$

Equation 3-1 is also based on the stoichiometric relationship described in equation A3-4, below.

$$5n_{SQ,mon} \rightarrow n_{SQ,CT-HA} \quad \text{A3-4}$$

Where $n_{SQ,mon}$ denotes moles of SQ monomer and $n_{SQ,CT-HA}$ denotes moles of SQ in the HCT form. The number of moles of SQ in the DHA form will be denoted as $n_{SQ,DHA}$ and by definition the dimer H-aggregate comprises 2 molecules of SQ monomer.

$$2n_{SQ,mon} \rightarrow n_{SQ,DHA} \quad \text{A3-5}$$

The further value of this approach is now described. We note that for any particular film the *total* number of SQ moles $n_{SQ,tot}$ and PCBM moles on that film can be determined after redissolving the film, and using simple Beer-Lambert law analysis, taking into account the stoichiometry relations described in equations A3-4 and A3-5. Equation A3-6 describes the number of moles of SQ.

$$n_{SQ,tot} = n_{SQ,mon} + 2n_{DHA} + 5n_{CT-HA} \quad \text{A3-6}$$

We recall our two objectives to quantify how much of any film's absorbance is associated with each SQ species, and secondly to quantify the number of SQ molecules that are then represented by that absorbance. Since we now know the extinction coefficients of the HCT state and the monomer, and for the PCBM film, we can therefore, by elimination, determine the absorbance that is associated with a dimer H-aggregate, which by definition we claim has two molecules of squaraine per absorbing dimer.

We can therefore obtain a coefficient for each species that, in its raw form, is the percentage of the total absorbance ($Abs_{total}$) that each species contributes ($Abs_{PCBM}$, $Abs_{mon}$, $Abs_{DHA}$, $Abs_{CT-HA}$). These values may be provided in future work. A full set of equations illustrating this logic is provided below.

$$Abs_{total} = Abs_{PCBM} + Abs_{Mon} + Abs_{DHA} + Abs_{CT-HA} \quad \text{A3-7}$$

Since we assume that the PCBM has a single amorphous form for all films in this study, and therefore a fixed density, and a predictable thickness, then we can comfortably remove its effective thickness (and subtract the absorbance, in practical terms) such that we focus only on the SQs in our samples.

We then assume that the effective path length for the SQ component, d, is equal to the constant intrinsic thickness of a SQ molecule independent of the environment, $d_{int}$, multiplied by the number of molecules, $N$, that the light passes through depending on the density and film thickness. We consider $N_{tot}$ as the population of all SQ molecules the light passes through. In other words, we can write:

$$Abs_{total} = \alpha d = \alpha d_{int} N_{tot} \quad \text{A3-8}$$

Upon substituting equation A3-7 into equation A3-8, taking into account the stoichiometry of forming aggregates and dimers, and after accounting for and removing the contribution of PCBM

we end up with equation A3-9, which now includes the populations of monomers, $N_{mon}$, dimers $N_{DHA}$, and HCT, $N_{CT-HA}$.

$$Abs_{total} = \alpha_{mon} d_{int} N_{mon} + 2\alpha_{DHA} d_{int} N_{DHA} + x\alpha_{CT-HA} d_{int} N_{CT-HA} \quad \text{A3-9}$$

Upon canceling the intrinsic thickness $d_{int}$ from both sides of equation A3-9, we arrive at:

$$\frac{Abs_{total}}{d_{int}} = \alpha_{mon} N_{mon} + 2\alpha_{DHA} N_{DHA} + 5\alpha_{CT-HA} N_{CT-HA} \quad \text{A3-10}$$

We now divide through by the total number of molecules on the left-hand side (which includes all the molecules of SQ in the sample, and is known) and we end up with a series of coefficients, $C_i$, whose values add up to one.

$$\frac{Abs_{total}}{d_{int} N_{total}} = \alpha_{mon} C_{mon} + 2\alpha_{DHA} C_{DHA} + 5\alpha_{CT-HA} C_{CT-HA} \quad \text{A3-11}$$

Where $C_i = N_i / N_{total}$. The important thing here is that the coefficients represent the relative contribution of SQ molecules within a given species to the overall absorbance of the sample.

We further recognize the total thickness of any film as being:

$$d_{total} = d_{PCBM} + d_{Mon} + d_{DHA} + d_{CT-HA} \quad \text{A3-12}$$

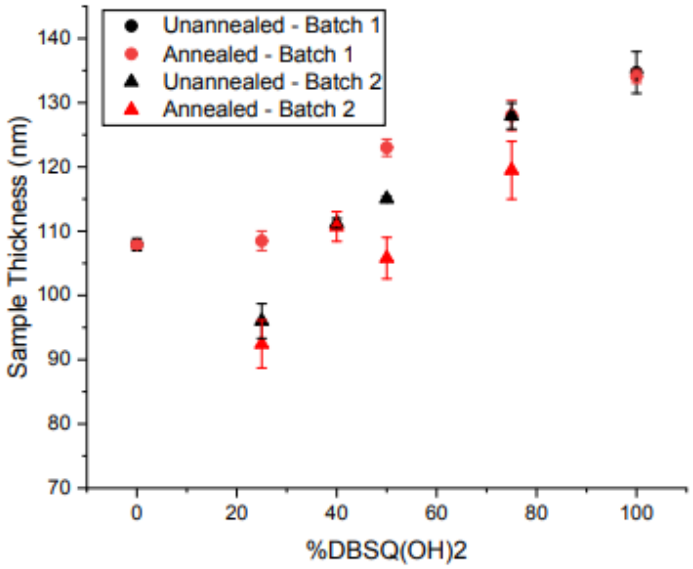


**Figure A8.6 - Sample thickness as a function of analysis for two batches of samples. Each point represents an average of thickness measurements from at least two samples of the same blend ratio. For both batches, the thickness decreases upon annealing, except for the 100% PCBM samples, indicating an increase in the density of the blends with annealing, while the density of pure PCBM remains fixed.**

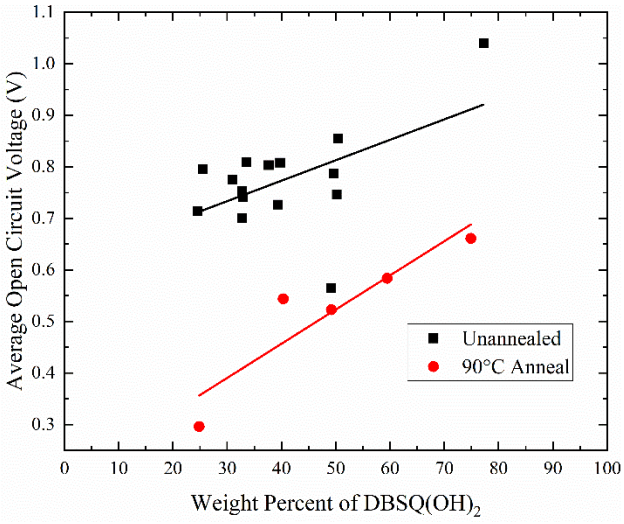


**Figure A8.7 – The average open circuit voltage measured for a series of DBSQ(OH)2:PCBM devices with varying blend ratio, unannealed in black and annealed in red. Linear fits are used as a guide to the eye.**

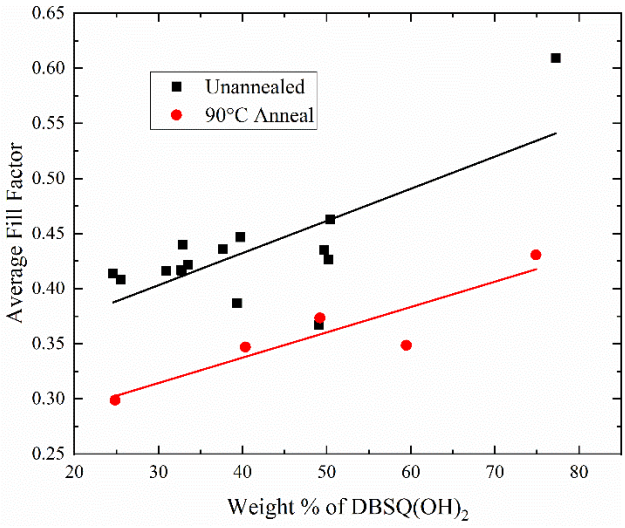


**Figure A8.8 – The average fill factor measured for a series of DBSQ(OH)2:PCBM devices with varying blend ratio, unannealed in black and annealed in red. Linear fits are used as a guide to the eye.**

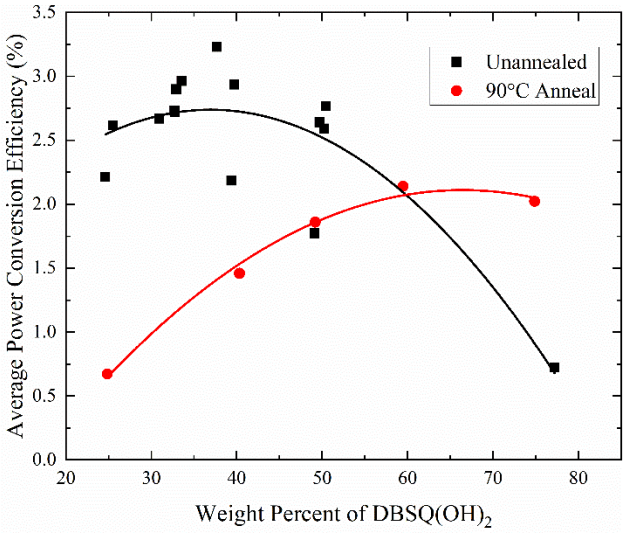


**Figure A8.9 – The average power conversion efficiency measured for a series of DBSQ(OH)2:PCBM devices with varying blend ratio, unannealed in black and annealed in red. Polynomial fits are used as a guide to the eye.**

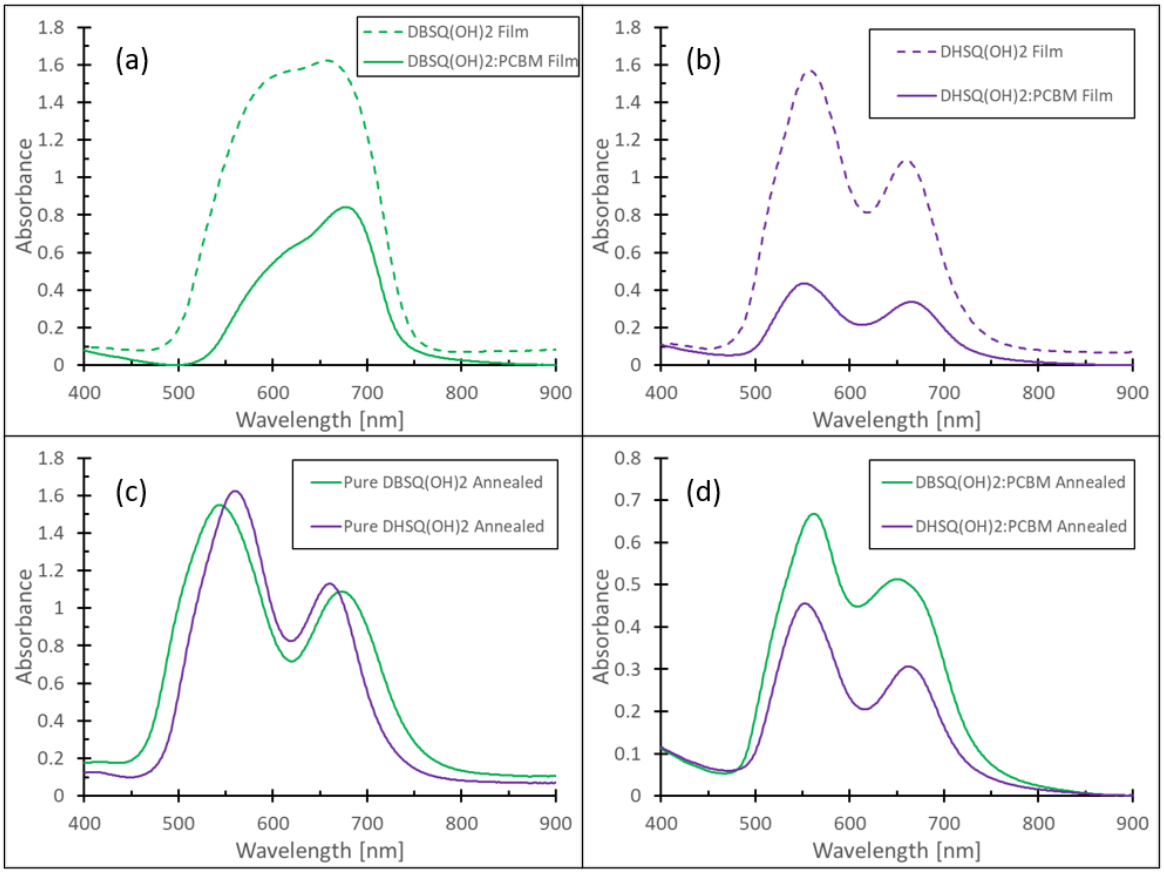


**Figure A8.10 - Absorbance spectra of a)DBSQ(OH)$_2$ and b)DHSQ(OH)$_2$ in a neat thin film and a 1:1 blend film with PCBM. c) and d) compare the annealed absorption spectra of DBSQ(OH)$_2$ and DHSQ(OH)$_2$ in a c) neat film and d) a 1:1 blend with PCBM.**

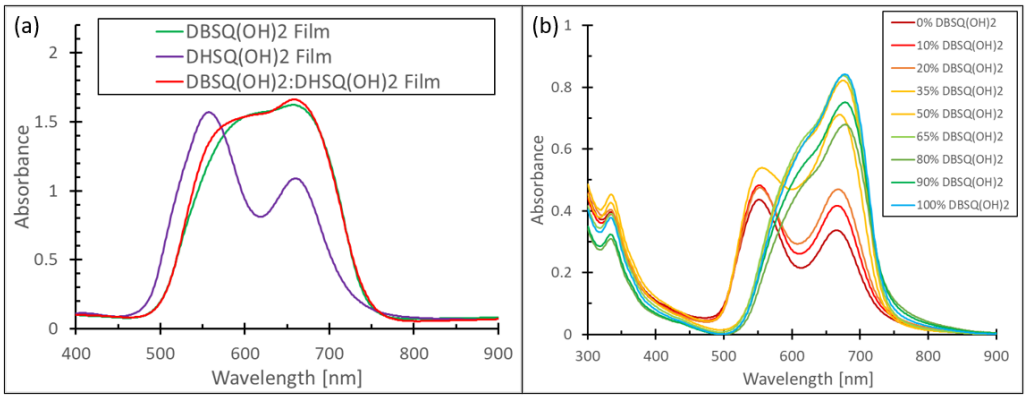


**Figure A8.11 – a) Absorbance spectra of a binary blend of both Squaraine donors compared to individual neat films of each Squaraine molecule. b) Absorbance of unannealed ternary blend films with changing DBSQ(OH)$_2$: DHSQ(OH)$_2$ weight ratio in the donor component while the donor:acceptor ratio is constant at 1:1.**

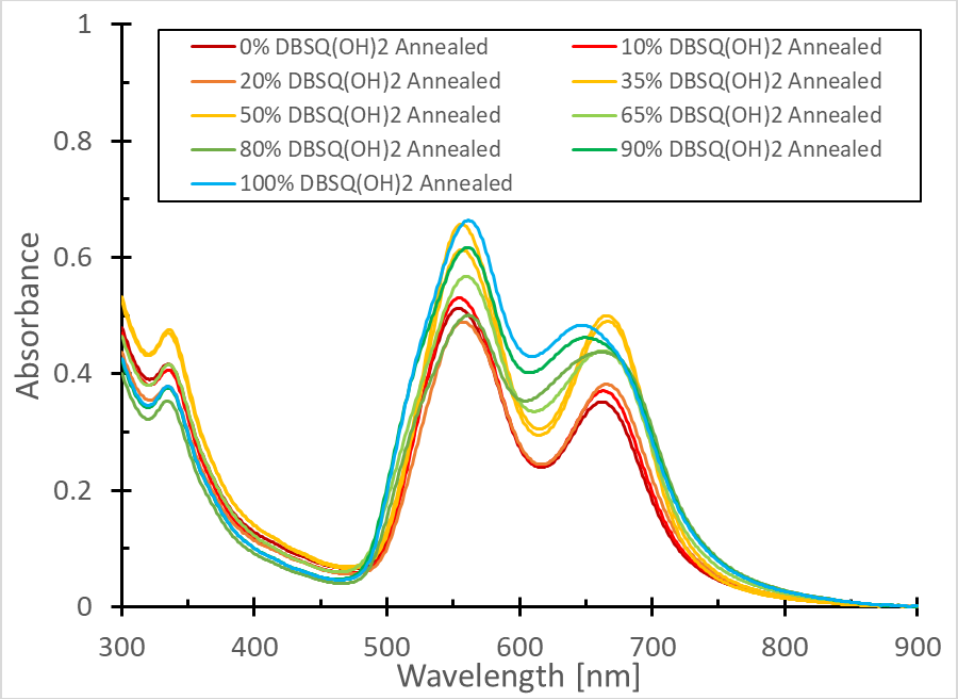


**Figure A8.12 – Absorbance spectra of annealed ternary blend films with changing $DBSQ(OH)_2$: $DHSQ(OH)_2$ weight ratio in the donor component while the donor:acceptor ratio is constant at 1:1. Annealing parameters were 5 minutes at 90˚C.**

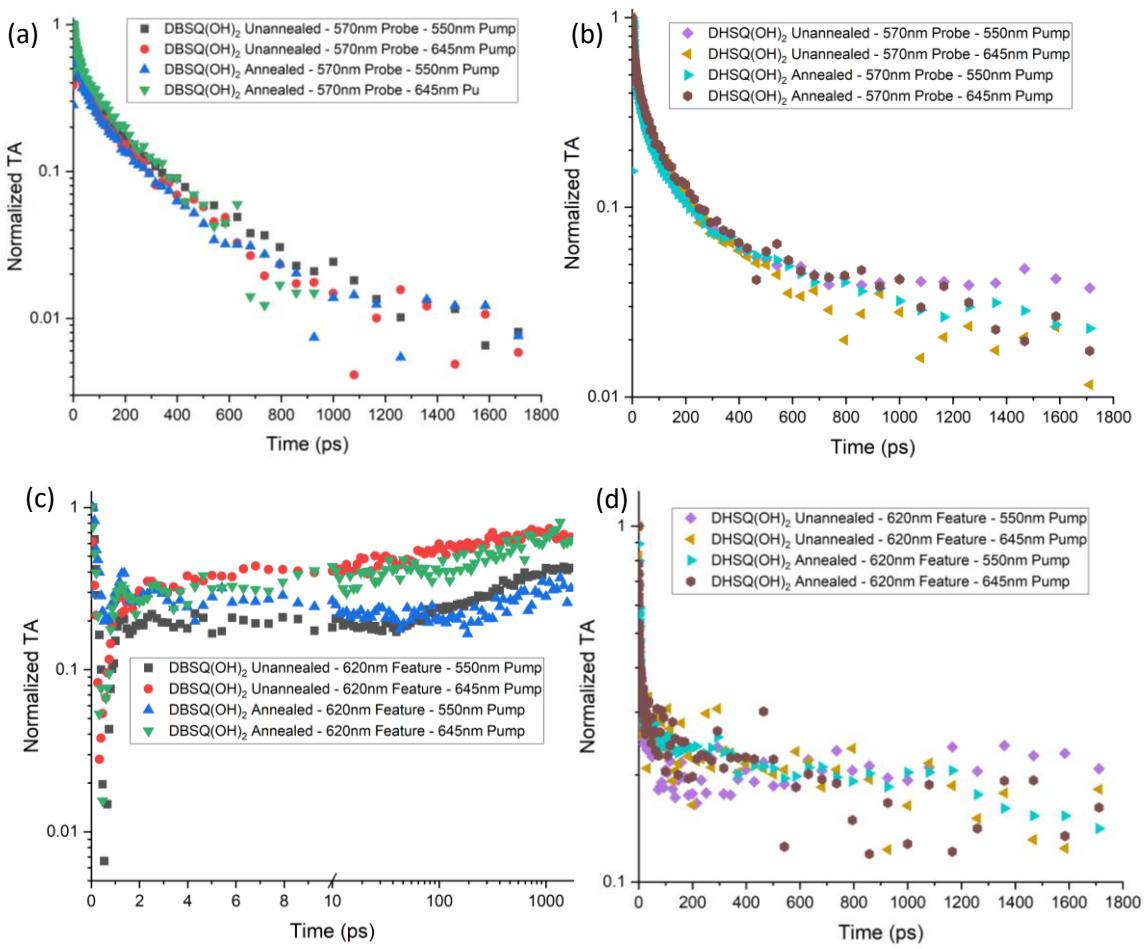


**Figure A8.13 – Kinetic Traces of the 620nm feature (a, b) and 550nm feature (c, d) for $DBSQ(OH)_2$ (a, c) and $DHSQ(OH)_2$ (b, d) neat film transient absorption measurements from Figure 5.4 with a log scale on the y-axis. Note that subfigure c is now normalized from 0 to 1 instead of to the maximum to remove negative values.**

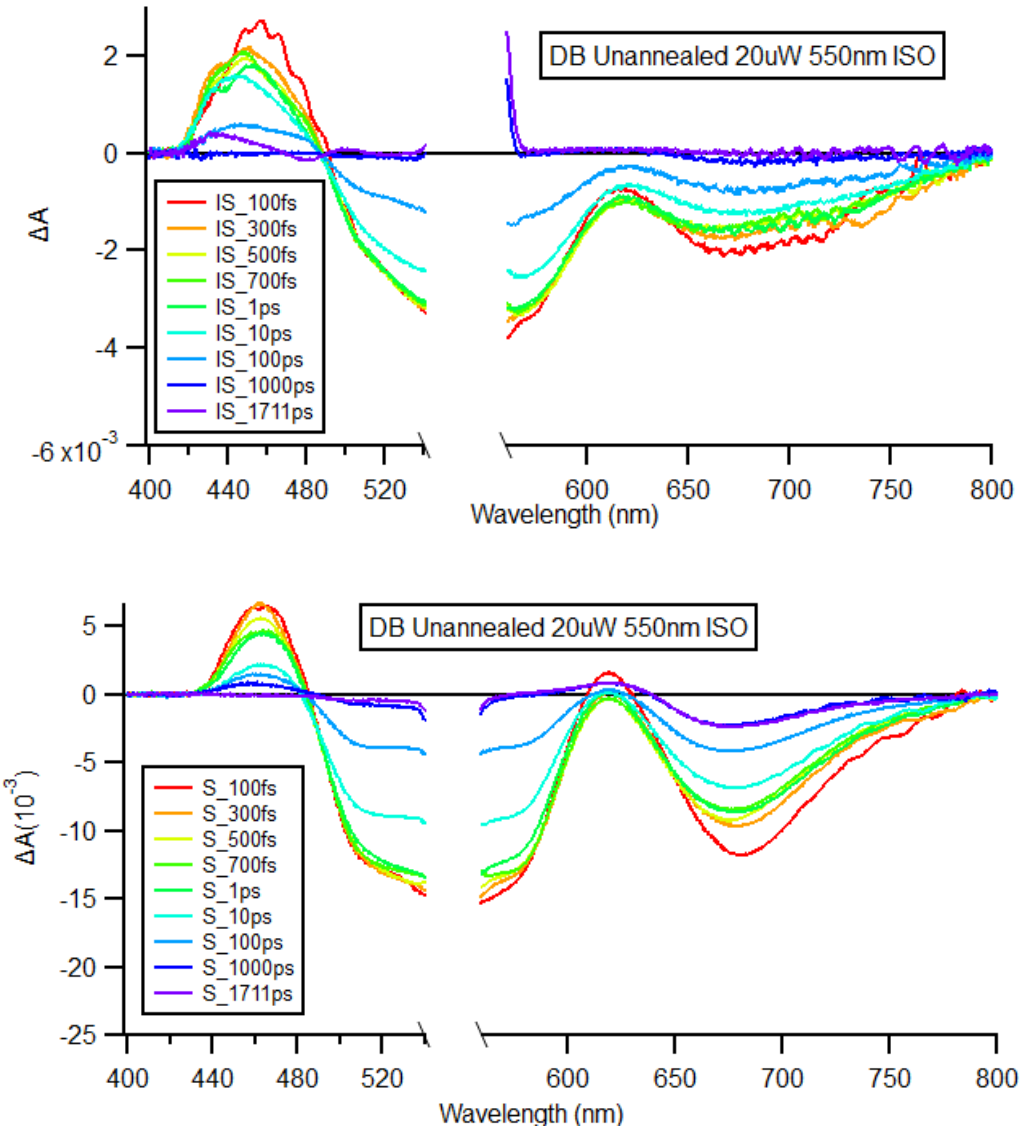


**Figure A8.14 – Comparison of the transient absorption response from a 550nm excitation of DBSQ(OH)$_2$ films cast from (top) 7mg/ml solution and (bottom) 4.5mg/ml solution.**